uOttawa

L'Université canadienne
Canada's university

FACULTÉ DES ÉTUDES SUPÉRIEURES ET POSTOCTORALES

uOttawa

L'Université canadienne
Canada's university

FACULTY OF GRADUATE AND POSDOCTORAL STUDIES

Dennis Ramos

AUTEUR DE LA THÈSE / AUTHOR OF THESIS

M.Sc. (Chemistry)

GRADE / DEGREE

Department of Chemistry

FACULTÉ, ÉCOLE, DÉPARTEMENT / FACULTY, SCHOOL, DEPARTMENT

Conformational Studies of Cell Division Regulator MinE by Nuclear Magnetic Resonance and Circular Dichroism Spectroscopy

TITRE DE LA THÈSE / TITLE OF THESIS

Dr. N. Goto

DIRECTEUR (DIRECTRICE) DE LA THÈSE / THESIS SUPERVISOR

CO-DIRECTEUR (CO-DIRECTRICE) DE LA THÈSE / THESIS CO-SUPERVISOR

EXAMINATEURS (EXAMINATRICES) DE LA THÈSE / THESIS EXAMINERS

Dr. A. St-Amant

Dr. Y. Aubin

Gary W. Slater

Le Doyen de la Faculté des études supérieures et postdoctorales / Dean of the Faculty of Graduate and Postdoctoral Studies

Conformational Studies of Cell Division Regulator MinE by Nuclear Magnetic Resonance and Circular Dichroism Spectroscopy

Dennis Ramos

Thesis submitted to the
Faculty of Graduate and Postdoctoral Studies
University of Ottawa
In partial fulfillment of the requirements for the degree of

Master in Science in Chemistry

Ottawa – Carleton Chemistry Institute
University of Ottawa
Ottawa, Ontario
CANADA K1N 6N5

Candidate

Dennis Ramos

Supervisor

Dr. Natalie Goto

Your file Votre référence
ISBN: 978-0-494-18461-5
Our file Notre référence
ISBN: 978-0-494-18461-5

Abstract

Symmetric division of Gram-negative bacteria depends on the combined action of three proteins that ensure correct positioning of the cell division septum; namely, MinC, MinD and MinE. To achieve this function, MinC and MinD form a membrane-bound complex that blocks cell division at all potential sites. Opposing this inhibition is MinE, which interacts with MinD via its N-terminal anti-MinCD domain to site-specifically counter the action of the MinCD complex. The anti-MinCD domain has been proposed to bind MinD in a helical conformation, however, little is actually known about the structure of this functionally critical region. In order to understand how MinE can perform its anti-MinCD function, we have therefore investigated the structural properties of the full-length MinE from *N. gonorrhoeae*. Results from solution NMR show that, in contrast to previous models, parts of the anti-MinCD domain are stably folded with many functionally important residues forming part of a β-structure. In addition, this structure may be stabilized by interactions with the C-terminal topological specificity domain, since mutations made in one domain led to NMR spectral changes in both domains. The inactive MinE mutant L22D showed even larger evidence of structural perturbations, with significant destabilization of the entire MinE structure. Overall, these results suggest an intimate structural association between the anti-MinCD and topological specificity domains raising the possibility that the functional properties of the two domains could be modulated through this interaction

Table of Contents

		Page #
Abstract		iii
Table of Contents		iv
List of Figures		vi
List of Tables		viii
Abbreviations		ix
Acknowledgements		x
Chapter 1: Introduction Part 1: Biological Background		
1.1	*Role of Cell Division in Disease Progression*	1
1.2	*The Min Protein Cycle*	4
1.3	*Min Protein Oscillation at the Cellular Level*	4
1.4	*MinE Function*	6
1.5	*MinE Structure*	7
1.6	*Structural and Functional Comparison of MinE from Round- versus Rod-Shaped Bacteria*	11
1.7	*Thesis Objectives*	12
Chapter 2: Introduction Part 2: Background to Methods Used for the Characterization of Protein Structure		
2.1	*Principles of Circular Dichroism Spectroscopy – Origin of the CD Effect*	14
2.2	*Characteristic CD Spectra of Protein Secondary Structures*	16
2.3	*NMR Spectroscopy – The $^{1}H - ^{15}N$ HSQC*	19
2.4	*Multi-Dimensional NMR Spectroscopy – Heteronuclear Correlations*	21
2.5	*Sequential Backbone Assignment Using Triple-Resonance Experiments*	25
2.6	*Secondary Structure Determination from Assigned Backbone Chemical Shifts*	28
2.7	*Application of CD and Solution NMR to $MinE_{Ng}$*	28
Chapter 3: Materials and Methods		
3.1	*Bacterial Plasmids*	30
3.2	*Bacterial Growth Media*	30
3.3	*Preparation of Competent Cells*	31

3.4 *Transformation of Bacterial Plasmid DNA into E. coli* 32
3.5 *Plasmid Mini-Preps* 33
3.6 *Agarose Gel Electrophoresis for DNA Analysis* 34
3.7 *Overxpression of Recombinant Gonococcal MinE* 34
3.8 *Purification of $MinE_{Ng}$ by Nickel Affinity Chromatography* 35
3.9 *Optimization of Protein Solubility* 36
3.10 *Size-Exclusion Chromatography of $MinE_{Ng}$* 37
3.11 *NMR Spectroscopy* 38
3.12 *Circular Dichroism Spectroscopy* 40
3.13 *Protein Concentration Determination* 40
3.14 *Sodium Dodecyl Sulphate – PolyAcrylamide Gel Eletrophoresis (SDS – PAGE)* 41

Chapter 4: Results

4.1 *Purification of $MinE_{Ng}$ and Estimation of its Complex Molecular Mass* 44
4.2 *Optimization of Sample Buffer Conditions for NMR Analyses* 47
4.3 *NMR Analyses of Wild-Type $MinE_{Ng}$ at High pH* 51
4.4 *Backbone Chemical Shift Assignment of $MinE_{Ng}$* 55
4.5 *Secondary Structure Prediction Based Secondary Shifts from Random Coil Values* 62
4.6 *Confirmation of Assignments and Structure for Helical Regions of MinE with the ^{15}N-edited NOESY* 65
4.7 *NMR Analyses of $MinE_{Ng}$ Mutants* 66
4.8 *Results Summary* 73

Chapter 5: Discussion

5.1 *$MinE_{Ng}$ is Stably Folded at Elevated pH Conditions* 75
5.2 *$MinE_{Ng}$ is Structurally Similar to $MinE_{Ec}$* 78
5.3 *Evidence for Interactions Between the Topological Specificity and Anti-MinCD Domains* 80

Claims to Original Research 85

Publications 86

References 87

List of Figures

		Page
Figure 1.1:	*Cell Division Pattern in A) Rod- and B) Round-Shaped Bacteria.*	**2**
Figure 1.2:	*Models for oscillation of Min proteins in E. coli – A) The Min protein interaction cycle.*	**3**
Figure 1.3:	*Structure of the E. coli MinE^{TSD} (PDB# 1EV0) **A)** Ribbon diagram of solution NMR structure of the TSD from the E. coli MinE. **B)** Location of conserved residues on the surface of E. coli MinE^{TSD} residues in the α-helix and **C)** in the β-sheet.*	**9**
Figure 2.1:	*The Peptide Bond is Rigid and Planar. The N – C_α and C_α– CO bonds can rotate with bond angles designated as phi (ϕ) and psi (ψ), respectively.*	**16**
Figure 2.2:	*Ball and stick model of two views of **A)** α-helical and **B)** β-sheet secondary structures.*	**17**
Figure 2.3:	*Characteristic CD Spectra for α-helix (red), β-sheets (blue) and random coil (green) conformations.*	**18**
Figure 2.4:	*HNCO Backbone Correlation Experiment. **A)** Magnetization transfer **B)** Schematic view of a simplified 3D HNCO spectrum. **C)** $^{1}H - ^{13}C$ strip plot to simplify visualization of the spectrum.*	**21**
Figure 2.5:	*Sequential Assignment Using HNCA and HN(CO)CA Experiments.*	**24**
Figure 2.6:	*Sequential Assignment Using CBCA(CO)NH and HNCACB Spectra.*	**26**
Figure 4.1:	*$MinE_{Ng}$ Purification on a Ni-NTA column.*	**44**
Figure 4.2:	*Purification of $MinE_{Ng}$ by Size-Exclusion Chromatography.*	**45**
Figure 4.3:	*Molecular Weight Calibration of the Superdex75® 10/300GL column.*	**46**
Figure 4.4:	*$^{1}H - ^{15}N$ HSQC at High pH.*	**51**
Figure 4.5:	*Effect of pH on $^{1}H - ^{15}N$ HSQC of $MinE_{Ng}$.*	**52**
Figure 4.6:	*Effect of pH on CD Spectra of $MinE_{Ng}$.*	**53**

Figure 4.7: *$^{1}H - ^{13}C$ Strip Plots from HN(CO)CA and HNCA experiments for $MinE_{Ng}$ Residues 26 to 31.* **54**

Figure 4.8: *Assigned HNCACB Strip Plot for the Anti-MinCD Domain of $MinE_{Ng}$.* **57**

Figure 4.9: *HNCACB Strip Plots for Backbone Assignment of α-Helix B of $MinE_{Ng}$.* **58**

Figure 4.10: *HNCACB Strip Plots for Backbone Assignment of β-Sheet 2 of $MinE_{Ng}$.* **59**

Figure 4.11: *Assigned $^{1}H - ^{15}N$ HSQC spectrum of WT MinE at pH 9.5.* **60**

Figure 4.12: *Assigned HNCO spectrum of WT MinE at pH 9.5.* **61**

Figure 4.13: *Secondary structure of $MinE_{Ng}$ determined from C_α and CO chemical shifts.* **63**

Figure 4.14: *$^{1}H - ^{1}H$ Strips from the ^{15}N-Edited HSQC – NOESY for **A)** residues I4 – F8 and **B)** residues Y39 – V55.* **64**

Figure 4.15: *$^{1}H - ^{15}N$ HSQC spectrum of A18D (red) superimposed on the black spectrum of WT $MinE_{Ng}$.* **66**

Figure 4.16: *CD Spectra of WT (red) vs. A18D (blue) $MinE_{Ng}$ in 10 mM Tris pH 9.5 at 25°C.* **68**

Figure 4.17: *$^{1}H - ^{15}N$ HSQC spectra of E46A (red) and WT (black) $MinE_{Ng}$.* **69**

Figure 4.18: *CD Spectra of WT (red) and E46A (blue) $MinE_{Ng}$ in 10 mM Tris pH 9.5 at 25°C.* **70**

Figure 4.19: *CD Spectra of WT (red) and L22D (blue) $MinE_{Ng}$ in 10 mM Tris pH 7.4. at 25°C.mM Tris pH 9.5 at 25°C.* **71**

Figure 4.20: *$^{1}H - ^{15}N$ HSQC spectrum of 250 μM L22D in 50 mM Tris, 50 mM NaCl, 100 μM EDTA, 0.02% sodium azide and 0.2mM PMSF at pH 7.2, 25°C.* **72**

Figure 4.21: *Size-exclusion chromatogram of WT and L22D $MinE_{Ng}$ using Superdex75® 10/300 GL column in 50 mM Tris, 150 mM NaCl, 1 mM EDTA at pH 9.5* **73**

Figure 5.1 *Protein Sequence Alignment for MinE* **77**

List of Tables

		Page
Table 2.1:	*Triple Resonance Experiments Used for Backbone Sequential Assignment*	**22**
Table 2.2:	*Typical $^{13}C_\alpha$ and $^{13}C_\beta$ Chemical Shift Ranges from Proteins*	**27**
Table 3.1:	*Spectral Data Set*	**39**
Table 4.1:	*Assessment of Protein Solubility*	**49**

Abbreviations

ADP	Adenosine diphosphate
ATP	Adenosine triphosphate
BCA	Bicinchoninic acid
BSA	Bovine serum albumin
CD	Circular dichroism
DNA	Deoxyribonucleic acid
DSS	2,2-dimethyl-2-silapentane-5-sulfonate (DSS)
Ec	*Escherichia coli; E. coli*
Ec-TSD	*Escherichia coli* topological specificity domain
EDTA	Ethylenediaminetetraacetic acid
FPLC	fast protein liquid chromatography
HSQC	Heteronuclear single quantum coherence
IPTG	isopropyl-β-D-thiogalactopyranoside
kDa	Kilodalton
$MinE_{Ec}$	*Escherichia coli* MinE
$MinE_{Ng}$	*Neisseria gonorrhoeae* MinE
MRE	Mean residue ellipticity
Ng	*Neisseria gonorrhoeae; N. gonorrhoeae*
Ng-TSD	*Neisseria gonorrhoeae* topological specificity domain
NMR	Nuclear magnetic resonance
NOE	Nuclear overhauser effect
NOESY	NOE spectroscopy
NTA	Nitriloacetic acid
PMSF	Phenylmethanesulfonyl Fluoride
ppm	Parts per million
SDS-PAGE	Sodium dodecyl sulphate – polyacrylimide gel electrophoresis
Tris	Tris(hydroxymethyl)aminomethane
TSD	Topological specificity domain
WT	Wild type

Acknowledgements

I would like to thank Dr. Natalie Goto for being a wonderful supervisor and mentor. Her teachings, support and vision have helped me in more ways I can say. Her research has given me the opportunity to expand on my knowledge in the fields of protein chemistry and biochemistry. I have very much enjoyed the time I have spent in the lab and I have been privileged to learn under her wings.

I would like to thank all present and former members of the "GLF" (or "GLAF"?) lab for their kindness, support and friendship. I will surely miss our outings, our lunches (you guys know what I meant by this!) and our endless shenanigans. It has truly been an unforgettable year. Thanks to Sudsy for his constant support during this trying time and his constant advice; thanks to Hay-Daddy's "social events" and road trip AAAHHHH!!!; thanks to Steve and his hilarious "Dr. Zoidberg" mating dance; thanks to Allison for inviting me to Sarnia during Christmas, my "sistah from another mothah"; and thanks to the "Wu – Cheng Clan" for all your cracked jokes, they are the best! I would also like to extend my special thanks to Dr. Thierry Ducat for all his help and advice, which is very much appreciated. Special thanks to Dr. Michelle Shaw and Delphine Courmier for being wonderful friends and I'll never forget our outings to Second Cup.

Lastly, I would like to thank my best friends from Winnipeg and your encouragements meant a lot to me. Thanks to my family back home and in Winnipeg especially my Tia Yoly for their constant support and love.

CHAPTER 1

INTRODUCTION Part 1: *Biological Background*

1.1 Role of Cell Division in Disease Progression

Many human illnesses are caused by bacterial infections. How these infectious agents multiply within a host is a fundamental part of disease progression (*1*). Multiplication of bacteria occurs via binary fission in a tightly regulated event that must ensure that equal amounts of genetic material be distributed between daughter cells. This means that the cytokinetic septum that splits the cell must be placed at a point that gives rise to symmetric division. For rod-shaped cells, this occurs at cell mid-point (Figure 1.1A) (*2*), while round-shaped cells divide along alternating perpendicular planes (Figure 1.1B) (*3, 4*). Clearly, the mechanisms underlying division site placement are very complex and highly regulated. How the timing of Z-ring assembly inside the cell is regulated and how the transition from ring assembly to constriction is controlled temporally is still not very well understood.

Division in bacteria involves the coordinated constriction of cell envelope layers by the septal ring, a cytoskeleton-like sub-cellular structure that assembles at the division site (*5*). This equatorial ring structure remains associated with the invaginating cell membrane until the two daughter cells separate. Septum formation is initiated by a protein called FtsZ which forms a polymer along with other cell division proteins (*6-9*). Formation of this septum is inhibited by the nucleoid, limiting its formation to either mid-point or polar

regions of the cell (*10-15*). However, in normally dividing bacteria, septum formation does not occur in the polar region but is instead restricted to the cell mid-point, thereby ensuring symmetric division of the parent cell. This thesis focuses on a protein called MinE, which is responsible for ensuring that the septum exclusively forms at mid-cell.

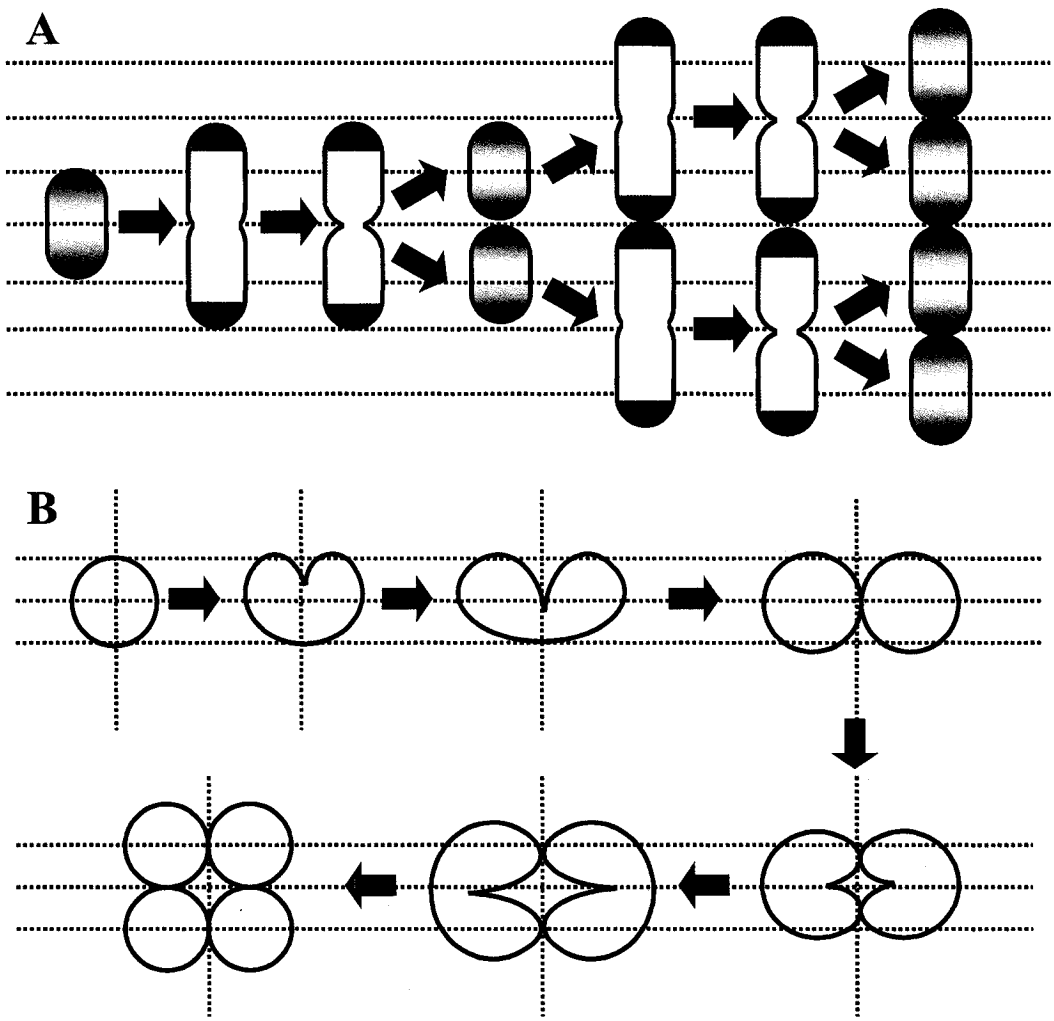

Figure 1.1: *Cell Division Pattern in A) Rod- and B) Round-Shaped Bacteria. The blue lines represent the division planes. The green regions represent the polar sites in the rod-shaped cells.*

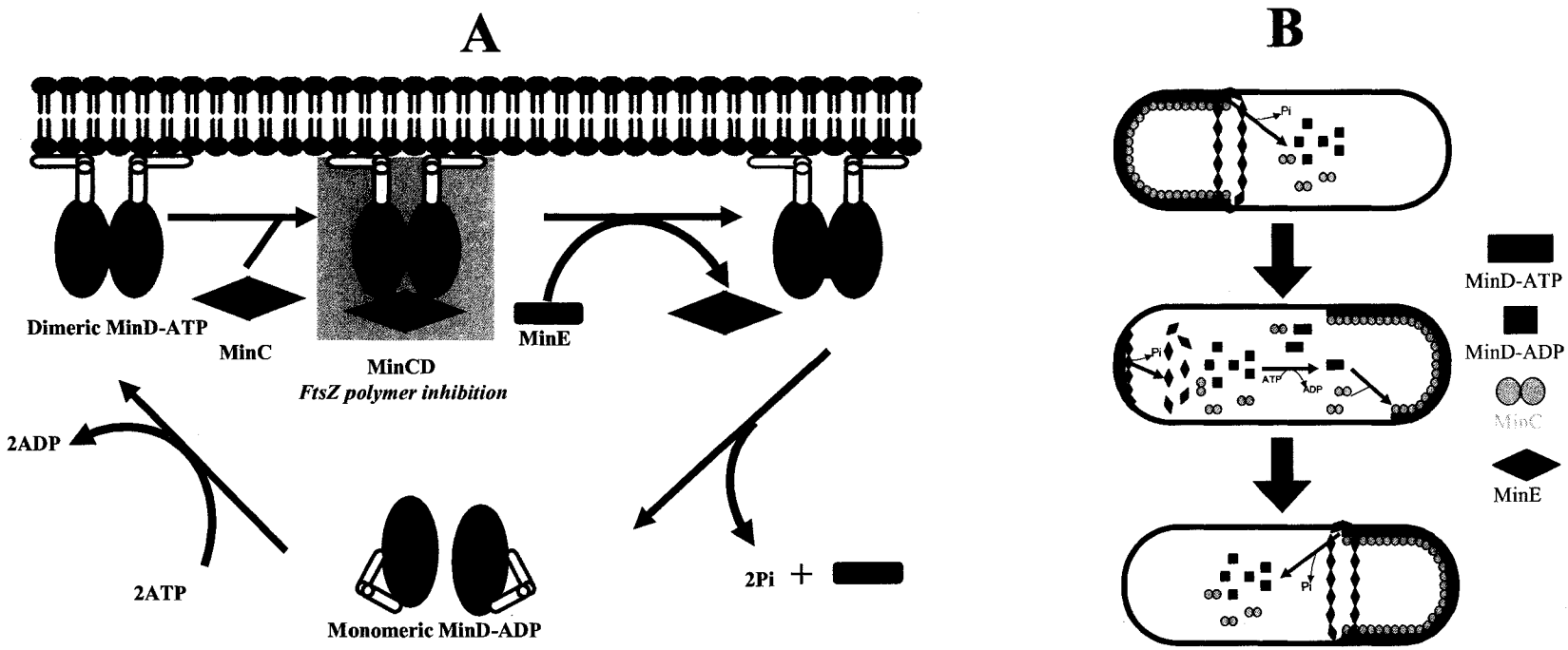

Figure 1.2: *Models for oscillation of Min proteins in E. coli – A) The Min protein interaction cycle. ATP exchange for ADP in monomeric MinD leads to dimerization and membrane localization of MinD. MinC is recruited to the membrane by binding this membrane-bound MinD where it inhibits cell septum formation. MinC can be displaced by MinE binding to MinD. This stimulates MinD ATPase activity releasing MinE and the ADP-bound form of MinD from the membrane. Cytoplasmic MinD is then available to undergo nucleotide exchange, allowing the process to be repeated. The MinCD complex (shaded in grey) is the only point along the Min protein cycle that inhibition of FtsZ polymer formation can occur. B) Schematic diagram of the oscillation of the E-ring and MinCD polar zones. A polar zone rich in membrane-localized MinCD forms with its leading edge capped by the ring formed by MinE (E-ring). This polar zone is dissociated by the E ring whereupon MinE is released into the cytoplasm. Meanwhile a new MinCD polar zone is being established at the opposite pole. Once the local concentration of MinE is high enough a new E-ring can be established at the leading edge of the new MinCD polar zone.*

1.2 The Min Protein Cycle

In Gram-negative bacteria, there are three Min proteins that regulate the correct positioning of the cell division septum by preventing cell division at the polar sites (highlighted in green in Figure 1.2A). These three proteins, called MinC, MinD and MinE, are present in a diverse group of Gram-negative bacteria including the bacillus *E. coli* and the coccus *N. gonorrhoeae* (*16-18*). A number of mutational studies have been done to eludicate the general mechanism behind Min protein function (summarized in Figure 1.2A). These studies have shown that MinC acts as a non-specific division inhibitor that is capable of blocking cell division through a disruption of FtsZ polymerization (*19-21*). However the ability of MinC to inhibit septum formation relies on its interaction with the MinD protein which can localize to the inner cell membrane in the presence of ATP (*22-31*). It has been shown that MinD exists in a monomeric cytoplasmic form when bound to ADP and in this form, it is not capable of binding to MinC (*22-31*). Therefore, only in the presence of ATP-bound MinD can MinC appropriately localize to the membrane where it can act to inhibit FtsZ polymerization. Antagonizing this inhibition is the MinE protein, which can displace MinC through direct interactions with MinD. Formation of the MinE-MinD complex stimulates ATPase activity in MinD, leading to the dissociation of MinD from the membrane and the regeneration of monomeric ADP-bound MinD. MinE is also released upon ATP hydrolysis (*22-24, 27, 28, 31-33*).

1.3 Min Protein Oscillation at the Cellular Level

A consequence of the antagonistic Min protein cycle at the cellular level is a dynamic localization of different Min complexes in different regions of the cell . A number

of studies with fluorescently-tagged proteins have shown that a newly dividing cell establishes a MinCD-rich zone at one pole of the growing cell (*10, 11, 15, 27, 28, 34, 35*) (Figure 1.2B). At the leading edge of this polar zone is a MinE-rich structure that has been characterized as the E-ring (*36, 37*). This E-ring is thought to catalyze the dissociation of the MinCD polar zone, liberating these molecules into the cytoplasm (*8, 10, 15, 20, 27, 38*). Free to diffuse through the cell cytoplasm, these proteins re-localize to the membrane at the opposite polar end of the cell while the original polar zone continues to be dissociated by the E-ring (*34, 36*). Once the original polar zone has been completely disrupted, MinE dissociates and is released into the cytoplasm where it is now available to establish a new E-ring at the leading edge of the newly formed MinCD zone (*34, 39*). The effect of this cycle is an oscillation of the MinCD-rich polar zones from end to end of the cell, preventing the formation of the cell division septum in these regions. Meanwhile, the MinE ring sweeps out a MinCD-free region at cell mid-point, creating a zone where cell division can occur (*15, 39, 40*).

More recently, it has been shown that this oscillation of Min proteins actually occurs along a sub-cellular coiled array that appears to persist along the length of the cell. Within this array, the bulk of MinCD assembles at one cell pole while disassembling at the other pole (*34, 39*). In contrast, high concentrations of MinE localize to one or two loops of the coiled structure within a central region of the cell (*15, 39*). These same studies suggest that all three Min proteins comprise part of the same higher-order coiled structure and that oscillation reflects the redistribution of Min proteins across this permanent scaffold of Min proteins (*15*).

While this cycle of Min protein interactions is well understood in general terms, the mechanism underlying these various states has not been elucidated at the molecular level.

For example, it is not known how MinE displaces MinC from the MinCD complex and stimulates ATP hydrolysis by MinD. In addition, it is not known how MinE assembles into the E-ring and site-specifically counters MinCD activity such that the inhibitory action of MinCD is relieved only at the mid-point of the cell (*10*), or how MinE acts to promote site-specific regulation of bacterial cell division. In order to answer these questions, more information is needed about the functional domains of this cell division regulator MinE.

1.4 MinE Function

A wide range of mutational and truncation studies have shown that MinE plays a central role in the regulation of cell septum placement. In some of the earliest experiments investigating cell division site placement, it was shown that wild-type *E. coli* transformed with a plasmid overexpressing MinE gave rise to the production of small, chromosomeless cells called minicells, that result from inappropriate cell division at polar sites (*17, 41*). This promiscuous formation of the cell division septum at both polar and mid-cell locations showed that the inhibition of cell septum formation by the MinCD complex could be overcome by large quantities of MinE. Due to this loss of specificity in the localization of MinE function in bacteria forming minicells, this type of phenotype is said to reflect loss of topological specificity function (*17*).

A number of studies have since been done to delineate the regions of MinE that are important for topological specificity function. Most notably, overexpression of a truncated construct containing only the C-terminal residues 31-88 of MinE ($MinE_{31-88}$) was also found to give rise to a minicell phenotype. Consequently, this fragment has been named the topological specificity domain (TSD) (*12, 17, 42, 43*). In contrast, the N-terminal

region of MinE appears to be associated with a different function related to disruption of the MinCD complex (*12*). Truncation studies in *E. coli* have shown that an N-terminal fragment including the first 22 amino acid residues from MinE is sufficient to inhibit MinCD activity (*42-44*). For this reason the N-terminal region of MinE, encompassing residues 1 - 30, has been termed the anti-MinCD domain (*12*). Therefore, it appears that the two distinct functional properties of MinE namely anti-MinCD and the topological specificity, localize to two different parts of the primary sequence.

1.5 MinE Structure

Some indication that these functional domains identified in the truncation studies may also correspond to structural domains was provided by limited proteolysis studies. In these experiments, limited exposure of MinE to the proteolytic enzyme trypsin was shown to lead to the generation of a trypsin-resistant fragment that also happens to be correlated with topological specificity function (*43*). The stability of this domain against proteolytic digestion suggested that, unlike the protease-susceptible N-terminal domain, the TSD is a stable, independently folded structure. This idea was substantiated by elucidation of the 3D structure for the TSD by solution NMR (*45*). In this structure (Figure 1.3A), it was observed that the TSD forms a unique homodimer in which each monomer consists of a αβ sandwich fold (*45*). As shown by the ribbon diagram representation of this structure in Figure 1.3A, within each monomer an α-helix packs against an anti-parallel β-hairpin. Inter-dimer interactions are formed between a hydrophobic face of the αB α-helix and the C-terminal β-sheet β2 (*45*). The extensive dimer interface therefore includes inter-

molecular hydrogen bond interactions between β-sheets and packing of hydrophobic side-chains between α-helices. The high affinity of this interaction as predicted from this extensive interface has been confirmed by analytical ultra-centrifugation studies that show that $MinE^{TSD}$ self associates in solution in a monomer – dimer equilibrium with a dissociation constant of 0.6 μM (*43, 46*).

Analysis of the *E. coli* TSD structure revealed two patches of highly conserved residues on the surface that were potential candidates for mediating topological specificity of MinE (*43*). As shown in Figure 1.3B and Figure 1.3C, one patch includes a number of β-sheet residues and the second patch localizes to α-helix residues adjacent to the dimerization interface. Subsequent mutational analyses identified two residues in this helix that are critical for MinCD topological specificity function: D45 and V49 (*10, 11, 43, 47*). When mutations were made to one or both of these sites and the mutants were expressed in place of WT MinE, minicell formation was observed. This result indicated that these MinE mutants were capable of inhibiting the MinCD complex, but had lost the ability to specifically perform this function at cell mid-site. This loss of specificity function did not seem to arise from large-scale structural changes as assessed by NMR and size-exclusion chromatography (*43, 45, 46*), raising the possibility that these residues form a functional interface responsible for topological specificity function.

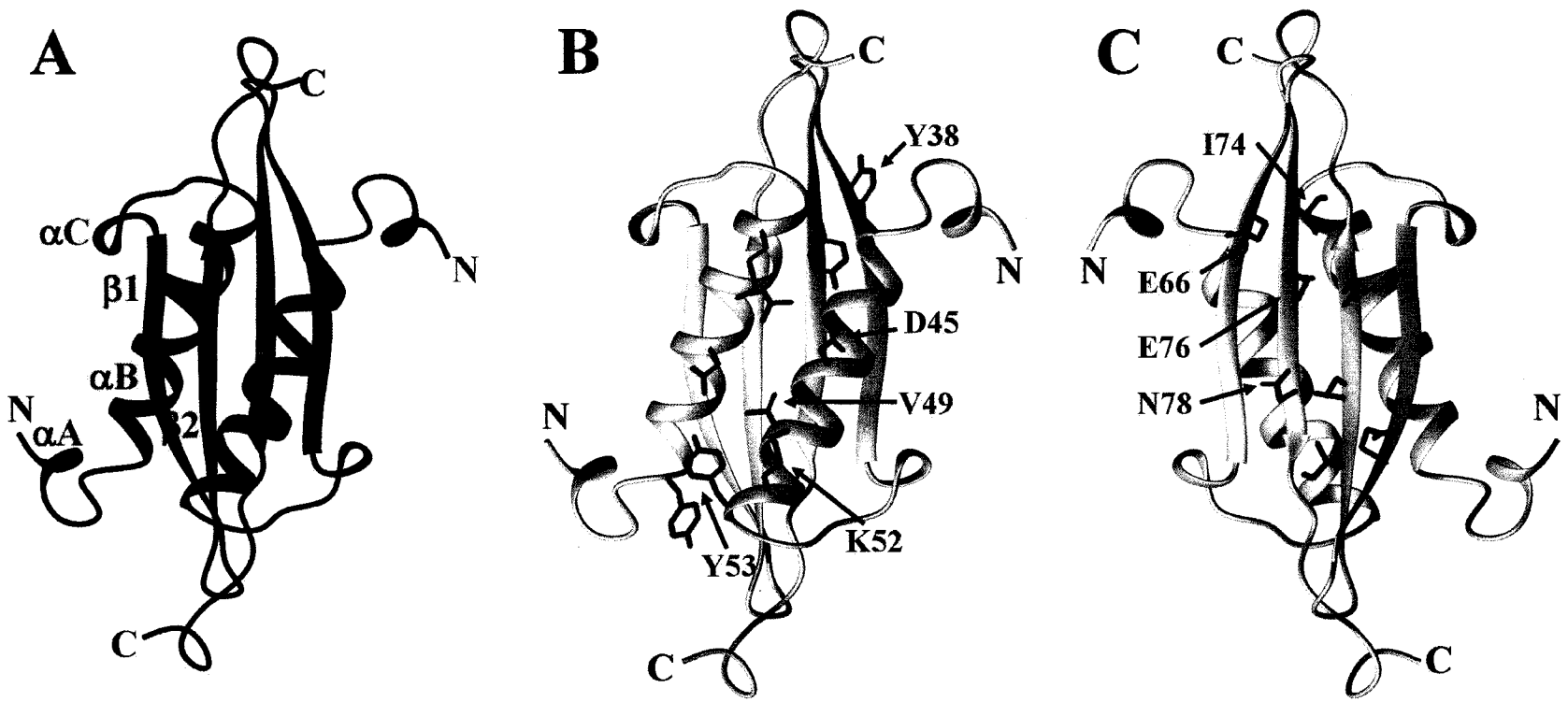

Figure 1.3: *Structure of the E. coli MinE^{TSD} (PDB# 1EV0).* ***A)*** *Ribbon diagram of the solution NMR structure of the TSD from the E. coli MinE (45) showing monomers in either red or blue.* ***B)*** *Location of conserved residues on the surface of E. coli MinE^{TSD} residues in the α-helix (Y38, D45, V49, K52, and Y53) and* ***C)*** *in the β-sheet (E66, I74, E76, and N78). Structure* ***A*** *has been rotated 180° about the long axis to give structure* ***C.***

Subsequent results obtained by Shih *et al.* provided additional insight into the functional role of these topological specificity-determining residues since replacement of the wild-type MinE with these mutants gave rise to a defect in the formation and stability of the E-ring (*10*). Also, while these mutants did not prevent the assembly and disassembly of MinD polar zones, there was a significant perturbation in the temporal and spatial regulation of these processes. This perturbation resulted in the continued growth of the polar zone beyond the normal stop point near the mid-cell and with the loss of normally ordered cycles of assembly and disassembly of the internal MinD zones (*15*). As a result, Shih *et al.* proposed that the major role of the TSD was to mediate the formation of the E-ring such that addition of new MinD molecules at the leading edge of the polar zone is prevented, thereby terminating polar zone growth (*10*).

Much less is known about the structure of the anti-MinCD domain. Trypsin degradation results suggested an absence of stable structure in the absence of MinD (*43-45*). However, since unstructured protein ligands tend to adopt specific conformations when bound to other proteins, experiments were performed to probe the structure of the anti-MinCD domain when bound to MinD (*44*). Specifically, yeast three-hybrid studies were done with a range of mutants of the anti-MinCD domain and a number of residues were identified that led to a complete or partial loss of MinD binding (*44, 45*). For example, the mutation of L22 to either glutamate or arginine led to a complete loss of anti-MinCD function (*44*). A18 and I25 were similarly shown to be critical for anti-MinCD function, while other residues (e.g. L4, I24 or A27) did not seem to be involved at all (*44*). The results of this mutational study were projected onto a helical model of this domain. In this model, all mutations that disrupted anti-MinCD function were found to localize to one face of the helix (*44*). This finding, along with secondary structure predictions based on

primary sequence, led to the proposal that the N-terminal domain forms a helical structure when bound to MinD (*43, 44*).

In spite of the abundance of structural data on the separate functional domains of MinE, these studies have not been able to reveal any insight into how these domains may behave in the full-length protein. For example, it is not known whether there are any interactions between the two domains that could modulate their respective functions. Resolution of this question would help to improve our understanding of how MinE performs its functions *in vivo*. Considering that it is still not known how topological specificity function is conferred by MinE, or whether part of the TSD might contribute to anti-MinCD function, it is clear that there is still much to learn about the molecular basis for MinE function. For these reasons, the primary focus of my thesis has been the structural analysis of the full-length MinE protein. As our lab was also interested in learning about the structure of a MinE protein from a bacterial species with a morphology that differs from that of the widely studied rod-shaped *E. coli* protein, we therefore focused our efforts on MinE from *N. gonorrhoeae* ($MinE_{Ng}$).

1.6 Structural and Functional Comparison of MinE from Round- versus Rod-Shaped Bacteria

Unlike the rod-shaped *E. coli*, *N. gonorrhoeae* is a coccus and therefore does not have definable poles. This raises questions concerning the mechanism of cell division septum placement in round cells and whether MinE proteins are also involved. The Dillon lab has done a lot of work in this area to answer this question and their results showed a large degree of functional similarity between Min proteins in rod-shaped and round cells.

In particular, they found that *E. coli* Min proteins are highly homologous to *N. gonorrhoeae* Min proteins and that Min proteins from one species are able to function with those from the other species (*48, 49*). In the case of $MinE_{Ng}$, they were able to show that it interacts with $MinD_{Ng}$ and can also functionally replace $MinE_{Ec}$ in *E. coli* (*48, 49*). This evidence of functional conservation suggested that the round- and rod-shaped proteins function in a similar manner. However, in this same study it was also shown that conserved residues that comprise part of the topological specificity domain (K53 and E67) in $MinE_{Ng}$ also influence binding to $MinD_{Ng}$ (*48, 49*). Mutations of these residues were found to drastically diminish the interaction between $MinE_{Ng}$ and $MinD_{Ng}$, a result that which had not been previously observed in the *E. coli* protein (*49*). This result suggests that there may be increased variation among MinE orthologues in the C-terminus and may reflect some differences and similarities in how MinE functions in round- and rod-shaped bacteria (*48*). Since differences in structure can provide some explanation for functional variation, the goal of this thesis is to characterize the conformation of $MinE_{Ng}$ and compare the result to the available data from $MinE_{Ec}$.

1.7 Thesis Objectives

Given the questions that still remain regarding the structure of full-length MinE, as well as the questions concerning functional differences between MinE and from round and rod-shaped cells, my work has focused on structural studies of $MinE_{Ng}$. The following objectives were therefore pursued in this work:

- generation of $MinE_{Ng}$ samples suitable for solution NMR studies

- determination of the secondary structure of full-length $MinE_{Ng}$
- investigation of the potential for inter-domain interactions in $MinE_{Ng}$

Results from these studies should help improve our understanding of the mechanisms that are involved in the regulation of cell division in round cells and to unravel the molecular basis of MinE function.

CHAPTER 2

INTRODUCTION Part 2:

Background to Methods Used for the Characterization of Protein Structure

In this thesis, two of the primary techniques used to characterize the structure of $MinE_{Ng}$ are circular dichroism (CD) and solution NMR. These two techniques provide complimentary information on a protein fold since CD accounts for global structural characteristics while NMR can provide highly localized information at an atomic level. In order to provide some insight in the utility and application of these techniques, this section will be devoted to a brief description of the origin and utilization of these two techniques.

2.1 Principles of Circular Dichroism Spectroscopy – Origin of the CD Effect

CD is a phenomenon that results from the interaction between asymmetrical molecules and plane-polarized light (*50-53*). Asymmetry can be conferred to molecules that have a restricted rotational arrangement that could result from strong intra-molecular interactions such as those found in a helical polypeptide structure (*50, 51*). When chromophores are in an asymmetrical environment, they will absorb left-circularly polarized light to a different extend than right-circularly polarized light. The CD signal is

defined as the differential absorption of these two different circularly polarized components of plane-polarized radiation:

$$\Delta\varepsilon(\lambda) = \varepsilon_L(\lambda) - \varepsilon_R(\lambda)$$

where ε_L and ε_R are the molar extinction coefficients of the left- and right-circularly polarized components at a specific wavelength, λ – where $\Delta\varepsilon$ is usually given in units of mol^{-1} L cm^{-1} (*50, 51*). If the left- and right-circularly polarized components are absorbed to the same extent this would give rise to zero CD signal (*51*). However, if the sample absorbs the right component more strongly than the left component, then it would give rise to a negative CD absorption while the opposite would be observed, if the left-handed component is more strongly absorbed than the right-handed component of circularly polarized light.

CD signals for proteins are most often reported in units of mean residue molar ellipticity, which is defined as follows:

$$[\theta]_{MRE} = \frac{100 \times \theta}{\mathbf{n} \times \mathbf{c} \times \mathbf{l}}$$

where **n**, **c** and **l** are the number of amino acid residues in the protein, protein concentration (M) and path length (cm), respectively, and $\theta = 3298 \times \Delta\varepsilon$. This unit of measurement reflects the fact that the peptide bond is the major absorbing species in proteins for CD spectra recorded in the range of 190 nm to 250 nm.

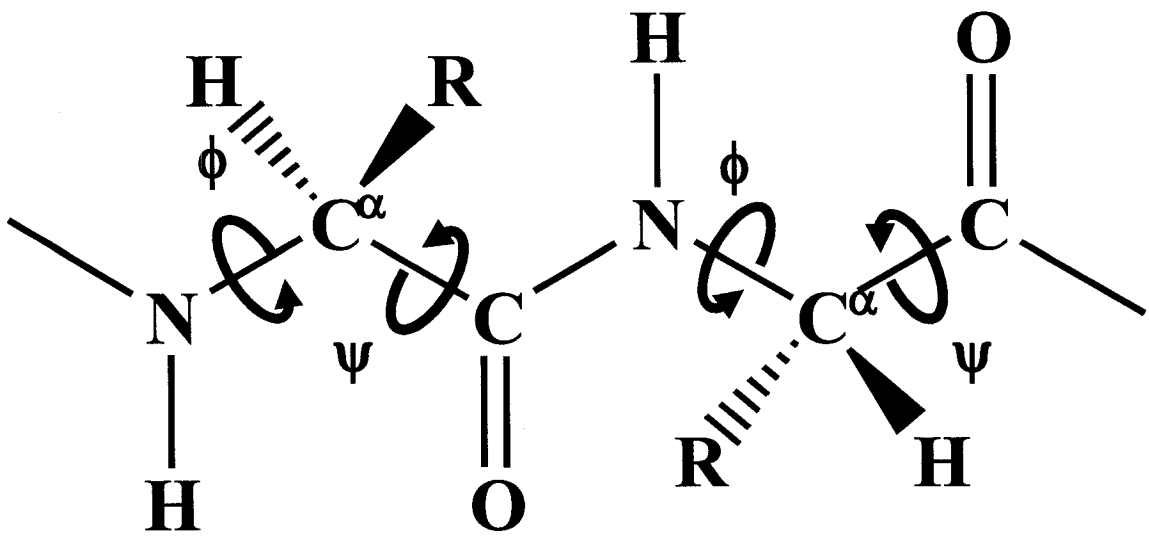

Figure 2.1: *The Peptide Bond is Rigid and Planar. Three bonds separate sequential C_α atoms in a polypeptide chain. The $N - C_\alpha$ and $C_\alpha - CO$ bonds can rotate with bond angles designated as phi (ϕ) and psi (ψ), respectively. By convention, both ϕ and ψ are defined as 180° when the polypeptide is in its fully extended conformation and all peptide groups are in the same plane.*

2.2 Characteristic CD Spectra of Protein Secondary Structures

The most commonly occurring secondary structures in proteins are α-helices and β-sheets. These secondary structures are characterized by a set of dihedral angles ψ and φ (Figure 2.1), which are typically in the range of ψ = -45°and φ = 60° for an α-helix (*54*). The dihedral angles ψ and φ for β-sheets tend to occur around -120° and 120°, respectively (*54*). In the α-helix conformation, the backbone amide protons are able to hydrogen bond with the carbonyl group 4 residues away in the sequence (Figure 2.2). The result is a rigid rod-like structure with the amino acid side chains projecting away from the main helix axis

(*54*). In contrast, β-strands form hydrogen bonds with other β-strands and side chains project both above and below the plane of the sheet (*54*). Amino acid residues that lack any of the stable conformations mentioned above are described as unordered or random coil structures.

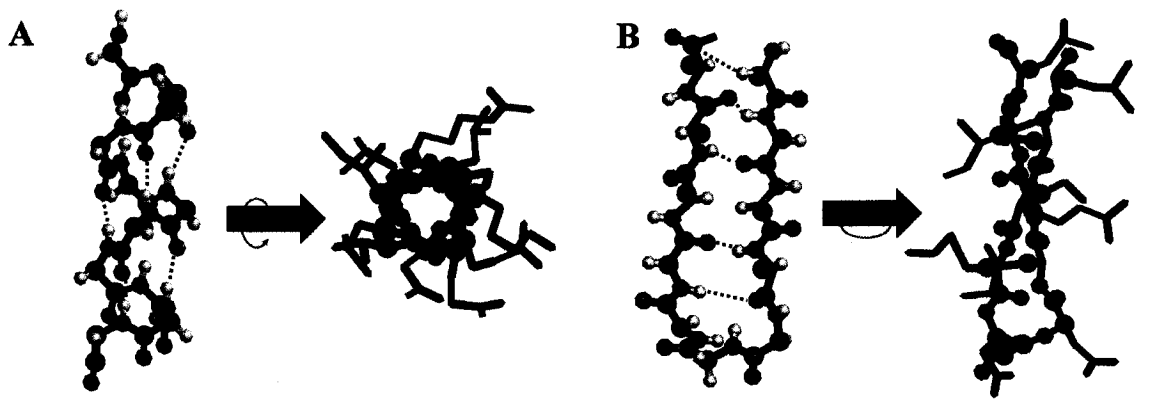

Figure 2.2: *Ball and stick model of two views of representative* ***A)*** *α-helical and* ***B)*** *β-sheet secondary structures generated by MOLMOL (55). Side chains are shown in green neon.*

The far-UV CD (i.e. 190 – 250 nm) region of a protein CD spectrum is reflective of the total secondary structure content because the dominant contribution is from the amide bonds (*50, 51*). Consequently, characterization of protein secondary structure by this technique benefits from the remarkable sensitivity of the spectrum to conformational changes within the protein. As a result, different types of protein secondary structure give rise to the characteristic CD shown in Figure 2.3. For example, the CD spectrum of an α-helical protein displays characteristic minima at approximately 222 nm and 208 nm and a maximum at approximately 192 nm reflecting the $n \rightarrow \pi^*$ and $\pi \rightarrow \pi^*$ transitions of the

oxygen non-bonding or carbonyl π electrons, respectively (*51, 56*). In contrast, these electronic transitions give rise to a CD with a different spectrum for a typical β-sheet conformation, with a minimum at approximately 215 nm and a maximum at approximately 198 nm (*51, 56*). Finally, the CD spectrum for a typical random coil conformation shows a weak positive signal at approximately 226 nm and a strong negative signal at approximately 205 nm (*51, 56*).

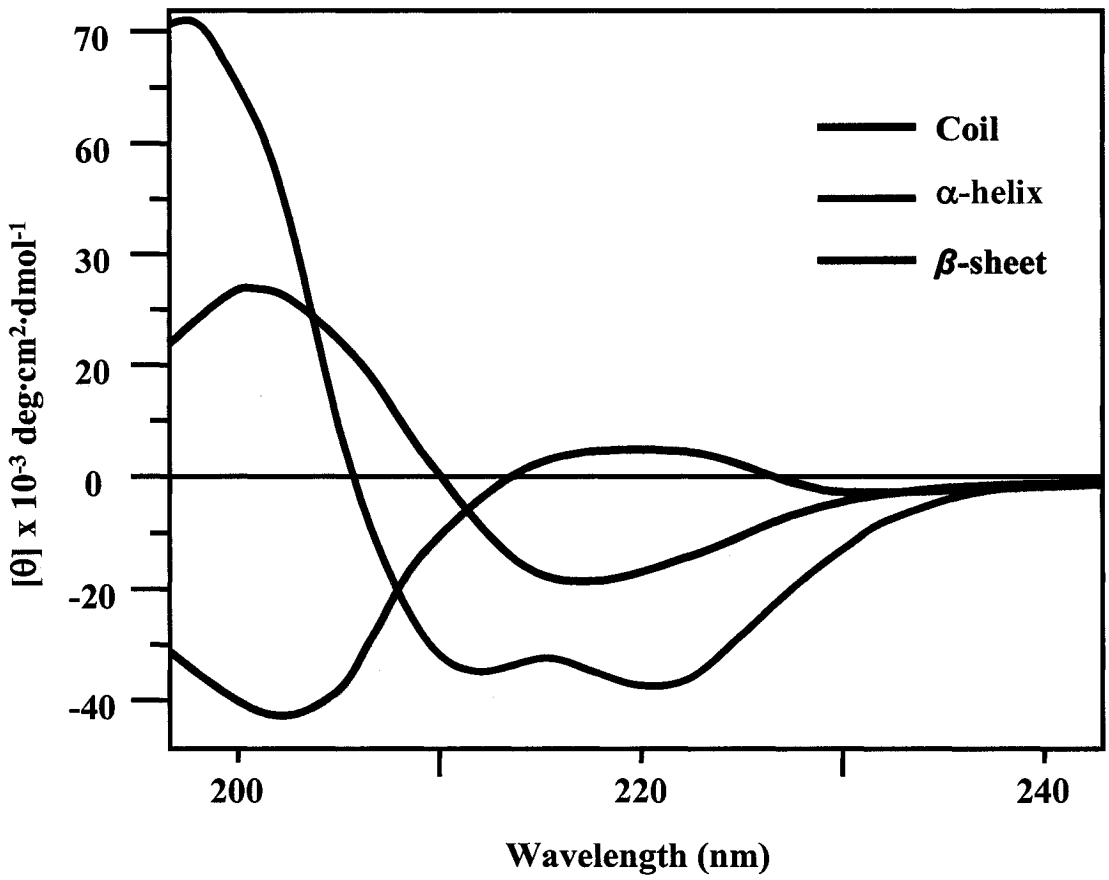

Figure 2.3: *Characteristic CD Spectra for α-helix (red), β-sheet (blue) and random coil (green) conformations (57). (Adapted from "Proteins: Structures and Molecular Properties, by T.E. Creighton).*

Given the fact that different secondary structure types produce characteristic spectra, it is possible to extract secondary structure estimations by spectral deconvolution programs such as CDPro (*58-60*). These types of programs use algorithms that refer to a dataset of reference CD spectra of proteins for which high resolution structures have been determined. Linear combinations of reference spectra are fit to input CD data to estimate the secondary structure content of the protein under investigation (*58-60*). Although the accuracy of secondary structure estimations using CD spectral deconvolution will depend of the suitability of the reference spectra used to reproduced the spectrum under investigation, these methods generally have success rate of ~75% and higher (*56, 61*). Therefore, spectral deconvolution techniques can provide a reasonable estimate of the secondary structure content of a protein of unknown structure.

2.3 NMR Spectroscopy – The $^{1}H - ^{15}N$ HSQC

Solution NMR of proteins offers an advantage over global spectroscopic methods such as CD in that structural information can be obtained at an atomic level (*62-66*). However, in order to extract this information, it is necessary to identify the atoms that give rise to each peak in the spectrum. In order to gain insight into the backbone conformation of $MinE_{Ng}$, we assigned chemical shifts for all observable backbone $^{13}C_{\alpha}$, $^{13}C_{\beta}$, ^{13}CO, ^{15}N and $^{1}H^{N}$ atoms (*62-64*). This can be done by using a standard set of triple-resonance multidimensional experiments that will be outlined in this section.

The basis for all the NMR experiments used in triple resonance backbone chemical shift assignment is also a widely used two-dimensional heteronuclear experiment for

proteins; the $^{1}H^{N}$ – ^{15}N HSQC (heteronuclear single quantum coherence) spectrum (*62, 63*). In this experiment, the amide proton chemical shift is correlated with the chemical shift of the directly attached nitrogen atom. The result is a peak at the intersection of the chemical shift of the amide proton (x-axis) and that of the bonded amide ^{15}N (y-axis). This $^{1}H^{N}$ – ^{15}N HSQC experiment provides what is often referred to as the "fingerprint spectrum" for a protein since each protein gives rise to a unique pattern of peaks.

The $^{1}H^{N}$ – ^{15}N HSQC spectrum has the additional feature that it can be used to evaluate the structural integrity of the protein of interest (*65*). Since this spectrum should show one peak for each proton that is directly bound to an amide proton, the number of peaks from the backbone amides should equal the number of non-proline amino acids present in the protein primary sequence in the spectrum. If a significant number of expected peaks are not present in the spectrum, this could be indicative of intermediate time-scale (e.g ns – ms) conformational or chemical processes (*62-66*). Alternatively, missing peaks could be indicative of aggregation, which could increase the molecular mass to the point where the NMR signal can no longer be detected (*63*). In addition to the peak number, the dispersion of peaks in the spectrum can also provide an indication of how a protein is folded. Specifically, if the proton chemical shifts span a wider range (> ~1 ppm) then this is good evidence that the protein is properly folded. However, proteins that are in an unfolded state usually have sharp resonances that have a narrow range of $^{1}H^{N}$ chemical shifts (~ 0.5 – 1 ppm). Therefore, the appearance of the ^{1}H – ^{15}N HSQC can rapidly provide a diagnostic view of the folding state for protein samples.

2.4 *Multi-Dimensional NMR Spectroscopy – Heteronuclear Correlations*

Once the initial $^{1}H^{N}$ – ^{15}N HSQC spectra have been recorded, and it has been established that the sample is properly folded, then a number of three-dimensional experiments can be run to perform backbone chemical shift assignment. These experiments are similar to the two-dimensional experiment; however, an additional chemical shift dimension is recorded such that the peaks now appear as spots in a three-dimensional cube. This allows the chemical shift of three or more different atoms to be correlated in a single experiment.

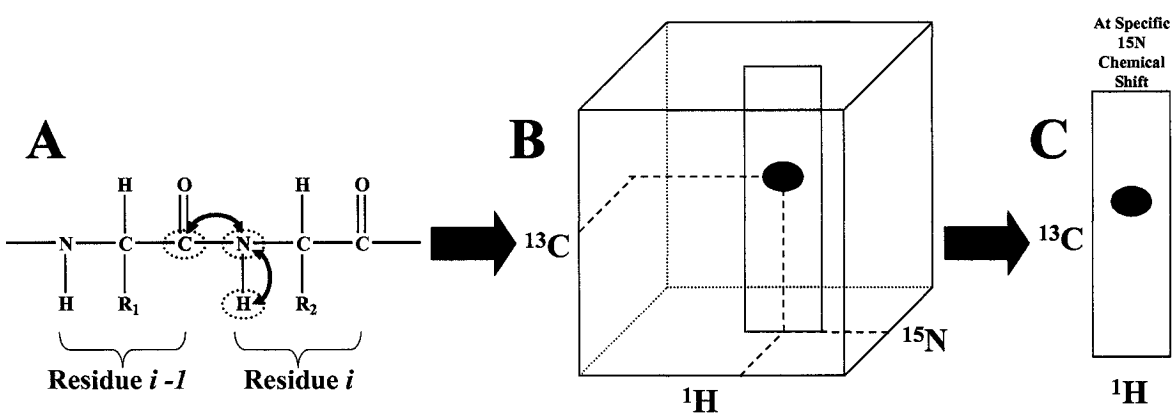

Figure 2.4: *HNCO Backbone Correlation Experiment.* ***A)*** *Magnetization transfer - In the HNCO experiment the magnetization is transferred from the $^{1}H^{N}$ (i position) proton via the ^{15}N atom to the directly attached ^{13}CO from the preceding residue (i-1) and is returned via the same path. The chemical shifts of all three nuclei, highlighted in yellow, are recorded in this experiment.* ***B)*** *Schematic view of a simplified 3D HNCO spectrum that would arise from a 2 amino acid long peptide. The position of this spot in the cube will be determined by the chemical shift of the $^{1}H^{N}$, its directly attached ^{15}N and the ^{13}CO from the preceding residue.* ***C)*** *$^{1}H - ^{13}C$ strip plot to simplify visualization of the spectrum.*

Table 2.1: Triple Resonance Experiments Used for Backbone Sequential Assignment

Experiments	Magnetization transfer pathway*	Correlations Observed
HSQC	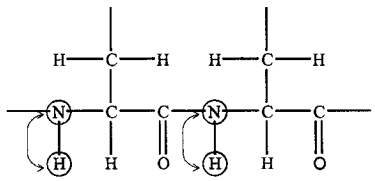	$^{1}H_{i}^{N}-^{15}N_{i}$
HNCO	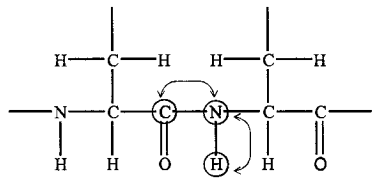	$^{1}H_{i}^{N}-^{15}N_{i}-^{13}CO_{i-}$
HN(CO)CA	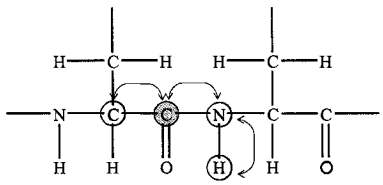	$^{1}H_{i}^{N}-^{15}N_{i}-^{13}C_{i-1}^{\alpha}$
HNCACB	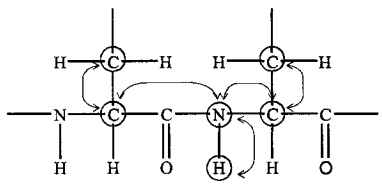	$^{1}H_{i}^{N}-^{15}N_{i}-^{13}C_{i}^{\alpha}/^{13}C$ $^{1}H_{i}^{N}-^{15}N_{i}-^{13}C_{i-1}^{\alpha}/^{13}C$
CBCA(CO)NH	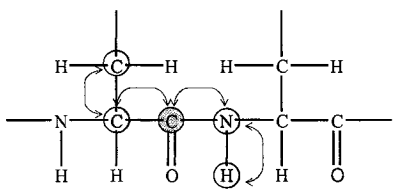	$^{13}C_{i-1}^{\alpha}/^{13}C_{i-1}^{\beta}-^{15}N_{i}-^{1}H$

**Yellow indicates atoms for which chemical shifts are recorded, blue highlights atoms through which magnetization is relayed but no chemical shift is recorded.*

One of the most commonly used and sensitive three-dimensional experiments is called the HNCO (*62-64*). In this experiment, the chemical shift of a backbone carbonyl atom is correlated with the chemical shift of the directly bonded amide nitrogen, which in turn is correlated with that of the amide proton (Figure 2.4). This will appear as a spot in a $^{1}H - ^{15}N - ^{13}C$ cube where the chemical shifts of these atoms can be obtained from the position of this spot in the cube. It is possible to simplify display of these correlations by using an NMR visualization program such as NMRView, so that strips containing the peaks can be extracted instead of analyzing the data within the cube. These strips represent two-dimensional slices taken at specific chemical shift values from the third dimension. For the HNCO, strips are typically used to show the correlation between ^{1}H and ^{13}C chemical shifts at a specific ^{15}N chemical shift.

As shown in Table 2.1, the nomenclature for triple resonance experiments used in backbone assignment reflects the magnetization transfer pathway used to obtain the spectrum (*64*). Nuclei that are correlated in the experiment are listed and nuclei that filter these chemical shifts without their chemical shifts being recorded themselves are indicated in parentheses. This was the nomenclature system used for the HNCO, as can be determined from the output of the experiment (i.e. the amide proton (H) is correlated to amide nitrogen (N) and the carbonyl carbon (CO)) (*62, 64*). Similarly, an experiment that correlates the amide proton chemical shift (H) with that of the directly bonded amide nitrogen (N) and the directly bonded α-carbon (CA) would be called HNCA (*62, 64*). In this case, however, there is significant through-bond coupling not only between the CA that is directly bonded to the nitrogen (intra-residue) but also through the carbonyl atom the CA of the previous residue (inter-residue). Therefore, in this experiment, there should be two

peaks in the carbon dimension at a single ^{1}H and ^{15}N chemical shift corresponding to the intra- and inter-residue correlations (Figure 2.5). It is also possible to perform an experiment that selectively relays magnetization through the carbonyl prior to acquisition of carbon chemical shift to provide only the inter-residue correlation in an experiment is called the HN(CO)CA (*62, 64*).

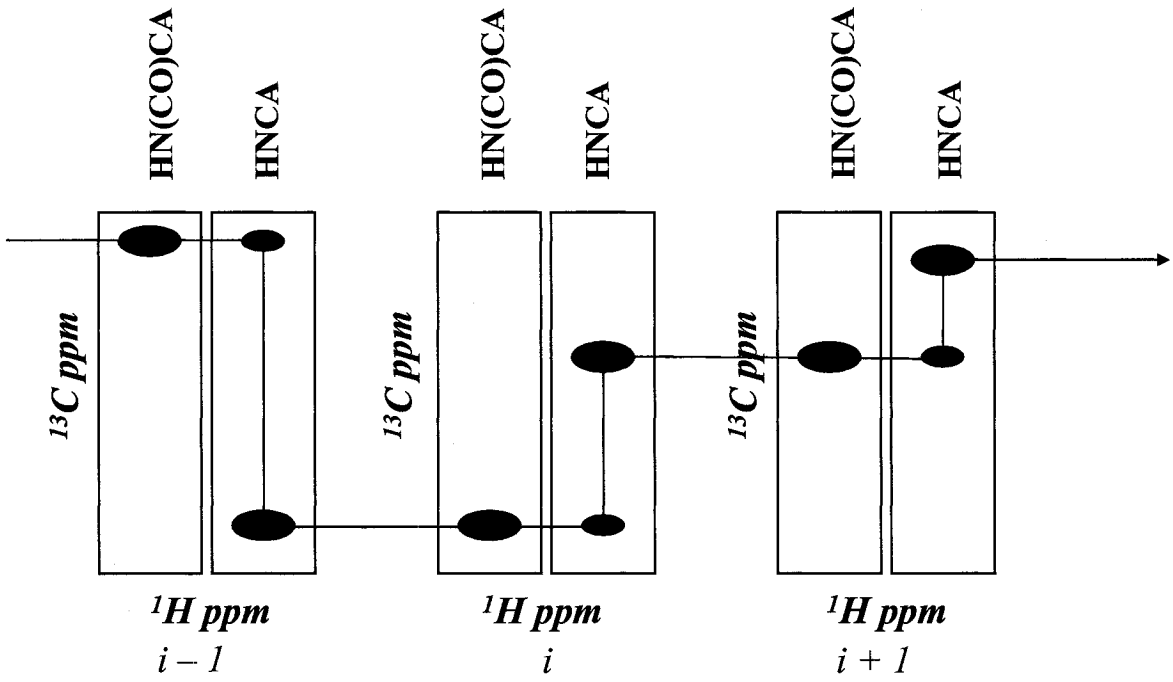

Figure 2.5: *Sequential Assignment Using HNCA and HN(CO)CA Experiments – $^{1}H - ^{13}C$ strips for the HNCA and HN(CO)CA are shown for three sequential residues (i-1, i, i+1) in a protein sequence. The red arrows represent the sequential connectivities between intra- and inter-residue $^{13}C_{\alpha}$ chemical shifts. In the HNCA each residue shows peaks corrsponding to the inter- and intra-resdidue $^{13}C_{\alpha}$. The HN(CO)CA only shows the $^{13}C_{\alpha}$ correlations from the preceding residue. Intra-residue correlations in the HNCA (larger peaks) strips are matched to inter-residue corraltions in the HN(CO)CA stips to determine the order in which the strips should be placed.*

2.5 *Sequential Backbone Assignment Using Triple-Resonance Experiments*

The ability to record triple resonance experiments such as the HNCA allow correlations not only to be made within amino acid residues but also between sequential residues (*62-64*). This combination of information provides a way to identify the resonances that come from amino acids that are adjacent in the protein sequence. An example of how this works is shown for three consecutive residues in Figure 2.5. In this example, strips have been extracted for these three residues from an HNCA spectrum. Beside each HNCA strip is the corresponding strip extracted from the HN(CO)CA. It is centered at the same ^{1}H chemical shift and extracted from the same ^{15}N plane as that from the HNCA, however, only one peak is observed; that of the C_α from the preceding residue. The carbon chemical shift of this peak is identical to that of the smaller peak in the HNCA strip thereby confirming that the smaller HNCA peak is actually that of the inter-residue C_α (*62-64*). The larger peak in the HNCA strip therefore corresponds to the intra-residue correlation. In order to find the corresponding chemical shifts for the next amino acid in the sequence (*i+1*), it is necessary to find an HN(CO)CA strip containing a peak at this carbon chemical shift (*62-64*). The corresponding strip from the HNCA can then be used to determine ^{1}H, ^{15}N and $^{13}C_\alpha$ chemical shifts of this adjacent (C-terminal side) residue. This process can be repeated to find the chemical shifts of the proceeding amino acids until all backbone $^{1}H^{N}$, ^{15}N and $^{13}C_\alpha$ chemical shifts are assigned.

Separation of peaks in the $^{13}C_\alpha$ spectrum can be poor in some cases increasing the possibility that multiple strip sequences could be proposed for a particular protein. One way to help resolve these ambiguities is to record experiments that have an even larger number of correlations within and between residues. Most common among these are the

HNCACB and the CBCA(CO)NH (*62-64*). The experiments are almost identical to the HNCA and HN(CO)CA experiments, respectively, except that peaks arising from $^{13}C_{\beta}$ atoms are also obtained. As shown in Figure 2.6, this creates additional information to help match the strips by reducing the ambiguity that could arise from proteins containing a number of amino acids with similar $^{13}C_{\alpha}$ shifts.

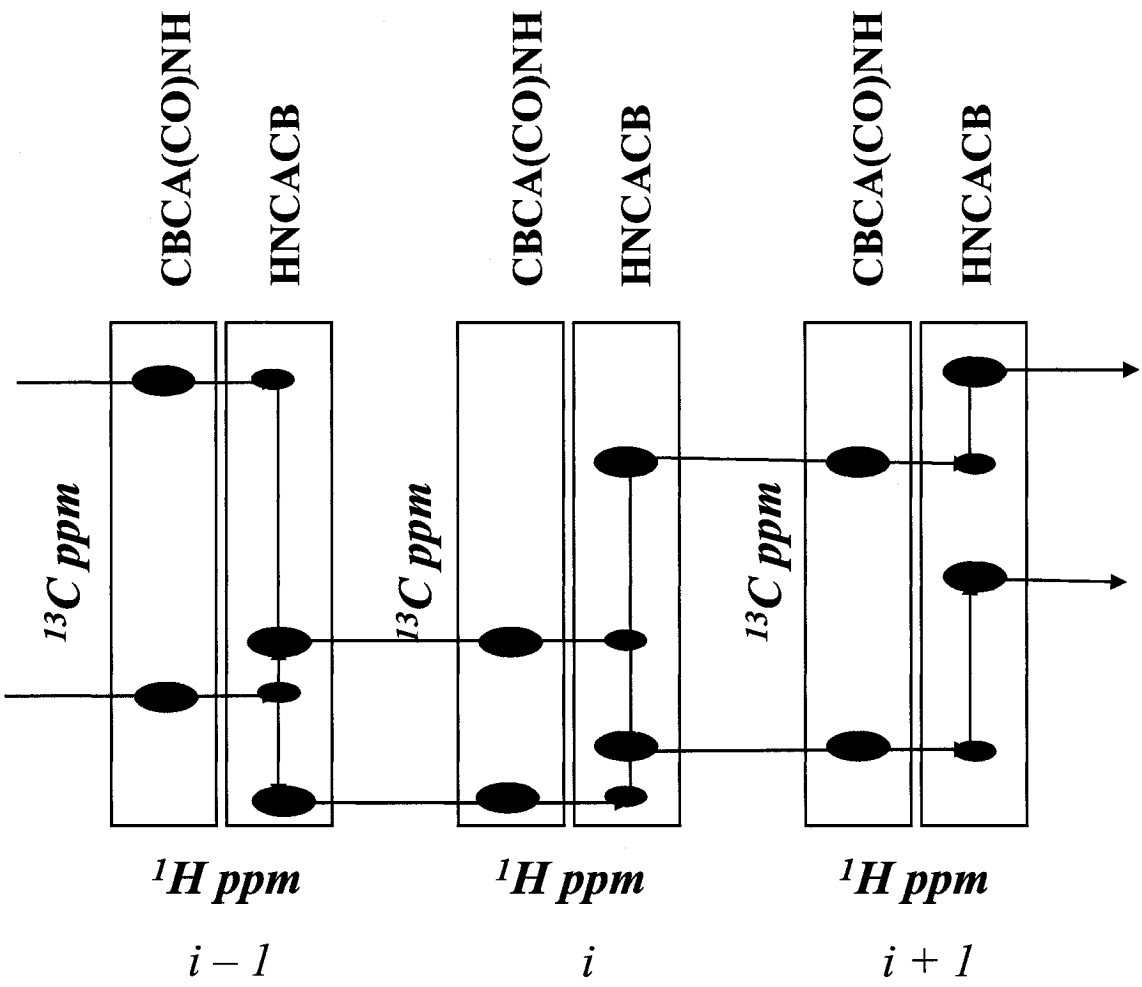

Figure 2.6: *Sequential Assignment Using CBCA(CO)NH and HNCACB Spectra – Each strip represents a $^{1}H^{N}$ – ^{13}C plane at a specific ^{15}N shift. Negative intensity peaks are shown in red and correspond to $^{13}C_{\beta}$ correlations in the HNCACB spectrum. The red arrows represent the sequential connectivities between the intra- and inter-residue $^{13}C_{\alpha}$ chemical shifts. The black arrows represent the connectivities between the $^{13}C_{\beta}$ chemical shifts.*

Table 2.2: Typical $^{13}C_\alpha$ and $^{13}C_\beta$ Chemical Shift Ranges from Proteins (62, 67)

Residue	*$^{13}C\alpha$ Chemical Shifts*	*$^{13}C\beta$ Chemical Shifts*
Alanine	55 – 50 ppm	22 – 16 ppm
Cysteine	60 – 55 ppm	46 – 38 ppm^{ox} 32 – 26 ppm^{red}
Aspartic acid	56 – 52 ppm	42 – 38 ppm
Glutamic acid	59 – 54 ppm	32 – 28 ppm
Phenylalanine	60 – 55 ppm	42 – 38 ppm
Glycine	47 – 44ppm	–
Histidine	58 – 53 ppm	32 – 37 ppm
Isoleucine	64 – 59 ppm	41 – 36 ppm
Lysine	59 – 54 ppm	35 – 30 ppm
Leucine	57 – 52 ppm	45 – 40 ppm
Methionine	57 – 53 ppm	36 – 30 ppm
Asparagine	56 – 51 ppm	40 – 36 ppm
Proline	64 – 61 ppm	34 – 30 ppm
Glutamine	58 – 54 ppm	34 – 32 ppm
Arginine	59 – 54 ppm	32 – 28 ppm
Serine	65 – 60 ppm	60 – 56 ppm
Threonine	71 – 68 ppm	64 – 59 ppm
Valine	64 – 59 ppm	35 – 31 ppm
Tryptophan	59 – 54 ppm	30 – 28 ppm
Tyrosine	59 – 54 ppm	42 – 37 ppm

Other information that is also used to facilitate the assignment process is a general database of typical chemical shift values for each atom in each amino acid (*62, 67*). In particular, ^{13}C chemical shift data has proven to be a particularly useful tool for the identification of amino acid identities since amino acids tend to exhibit a characteristic range of chemical shifts, as shown in Table 2.2. The distinctive $^{13}C_\alpha$ and $^{13}C_\beta$ chemical shifts of alanine, threonine, serine and glycine residues are especially useful in the identification of the amino acid types. This information is usually coupled with the

alignment of sequentially connected strip plots to allow correlations with the known amino acid sequence as required for unambiguous assignment of backbone chemical shifts.

2.6 Secondary Structure Determination from Assigned Backbone Chemical Shifts

Once backbone chemical shifts have been assigned for a protein, it is possible to use this data to characterize protein secondary structure. This is generally done by calculating the secondary chemical shifts from random coil values as originally described by Wishart *et al.* (*68-70*). Since backbone atoms in proteins experience an upfield or downfield shift relative to their random coil values that heavily depends upon the type of secondary structure they are in, subtraction of random coil amino acid specific shifts from experimental values can provide an accurate prediction of secondary structure. The predictive power of this secondary shift calculation improves as wider ranges of backbone atoms are included in the analysis (*68, 69, 71*). For example, both $^{13}C_{\alpha}$ and ^{13}CO atoms tend to experience an upfield shift in α-helices and a downfield shift in β-strands. Therefore, observation of positive secondary chemical shift for both atoms would provide a strong indication of α-helical structure while negative shifts would suggest β-stand structure.

2.7 Application of CD and Solution NMR to $MinE_{Ng}$

In order to meet the thesis objectives outlined in Chapter 1, we have used the biophysical techniques outlined in this chapter. Specifically, ^{15}N- and ^{13}C-labeled $MinE_{Ng}$

was prepared, backbone chemical shifts were assigned and secondary chemical shifts were calculated to probe the conformation of full-length $MinE_{Ng}$. CD spectroscopy was used concurrently to evaluate the total secondary structure of $MinE_{Ng}$ under the range of conditions tested by NMR. The potential for inter-domain interactions within $MinE_{Ng}$ was also investigated by applying these two techniques to $MinE_{Ng}$ mutants. Overall, the results from these studies gave rise to new insights into MinE structure and function as will be described in the subsequent chapters.

CHAPTER 3

MATERIALS AND METHODS

3.1 Bacterial Plasmids

All plasmids used in this study were provided by the Dillon lab (*49*) except for the E46A mutant which was generated by Ms. Jenny Cheng, a Master's student in the Goto lab (*72*). The wild-type plasmid (pEC1) had been generated by inserting DNA encoding a C-terminally hexahistidine-tagged $MinE_{Ng}$ sequence into the pET30a expression vector (Novagen, Madison, WI) at the *NdeI* and *XhoI* restriction sites. Mutations A18D, L22D or E46A were introduced into the wild-type sequence using the QuickChange® Site-Directed Mutagenesis Kit as described by the manufacturer (Stratagene). The resulting plasmids contained a kanamycin resistance marker and placed the His-tagged MinE protein under the control of the T7 RNA polymerase promoter. The identity of all DNA constructs used in this thesis was confirmed by sequencing performed at the Ontario Genomics Innovation Centre at the Ottawa Health Research Institute and master stocks of sequenced DNA was used throughout these studies.

3.2 Bacterial Growth Media

Minimal (M9) media (*73*) was used to culture bacteria used for protein expression. A concentrated 10X M9 Salts solution containing 479 mM of dibasic sodium phosphate

(Sigma Aldrich), 220 mM of monobasic potassium phosphate (Sigma Aldrich) and 87 mM of sodium chloride (Sigma Aldrich) was prepared in MilliQ-pure water and sterilized by autoclave. Separate stock solutions were also prepared with 30% (w/v) glucose (Sigma Aldrich), 10% (w/v) ammonium chloride (Sigma Aldrich), 1 M magnesium sulphate (Sigma Aldrich) or 100 mM calcium chloride (Sigma Aldrich) and filter-sterilized through a 0.22 μm filter. These solutions were all used to make the final media used in expression containing: 1X M9 salts, 0.1% (w/v) NH_4Cl, 0.3% (w/v) glucose, 0.01X Gibco MEM Vitamin Solution (filter-sterilized in a 0.22 μm filter), 1 mM $MgSO_4$, 100 μM $CaCl_2$, and 50 μg/mL kanamycin. The final pH of the media was between 7.2 and 7.4. For the production of ^{15}N and ^{13}C-labelled MinE, $^{15}NH_4Cl$ (Cambridge Isotope Laboratories) and ^{13}C-glucose (Cambridge Isotope Laboratories) were used as the sole nitrogen and carbon sources, respectively.

The growth media used to prepare competent cells and for transformation was Luria-Bertani (LB) broth and agar. For LB broth, 10 g of tryptone, 5 g of yeast, 5 g of NaCl and 1 mL of 1 M NaOH were mixed together and the volume was brought up to 1 L with MilliQ-pure water. The LB agar was prepared in the same manner as the LB broth except 15 g of agar was added for every 1 L of LB broth. Both LB broth and agar were sterilized by autoclaving and allowed to cool down before adding the appropriate antibiotic.

3.3 Preparation of Competent Cells

Competent cells for $CaCl_2$ transformation were prepared according to established methods (*74, 75*). In this method, competent *E. coli* BL21 and DH5α strains were streaked

on a non-selective agar plate and incubated at 37°C overnight. One colony was used to inoculate 50 mL LB broth, which was allowed to grow overnight at 37°C shaking at 220 rpm. 2 mL of overnight culture was used to inoculate 200 mL of fresh LB broth and grown at 37°C with shaking at 220 rpm to an optical density at 600 nm (OD_{600}) of 0.3 – 0.4. The culture was transferred into four sterile 50 mL Falcon tubes and spun in a Beckman-Coulter Spinchron centrifuge at 6,000 rpm for 10 min at 4°C. The supernatant was discarded under sterile conditions and the bacterial pellet was *gently* resuspended in 12.5 mLs of cold 100 mM $MgCl_2$. The cells were then pelleted by centrifugation at 5000 rpm for 10 min at 4°C. The supernatant was discarded and the pellets were *gently* resuspended again in a sterile 25 mL 100 mM $CaCl_2$ at 4°C. The resuspended competent cells were allowed to incubate on ice for at least 20 minutes prior to centrifugation at 5,000 rpm for 10 min at 4°C. The supernatant was discarded and the competent cells were again *gently* resuspended in sterile 1 mL solution of 85 mM $CaCl_2$ in 15% (v/v) glycerol. Approximately 100 µL aliquots of competent cells were transferred in sterile 1.5 mL microfuge tubes and flash-frozen with liquid nitrogen. The competent cells were stored in -80°C freezer.

3.4 Transformation of Bacterial Plasmid DNA into E. coli

Transformation was done using the $CaCl_2$ method (*76*). Briefly, 1 µL of 10 ng/uL of plasmid stock was added to 20 µL of competent *E. coli* and allowed to incubate on ice for 30 minutes. The cells were then heat-shocked in a 42°C water bath for one minute and then stored on ice for another minute. These cells were then added to 200 µL of LB broth and incubated for one hour at 37°C shaking at 220 rpm. The culture was plated onto an LB

agar containing the antibiotic for which resistance was conferred by the plasmid being introduced. The plates were allowed to incubate overnight at 37°C.

3.5 Plasmid Mini-Preps

The boiling lysis method was used to isolate plasmid DNA (*76*). In this method, 15 mL LB broth in a 50 mL Falcon tube was inoculated with a colony from a freshly transformed *E. coli* DH5α plate. The cultures were allowed to grow overnight at 37°C with shaking at 220 rpm. 1.5 mL of overnight culture was then transferred into a sterile microfuge tube and the cells were pelleted using a Beckman-Coulter Spinchron centrifuge at 14,000 rpm for 20 sec at 4°C. The cell pellets were resuspended in 300 uL of STET solution (10 mM Tris-Cl pH 8.0, 1 mM EDTA, 100 mM NaCl and 5% (v/v) Triton X-100) and 45 mM of lysozyme (Sigma) and then incubated in a boiling water bath for exactly 40 sec. Cell debris was pelleted at 12,000x*g* for 10 min at room temperature and removed using a sterile toothpick. Plasmid DNA was precipitated by adding 40 μL of 2.5 M sodium acetate at pH 5.2 and 420 μL of isopropanol to the supernatant followed by centrifugation at 12,000x*g* for 5 min at 4°C. The supernatant was *gently* removed and the DNA pellet was allowed to air dry. The pellet was then washed with 1 mL 70% ethanol and spun at 12,000x*g* for 2 min at 4°C. The supernatant was carefully removed and the tubes containing the plasmid DNA were placed face down on Kimwipes to remove excess ethanol. The nucleic acids were redissolved in the 50 μL TE buffer (containing 10 mM Tris pH 8.0, 1 mM EDTA and 20 μg/mL DNAase-free pancreatic RNAase). When necessary (e.g. for DNA sequencing), plasmid DNA was further purified using the Sigma-

Aldrich GenElute™ PCR Clean-Up kit. Procedures were followed as specified in the manufacturer's protocol.

3.6 Agarose Gel Electrophoresis for DNA Analysis

To analyze the purity of plasmid DNA, a 1% agarose gel was prepared in 1X TAE buffer (40 mM Tris, 20 mM Acetate, 2.5 mM EDTA pH 7.6 – 7.8). The DNA samples were prepared in loading buffer (0.02% (w/v) bromphenol blue, 0.02 mM EDTA pH 8.0 and 10% (v/v) glycerol) and loaded on the agarose gel submerged in 1X TAE buffer, which was then run at 100 V for 30 min, followed by staining with 2.5 μM ethidium bromide in 100 mL of 1X TAE for 10 min and destaining in water for 10 min.

3.7 Overxpression of Recombinant Gonococcal MinE

Since transcription of the $MinE_{Ng}$ gene is under the control of the T7 promoter, a T7 lysogen of *E. coli* must be used to express the protein. For this purpose, we used the commercially available BL21 (DE3) strain (Novagen). In this bacteria, protein expression is activated by addition of non-hydrolyzable analogues of galactose such as IPTG (isopropyl-β-D-thiogalactopyranoside) to the expression media. These compounds bind to the lacI repressor, which is bound to regions of the plasmid DNA that are upstream of the sequence to be expressed. Interactions with lactose or IPTG cause lacI to dissociate from the DNA allowing transcription to occur (*77*).

To express $MinE_{Ng}$, a freshly transformed BL21 (DE3) colony was used to inoculate 50 mL of M9 minimal media and allowed to incubate overnight at 37°C for 20 hours with shaking at 220 rpm. 30 mL of this overnight culture was transferred into a fresh 1 L of M9 minimal media, grown to an OD_{600} of 0.6 – 0.8 and then induced with 0.4 mM IPTG for 3 hours. After IPTG induction, the cells were harvested by centrifugation at 6,000 rpm for 10 min at 4°C and the cell pellet was stored at -20°C for future use

3.8 Purification of $MinE_{Ng}$ by Nickel Affinity Chromatography

Cells produced from 1 L expression media were thawed on ice and resuspended in 30 mL binding buffer (50 mM sodium phosphate, 10 mM imidazole, 300 mM NaCl, pH 8.0). 500 µL of 10 mg/mL lysozyme was added for every liter of culture and then placed on a rotating platform for 15 – 30 minutes at 4°C. The cells were lysed using a Fischer Scientific 500 Sonic Dismembrator at 60% power (amplitude) for 20 seconds on ice six to eight times. The sonicator tip was cooled in ice water for about 30 seconds and the cells were also kept cooled at 4°C between sonications. The insoluble material was pelleted by centrifugation at 16,000 rpm at 4°C for 35 minutes and the supernatant was collected for further purification.

3 – 6 mLs of Ni-NTA (Novagen) slurry was transferred into a column and rinsed with 20 mL of water, followed by 15 mL binding buffer. The resin was resuspended with the cell lysate and transferred into a 50 mL Falcon tube. The suspension was allowed to equilibrate on a rotating platform at 4°C for 1 – 1.5 hours and then transferred back into the column to allow the lysate to be separated from the resin. To ensure complete binding of

the His-tagged MinE, the flow-through was re-applied into the column. The column was then rinsed with 30 mL binding buffer and washed with another 30 mL wash buffer (50 mM sodium phosphate, 75 mM imidazole, 300 mM NaCl, pH 8.0). $MinE_{Ng}$ was then eluted with 30 mL of elution buffer (50 mM sodium phosphate, 250 mM imidazole, 300 mM NaCl, pH 8.0). The fractions containing MinE were pooled together (typically 50 mL) and dialyzed in a 4 L buffer containing 50 mM Tris, 50mM NaCl, 1 mM EDTA pH 9.5.

An AKTA–FPLC-based method using the HisTrap® column (GE Health Sciences) was also developed as an alternative (automated) purification. In this method, a 1 mL HisTrap® (Pharmacia) column was equilibrated in 20 mM sodium phosphate, 10 mM imidazole, 500 mM NaCl, pH 8.0. The cell lysate was filtered with 0.22 μm filter and loaded into the column at a rate of 1 mL/min. The column was washed with the same buffer for 12 column volumes (cv). The imidazole concentration was then increased to 100 mM and the column was washed for another 10 cv. The imidazole concentration was increased to 500 mM and the column was washed for 15 cv. Purified $MinE_{Ng}$ obtained by either method was >90% pure based on SDS-PAGE analysis (Section 3.15). When necessary, protein samples were concentrated in a 15 mL 5K MWCO Amicon Ultra centrifugal filter device.

3.9 Optimization of Protein Solubility

To assess the protein solubility of MinE, a range of buffer, pH and salt conditions were evaluated. When buffers with pH conditions above 7.0 were evaluated, protein samples were introduced into the new buffer using dialysis with tubing of MWCO 5 kDa

(Spectrapore). For samples to be analyzed below pH 7.0, the protein sample was diluted two-fold with H_2O to reduce the possibility of aggregation and then dialyzed against 100 equivalent volumes of buffer. For samples to be transferred into acetate buffer, the protein sample was diluted again in 1:1 v/v ratio with 200 mM acetate and 100mM NaCl pH 4.0, with the final pH being approximately 4.4 prior to dialysis.

3.10 Size-Exclusion Chromatography of $MinE_{Ng}$

Using an AKTA–FPLC, a Superdex75® 10/300 GL column was rinsed with filtered MilliQ-pure water for 2 (cv) at a flow rate of 0.5 mL/min and then equilibrated with 2 cv of 50 mM Tris, 150 mM NaCl, 1 mM EDTA pH 9.5. A concentrated $MinE_{Ng}$ sample produced by nickel affinity chromatography was centrifuged at 10,000x*g* for 10 min and injected into the column at a flow rate of 0.5mL/min. $MinE_{Ng}$ elution was monitored by UV absorbance at 280 nm, with fractions containing $MinE_{Ng}$ typically eluting at approximately 11.6 mL. If used as an additional purification step then fractions eluting at this approximate volume were collected and concentrated.

For the estimation of molecular weight by size-exclusion, protein standards were resuspended in 50 mM Tris pH 9.5, 150 mM NaCl, 1 mM EDTA buffer and analyzed in the same buffer at a flow rate of 0.5 mL/min. The void volume of the Superdex75® 10/300GL colum was determined to be from the mobility of Blue Dextran approximately to be 8.0 mL.

3.11 NMR Spectroscopy

All samples prepared for NMR spectroscopy were exchanged by dialysis into 50 mM Tris, 50 mM NaCl, 100 μM EDTA, 0.02% sodium azide, 0.2 mM PMSF and 10% D_2O and concentrated to approximately 0.9 mM – 1.5 mM at pH 9.5 or 100 μM at pH 7.8. All spectra were recorded at 25°C on a Varian Inova500, processed by NMRPipe (*78*) and analyzed with NMRView (*79, 80*). $MinE_{Ng}$ concentrations were typically ~0.9 – 1.5 mM for spectra recorded at pH 9.5 and 100 μM for the wild type spectrum recorded at pH 7.8. All HSQC spectra shown, including that of L22D, were reproduced at least once with proteins produced from independent purifications and found to yield superimposable spectra.

Backbone ^{15}N, $^{1}H^{N}$, $^{13}C_{\alpha}$, $^{13}C_{\beta}$ and ^{13}CO chemical shift assignments were made on the wild-type $MinE_{Ng}$ at pH 9.5 based on HNCA, HN(CO)CA, HNCACB, CBCA(CO)NH and HNCO experiments and amide proton assignments confirmed with an ^{15}N-edited NOESY utilizing a 100 ms mixing time (See Table 3.1 for spectral parameters). All 3D spectra except the HNCO, HNCA and HN(CO)CA were recorded at the Quebec/Eastern Canada High Field NMR Facility on the cryo-probe equipped INOVA 500. ^{1}H, ^{13}C and ^{15}N chemical shifts were referenced using a 2,2-dimethyl-2-silapentane-5-sulfonate (DSS) internal standard and secondary shifts from peptide-derived random coil values were calculated using NMRview.

Table 3.1: Spectral Data Set

	^{1}H		^{15}N		^{13}C		
Experiment	Spectral Width (sw, Hz)	Complex Points (ni)	Spectral Width (sw1, Hz)	Complex Points (ni2)	Spectral Width (sw2, Hz)	Complex Points (ni3)	Transients (nt)
15N HSQC	7017.5	449	1520.7	128	-	-	16
HNCO	7017.5	449	1115.1	30	1257.9	32	16
HNCA	7017.5	449	2030.4	28	3773.7	48	30
HN(CO)CA	7017.5	449	1115.1	27	3773.7	48	41
CBCA(CO)NH	7017.5	449	1115.1	31	6288.7	37	64
HNCACB	8384.9	512	1215.4	30	6383.0	31	64
15N-edited NOESY	7017.5	449	1115.1	27	7017.5*	110*	24

* *F2 is for ^{1}H in this experiment*

3.12 Circular Dichroism Spectroscopy

All samples for CD spectroscopy were further purified by size-exclusion chromatography (Section 3.11) and dialyzed into 10 mM Tris buffer at either pH 7.4 or 9.5. CD spectra were recorded on a Jasco J-810 circular dichroism spectropolarimeter with a 1 mm path length quartz cell at 25°C. Spectral scans were recorded from 250 – 190 nm with a 0.2 nm step resolution, a speed of 20 nm/min and a bandwidth of 1.0 nm. CD spectra were found to be reproducible for all samples over a concentration range of 10 – 100 μM under both pH conditions. Background subtraction was applied to the spectra by obtaining a blank spectrum of the buffer. No smoothing function was used. The mean residue ellipticity (MRE) was calculated as outlined in Chapter 2 using protein concentrations determined using a modified version of the Bradford assay and confirmed with the BCA assay (Section 3.13). The structural integrity of the sample was confirmed by SDS-PAGE analysis (Section 3.14). In order to estimate the secondary structure content from these spectra, spectral deconvolution was performed with CDPro (*61*).

3.13 Protein Concentration Determination

Protein concentrations were determined using commercially available Bradford (BioRad) (*81, 82*) and/or bicinchoninic acid (BCA) assays (Pierce Biotech.) (*83, 84*). For both assays, serial dilutions of a stock solution of bovine serum albumin (BSA) were used to generate a standard curve. In the Bradford assay, 200 μL of concentrated dye reagent (BioRad), containing dye, phosphoric acid and methanol, was added into 1 mL of protein solution and allowed to incubate at room temperature for at least 5 min but for no more

than 1 hr. The absorbance of the protein standards and samples were measured at 595 nm and linear regression was used within Excel to determine the equation of the best-fit line to the experimental data. The equation of this standard curve used to determine the concentration of $MinE_{Ng}$ samples.

For the BCA Protein Assay the procedures were followed according to the protocols specified by the manufacturer. Briefly, BCA working reagent was prepared by mixing 50 parts of BCA™ Reagent A, which contains 200 mM sodium carbonate, 120 mM sodium bicarbonate, 30 mM bicinchoninic acid and 10 mM sodium tartrate in 0.1 M sodium hydroxide (Pierce Biotech), with 1 part of BCA™ Reagent B, which contains 4% cupric sulfate (Pierce Biotech). 2.0 mL of working reagent was transferred into a clean test tube and 100 µL of each protein solution was added into each tube. Each tube was vortexed and incubated at 37°C for 30 min (or at room temperature for 2 hrs). After incubation, all samples were cooled to room temperature and the absorbances were measured at 562 nm.

3.14 Sodium Dodecyl Sulphate – PolyAcrylamide Gel Eletrophoresis (SDS – PAGE)

To assess the purity and yield of proteins, samples were analyzed by SDS-PAGE using the protocol described by Sambrook et al., 1980. Prior to loading, samples were diluted with 2X SDS-PAGE loading buffer (100mM Tris pH 6.8, 20% (v/v) glycerol, 4% (w/v) SDS, 0.02% bromphenol blue), and boiled for 5 minutes followed by centrifugation at 10,000*g* for 5 minutes. Polyacrylamide gels containing two phases – a 5% stacking phase, and a 12 or 15% resolving phase – were loaded with 20 µl of each sample and allowed to run at 200 volts for 30 minutes in 25 mM Tris base, 250 mM glycine, and 0.5%

SDS running buffer using the Mini-PROTEAN II Electrophoresis Cell (Bio-Rad). For visualization, gels were stained in Coomassie blue stain (50% methanol, 40% H_2O, 10% acetic acid, 0.1% (w/v) coomasie brilliant blue) for 60 min and destained in a solution containing 50% H_2O, 40% methanol, and 10% acetic acid.

CHAPTER 4

RESULTS

In order to pursue solution NMR studies on a full-length bacterial MinE protein we chose to focus on the homologue from *N. gonorrhoeae* (Ng) which has 42% sequence identity to the *E. coli* (Ec) protein. Previous studies with $MinE_{Ng}$ have indicated some potential differences from the Ec protein since both the C-terminal and N-terminal domains appear to be important for MinD binding (*49*). We therefore chose to study the Ng homologue to allow comparison with the existing structural data on the $MinE_{Ec}$ and help evaluate whether these variations between Ec and Ng proteins could be the result of structural differences. For this purpose, we used a C-terminally hexahistidine tagged $MinE_{Ng}$ construct that could be expressed and purified in high yield from *E. coli* in ^{15}N- and ^{15}N, ^{13}C-isotopically labeled forms. Functional assays with this His-tagged $MinE_{Ng}$ construct confirm that it retains the ability to promote a >10-fold increase in $MinD_{Ng}$ ATPase activity similar to observations made with the Ec proteins (data not shown). Since the C-terminus of $MinE_{Ec}$ and $MinE_{Ng}$ does not appear to be critical to MinE structure or function the His-tag was not removed for these studies.

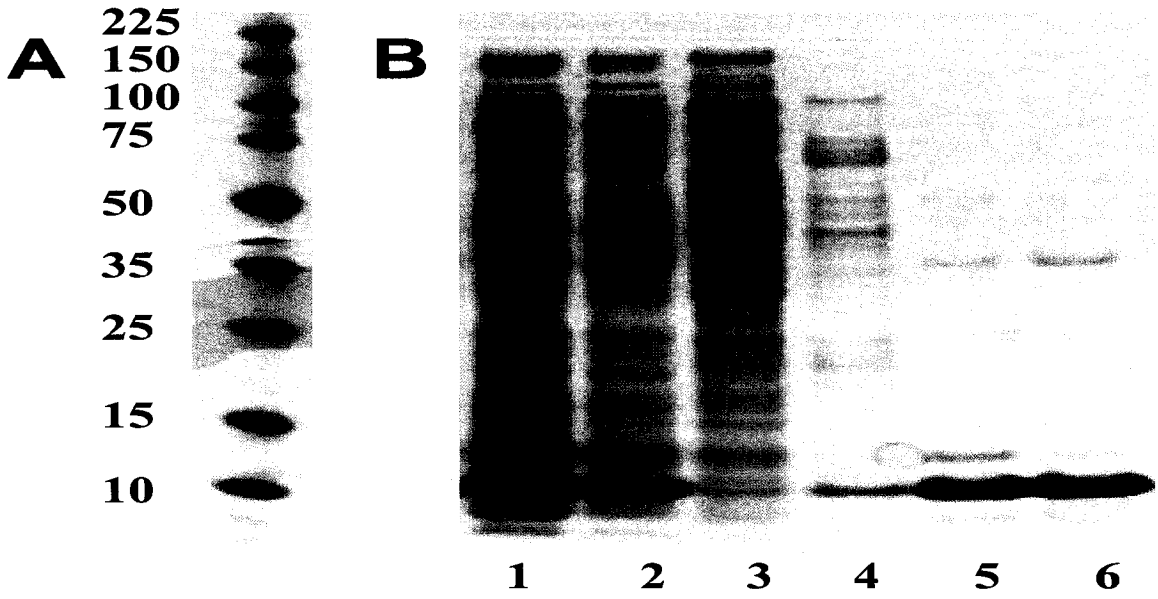

Figure 4.1: *$MinE_{Ng}$ Purification on a Ni-NTA column - **A)** Protein molecular weight standards (size indicated in kDa). **B)** Coomassie-stained 4-20% Nu-PAGE® SDS-PAGE gel of $MinE_{Ng}$ purification showing fractions from lLanes 1 – 2) water-soluble cell extract (after sonication); (3) 30 mL 10mM imidazole wash; (4) 30 mL 75mM imidazole wash; (5) 30 mL 250mM imidazole elution; and (6) 20 mL 500mM imidazole elution.*

4.1 Purification of $MinE_{Ng}$ and Estimation of its Complex Molecular Mass

In order to purify MinE, we used immobilized metal-ion affinity chromatography (IMAC), a separation principle that utilizes the differential affinity of proteins for metal ions. This differential affinity arises from the coordination bonds formed between metal ions and certain amino acid side chains, such as histidine, exposed on the surface of the protein molecules. In this approach, a metal (typically Ni(II)) is bound to a solid matrix through a chelator such as nitriloacetic acid (NTA). Since a hexahistidine tag was engineered into the C-terminal end of $MinE_{Ng}$, this protein should exhibit a high affinity for binding to the Ni-NTA resin. The results of this purification performed with a bench-top column are shown in Figure 4.1. As shown in lanes 1 and 2 of this Coomassie-stained

SDS-PAGE gel of the water-soluble fraction of bacterial cell extract, an intense band appears at an approximate MW of 10 kDa, corresponding to $MinE_{Ng}$. This impure extract was then applied to the Ni-NTA column, which was then washed with low concentrations of imidazole to remove non-specifically bound proteins (lanes 3 and 4). $MinE_{Ng}$ was then eluted with high concentrations of imidazole (lanes 5 and 6) with a purity usually exceeding 90%. A yield of 15 mg of $MinE_{Ng}$ was typically obtained from 1 L of bacterial culture.

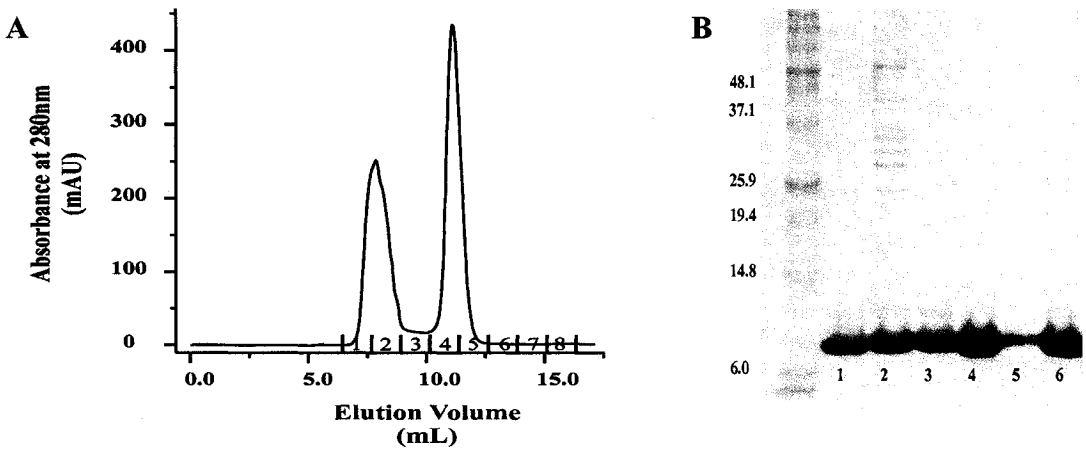

Figure 4.2: *Purification of $MinE_{Ng}$ by Size-Exclusion Chromatography – **A)** Absorbance at 280 nm monitored as a function of elution volume after Ni-NTA purified MinE was applied to a Superdex75® 10/300GL column. The sample was run at 0.5 mL/min flow rate in 50 mM Tris pH 9.5, 150 mM NaCl, 1mM EDTA. Number of fractions collected are indicated on the x-axis. **B)** The fractions from **A** on a 15% Coomassie-stained Tris-glycine SDS-PAGE. Lanes 1 to 5 correspond to the fractions indicated on the chromatogram in **A**, Lane 6 corresponds to the pure $MinE_{Ng}$ sample and after dialysis into 50 mM Tris, 50 mM NaCl, 1 mM EDTA pH 9.5.*

When a higher degree of MinE purity was required, gel filtration/size-exclusion chromatography was used to remove contaminants that differed in size relative to MinE. The purification chromatogram and accompanying gel in Figure 4.2A shows elution of

$MinE_{Ng}$ in two major peaks in at approximately 8.0 mL and 11.6 mL. While $MinE_{Ng}$ was present in both peak fractions, the first major peak also contained a number of high molecular weight contaminants. It is interesting to note that the 8 mL fractions corresponds to the column void volume where species larger than ~75 kDa would be expected to elute, suggesting that some of the $MinE_{Ng}$ existed as a water-soluble aggregate. However, this may have formed during purification due to the extremely high $MinE_{Ng}$ concentrations that were achieved on the His column. These aggregates were not observed once the low molecular weight $MinE_{Ng}$ peak (11.6 mL) had been isolated by gel filtration chromatography as long as the sample pH was maintained at 9.5. Isolation of $MinE_{Ng}$ from the 11.6 mL peak fraction made it possible to acquire >95% pure sample as shown in lane 6 of Figure 4.2B.

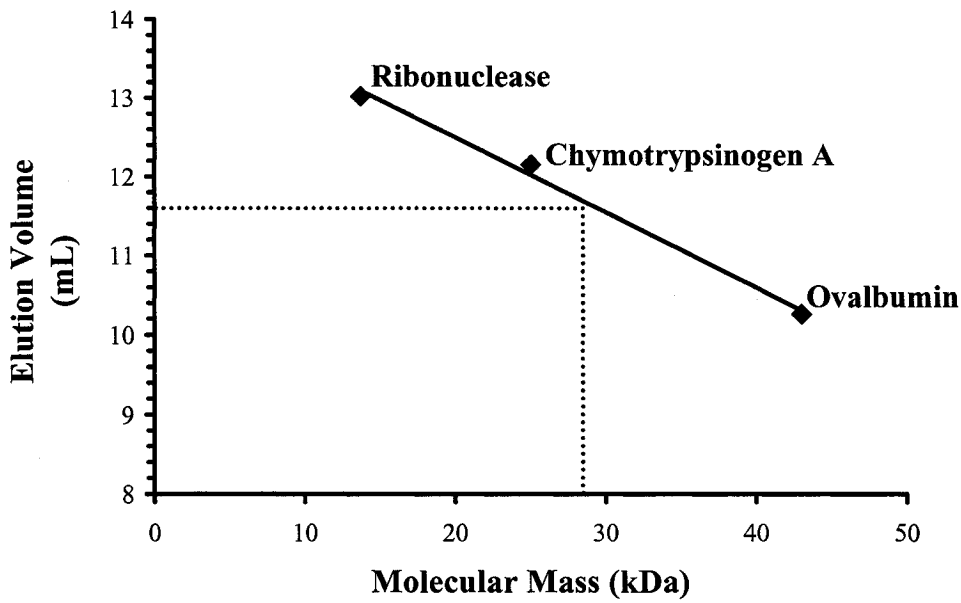

Figure 4.3: *Molecular Weight Calibration of the Superdex75® 10/300GL column. Each molecular weight standard was run under conditions that were identical to these those used for $MinE_{Ng}$ (described in Figure 4.2 legend). A least-squares fit was applied to find the approximate linear relationship between molecular mass and elution volume.*

To estimate the molecular weight of $MinE_{Ng}$ from its elution profile in the gel filtration purification, a series of molecular weight standards were applied to the same column and their elution volumes measured. As shown in Figure 4.3, a plot of the elution volumes of these standards versus their known molecular mass generates a roughly linear relationship that can be used to estimate the molecular weight of unknown samples. From this relationship, the 11.6 mL fraction corresponds to a molecular weight of approximately 28 kDa, a result that was also found at pH 7.8 (data not shown). Since $MinE_{Ng}$ is known to exist predominantly as a dimer at physiological pH, it is likely that this peak corresponds to the dimeric form and not a trimer as suggested by the estimated molecular weight. Although sample mobility through a gel filtration column depends on the molecular weight, differences in shape from a spherical form will lead to differences in mobility from that predicted by the calibration standards (*54*). While the structure of the full-length $MinE_{Ng}$ dimer is not yet known, it is likely that this complex does not have a perfectly spherical globular form and so the molecular mass of this complex is likely to be closer to the 20 kDa predicted from the dimer. This has since been confirmed in analytical ultracentrifugation studies performed at the Protein Function Discovery Facility at Queen's University (T. Ducat, personal communication). Therefore, even at pH 9.5, it appears that $MinE_{Ng}$ retains it dimeric form with no detectable monomer present.

4.2 Optimization of Sample Buffer Conditions for NMR Analyses

Since structure determination of proteins by solution NMR requires samples with a concentration that is optimally >0.5 mM, a number of different sample conditions were tested for $MinE_{Ng}$ with our first experiments investigating the pH dependence of $MinE_{Ng}$

solubility. The theoretical isoelectric point (pI) of $MinE_{Ng}$ based on primary sequence analysis is 6.3 – 7.0 (with or without the hexahistidine tag), suggesting that the solubility of $MinE_{Ng}$ would be lowest in this pH range (*54*). Therefore, the solubility of $MinE_{Ng}$ was tested outside this range (i.e. pH 5.0, 7.2 and 9.5). Since the sample was originally prepared at pH 8.0 as required for Ni-NTA chromatography, $MinE_{Ng}$ was already above its pI. Therefore, to transfer the sample to pH conditions that are below the pI, precautions were taken to minimize the exposure time to buffers with pH 6 – 7. In addition, the concentration of these samples was lowered prior to buffer exchange as high concentrations also favour aggregation. For the pH 5.0 solubility trials, $MinE_{Ng}$ samples were always diluted to ~1 μM and the pH then changed by rapid addition of concentrated low pH acetate buffer. The pH 7.2 buffer was also diluted to ~1 μM prior to buffer exchange in order to minimize the chance of aggregation.

In the first series of tests, these three pH conditions were evaluated in the presence of 50 mM NaCl and 1 mM EDTA. The concentration of protein before and after dialysis was determined using a modified Bradford assay (*81*). After buffer exchange, the maximum MinE concentration was also determined by concentrating the sample until some precipitation was observed (i.e. the $MinE_{Ng}$ saturation point). The amount of $MinE_{Ng}$ remaining in solution was used as the estimate of maximum solubility. As shown in Table 4.1 (Trial # 1 – 3), the results of this study show that the solubility of $MinE_{Ng}$ was highest at pH 9.5, with a maximum concentration of approximately 1 mM. As the sample pH decreased, the stability of $MinE_{Ng}$ decreased dramatically. Therefore based on these observations, it is clear that MinE solubility is optimal at high pH.

Table 4.1: Assessment of Protein Solubility

Trial #	*Buffers**	*pH*	*Additive*[X]	*Maximum Solubility*[+] *(mM)*
1	*Acetate*	5.0	-	0.03 ± 0.01
2	*Tris*	7.2	-	0.14 ± 0.01
3	*Tris*	9.5	-	1.05 ± 0.01
4	*Acetate*	5.0	50 mM $(NH_4)_2SO_4$	0.10 ± 0.03
5	*Acetate*	5.0	100 mM $(NH_4)_2SO_4$	0.15 ± 0.03
6	*Tris*	7.2	50 mM $(NH_4)_2SO_4$	0.13 ± 0.03
7	*Tris*	7.2	100 mM $(NH_4)_2SO_4$	0.11 ± 0.03
8	*Acetate*	5.0	50mM Arginine	0.02 ± 0.01
9	*Acetate*	5.0	150mM Arginine	0.02 ± 0.01
10	*Tris*	7.2	50mM Arginine	0.05 ± 0.01
11	*Tris*	7.2	150mM Arginine	0.07 ± 0.01

* 50 mM of the indicated buffer, 50 mM NaCl, 1 mM EDTA

[X] The 50 mM NaCl was replaced with the additive shown.

[+] The maximum concentration of $MinE_{Ng}$ after exchange into the indicated solution and concentration to saturation.

Athough the best pH for MinE solubility was significantly greater than pH 7.0, the optimal pH for solution NMR of proteins is between pH 5 and pH 7 (*66*). Utilization of lower pH conditions minimizes the rate of amide protein exchange with solvent protons that reduces the intensity of peaks in amide proton-detected experiments. Therefore, $MinE_{Ng}$ solubility was tested in the presence of other additives that could help prevent protein aggregation at low pH. Ammonium sulphate was tested first, since it is a known kosmotrope, which in some cases can increase protein solubility (*85*). As shown in Table 4.1, the addition of ammonium sulphate to acetate buffer led to an increase solubility of $MinE_{Ng}$ (Trial # 4 – 6). However, even at a 100 mM concentration of ammonium sulphate, the $MinE_{Ng}$ concentration only increased to ~150 μM, which is still too low for structural studies on a 500 MHz spectrometer without a cryoprobe. In addition, $MinE_{Ng}$ solubility in Tris pH 7.2 buffers did not improve at all with this additive (Trials 2, 6 and 7). Therefore, ammonium sulphate was not able to improve MinE solubility to the degree required for structure determination.

It has been shown that inclusion of positively charged amino acids such as arginine can favour the folded state (*85, 86*). Thus, arginine was tested for its ability to improve $MinE_{Ng}$ solubility. As shown in Table 4.1, the solubility of $MinE_{Ng}$ actually decreased in the presence of arginine in both acetate and Tris buffers (Trial # 8 -11), indicating that this additive is not appropriate for $MinE_{Ng}$. Overall, the result of these buffer optimization studies suggested that it may not be possible to obtain high concentrations of $MinE_{Ng}$ in pH conditions that would be optimal for solution NMR studies. However, given the high solubility of $MinE_{Ng}$ at high pH, we decided to determine whether some structural information could be obtained under these conditions.

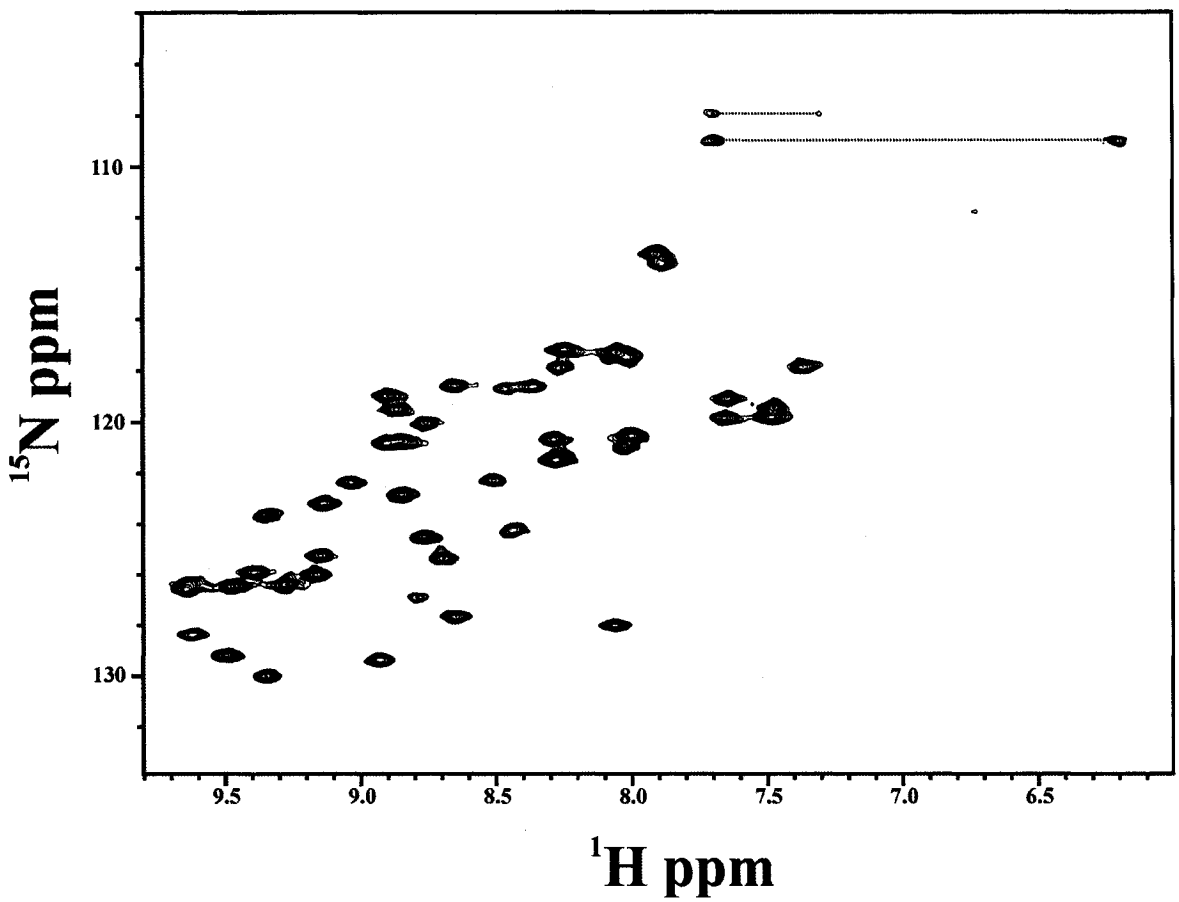

Figure 4.4: *$^{1}H - ^{15}N$ HSQC at High pH. The 1.5 mM WT $MinE_{Ng}$ sample was analyzed in 50 mM Tris, 50 mM NaCl, 100 μM EDTA, 0.02% sodium azide, 0.2 mM PMSF at pH 9.5 at 25°C on a Varian INOVA500. Peaks arising from sidechain amides are connected by a dotted line.*

4.3 NMR Analyses of Wild-Type $MinE_{Ng}$ at High pH

A stably folded protein will possess hydrogen-bonded and/or buried backbone amide protons that should be protected from solvent exchange and hence, it can be possible to observe signals from exchange-protected amide protons in a $^{1}H - ^{15}N$ HSQC spectrum at high pH. Therefore, to determine whether $MinE_{Ng}$ was folded under conditions where it was soluble, we recorded an HSQC spectrum of a 1.5 mM ^{15}N-labeled sample at pH 9.5.

As shown by the spectrum in Figure 4.4, 48 of the expected 89 backbone amide peaks are observed, suggesting that approximately half of the amide protons are protected from rapid solvent exchange. In addition, the wide range of proton chemical shifts suggests that the regions resistant to solvent exchange comprise part of a folded domain, as would be expected from the solvent protection.

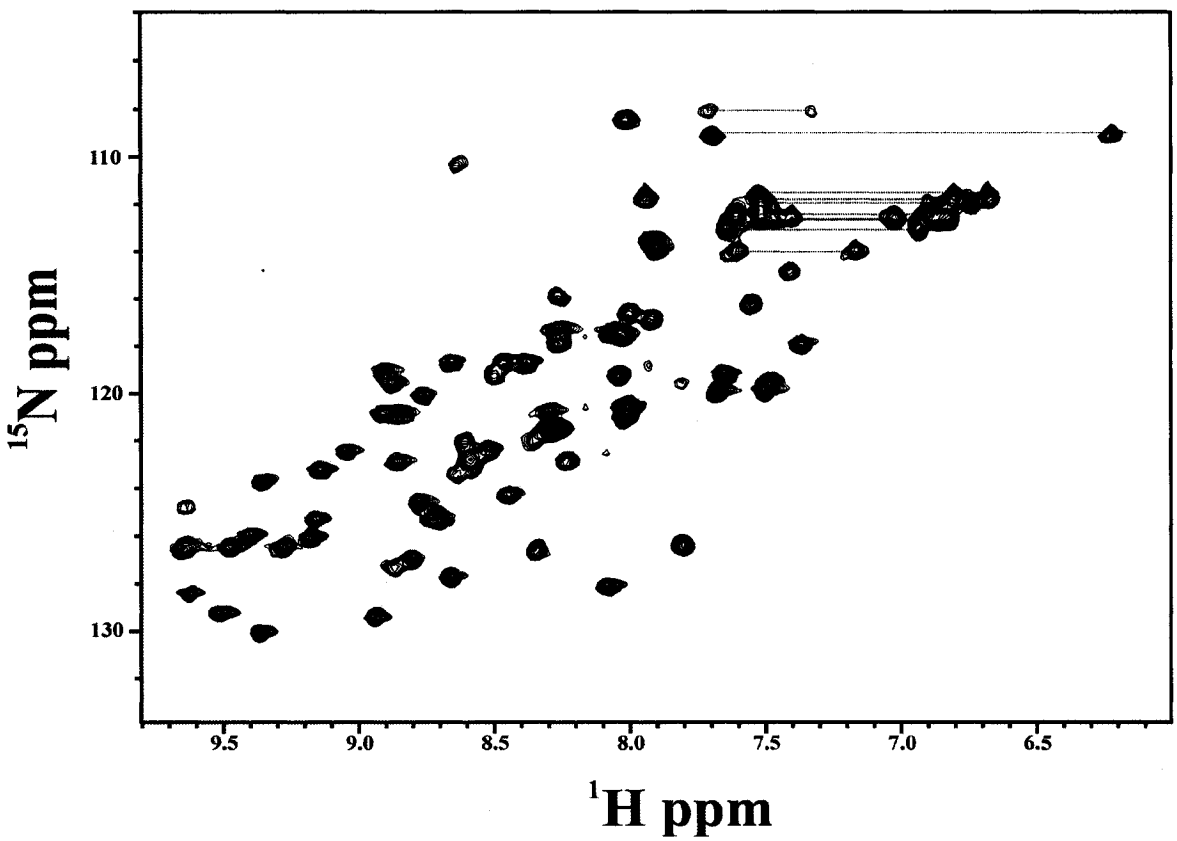

Figure 4.5: *Effect of pH on $^{1}H - ^{15}N$ HSQC of $MinE_{Ng}$. The spectrum of $MinE_{Ng}$ at pH 9.5 (red) was superimposed onto the spectrum at pH 7.8 (black). Aside from pH, buffer conditions were identical to those in the Figure 4.4 legend.*

To establish that the structure of $MinE_{Ng}$ at high pH is similar to its structure at a physiological pH, a 100 μM ^{15}N-labeled sample of $MinE_{Ng}$ was also prepared at pH 7.8.

As shown in Figure 4.5, the HSQC spectrum of this sample shows the appearance of approximately 20 new backbone amide proton peaks that are distinct from those observed in the high pH spectrum that likely arise from parts of $MinE_{Ng}$ that are only partially protected from solvent exchange. In addition, a subset of peaks is obtained that overlap exactly with those in the high pH spectrum. Since chemical shift is a property that is exquisitely sensitive to small changes in the local chemical environment, the absence of pH-dependent chemical shift changes in these peaks suggests that the core of the structure of $MinE_{Ng}$ does not change with pH.

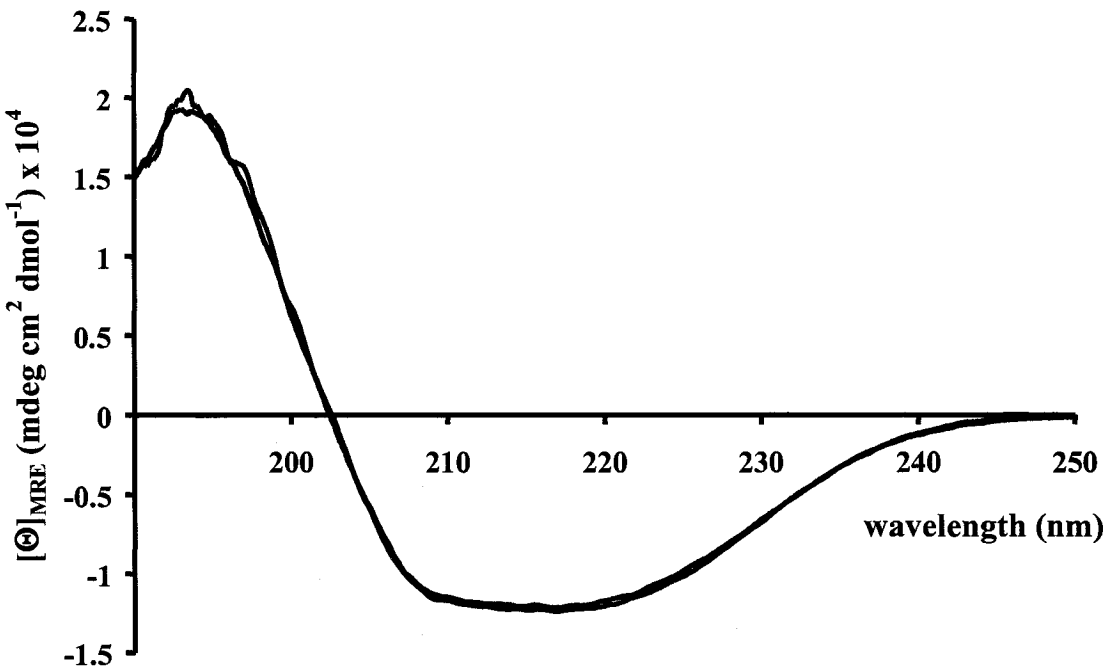

Figure 4.6: *Effect of pH on CD Spectra of $MinE_{Ng}$. Approximately 15 μM MinE in 10 mM Tris at pH 7.4 (blue) or pH 9.5 (red) was analyzed by CD as described in the Materials and Methods.*

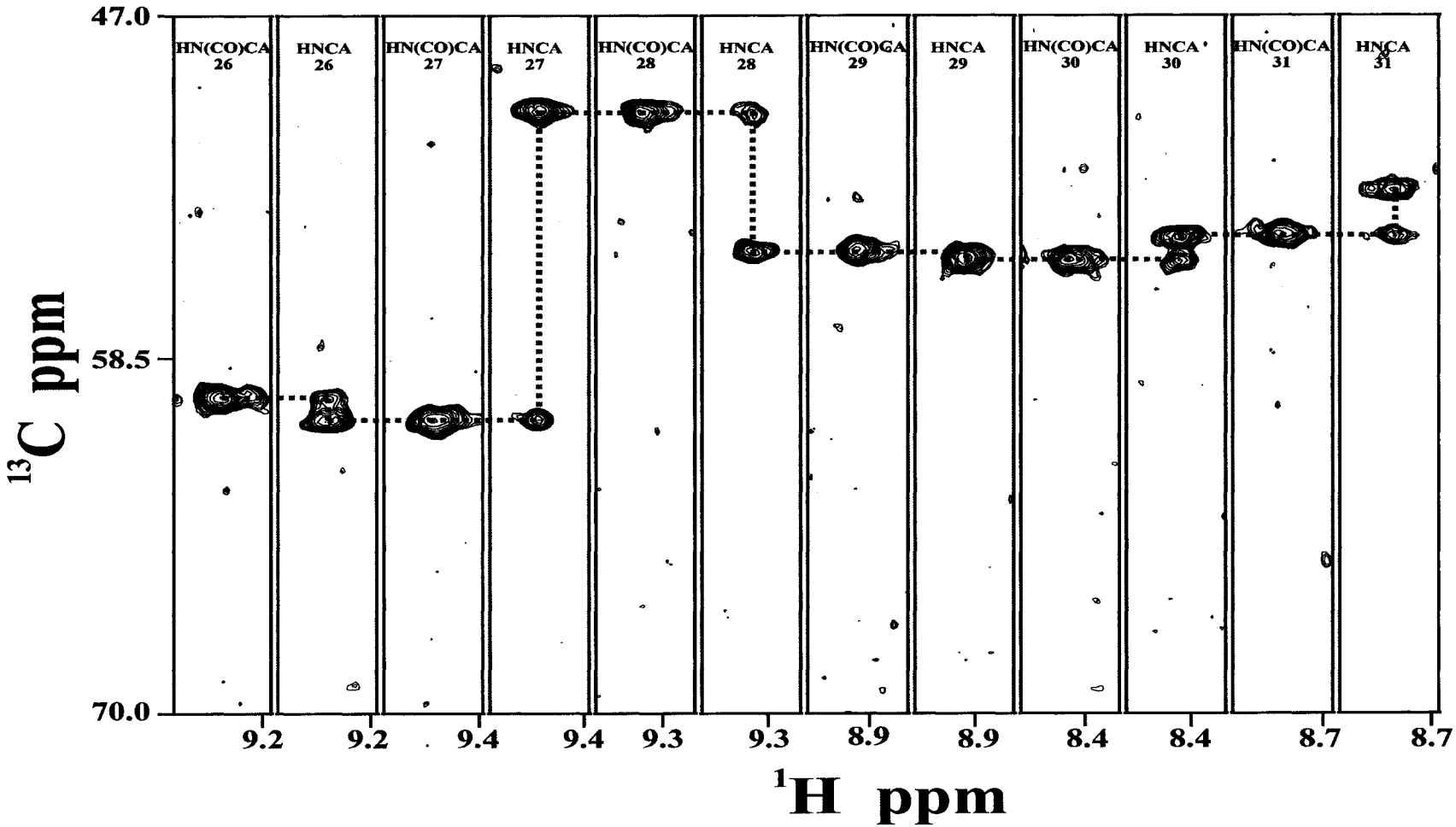

Figure 4.7: *$^{1}H - ^{13}C$ Strip Plots from HN(CO)CA and HNCA experiments for $MinE_{Ng}$ Residues 26 to 31 – Intra- and inter-residue correlations between strips confirm the connectivity of this series shown with the blue line.*

The absence of structural differences in $MinE_{Ng}$ between low and high pH conditions was further substantiated by circular dichroism (CD) spectroscopy, which showed superimposable spectra for $MinE_{Ng}$ in the two pH conditions as shown in Figure 4.6. Since this technique provides a measure of the total secondary structure of a protein sample, these spectra provide additional evidence that $MinE_{Ng}$ has a folded domain that persists under high pH conditions.

4.4 Backbone Chemical Shift Assignment of $MinE_{Ng}$

Since the MinE sample appeared to be folded under high pH conditions, we decided to pursue backbone chemical shift assignment of the parts of $MinE_{Ng}$ that were visible in the spectrum. In order to achieve this, we decided to start with the HNCA and HN(CO)CA experiments since these are the most sensitive experiments that can be used for backbone chemical shift assignment. The HNCA correlates the amide ^{1}H and ^{15}N chemical shifts with both the intra-and inter residue $^{13}C_{\alpha}$ shift (*62, 64*). In order to distinguish between intra- and inter-residue correlations, the HN(CO)CA experiment was also run since only the inter-residue correlation is observed in this experiment (*62, 64*). In spite of the high concentration of this sample, sensitivity in this experiment was poor, likely due to solvent exchange that may still occur in these protected regions. Nonetheless, most of the inter- and the intra-residue correlations were observed. Chemical shift assignment was attempted by arranging strips such that the inter-residue $^{13}C_{\alpha}$ chemical shift from each strip matched the intra-residue $^{13}C_{\alpha}$ shift of the previous residue. A successful example of this is shown

in Figure 4.7, for strips from the HNCA and HN(CO)CA spectra that could assigned to residues Ile26 to Ala31.

One of the major drawbacks to using only HNCA and HN(CO)CA spectra to assign chemical shifts is that the dispersion of $^{13}C_{\alpha}$ shifts is poor and hence, there is a good chance that $^{13}C_{\alpha}$ shifts from more than one residue will be indistinguishable. This gives rise to ambiguities in chemical shift assignment that cannot be resolved by these spectra alone. Instead, additional three-dimensional experiments must be used that can provide correlations beyond the $^{13}C_{\alpha}$. This can be provided by the HNCACB and CBCA(CO)NH experiments, both of which correlate the $^{13}C_{\alpha}$ and $^{13}C_{\beta}$ resonances of an amino acid residue with the amide proton and nitrogen resonances of the following residue. In addition, the HNCACB experiment also correlates the amide resonances with both $^{13}C_{\alpha}$ and $^{13}C_{\beta}$ resoncances of the same residues. Consequently, each $^{1}H - ^{13}C$ strip in the HNCACB contains four peaks; intense intra-residue $^{13}C_{\alpha}$ and $^{13}C_{\beta}$ peaks and weaker inter-residue $^{13}C_{\alpha}$ and $^{13}C_{\beta}$ peaks. In addition, the $^{13}C_{\alpha}$ and $^{13}C_{\beta}$ resonances can be distinguished from each other in this experiment since they are of opposite intensities. Therefore, as was done for the HNCA experiment, assignment can be achieved by matching inter-residue correlations to intra-residue correlations in a strip from the preceding residue. Since two carbon chemical shifts ($^{13}C_{\alpha}$ and $^{13}C_{\beta}$) must be matched in these strips, this reduces the potential ambiguities when determining the sequence of strips.

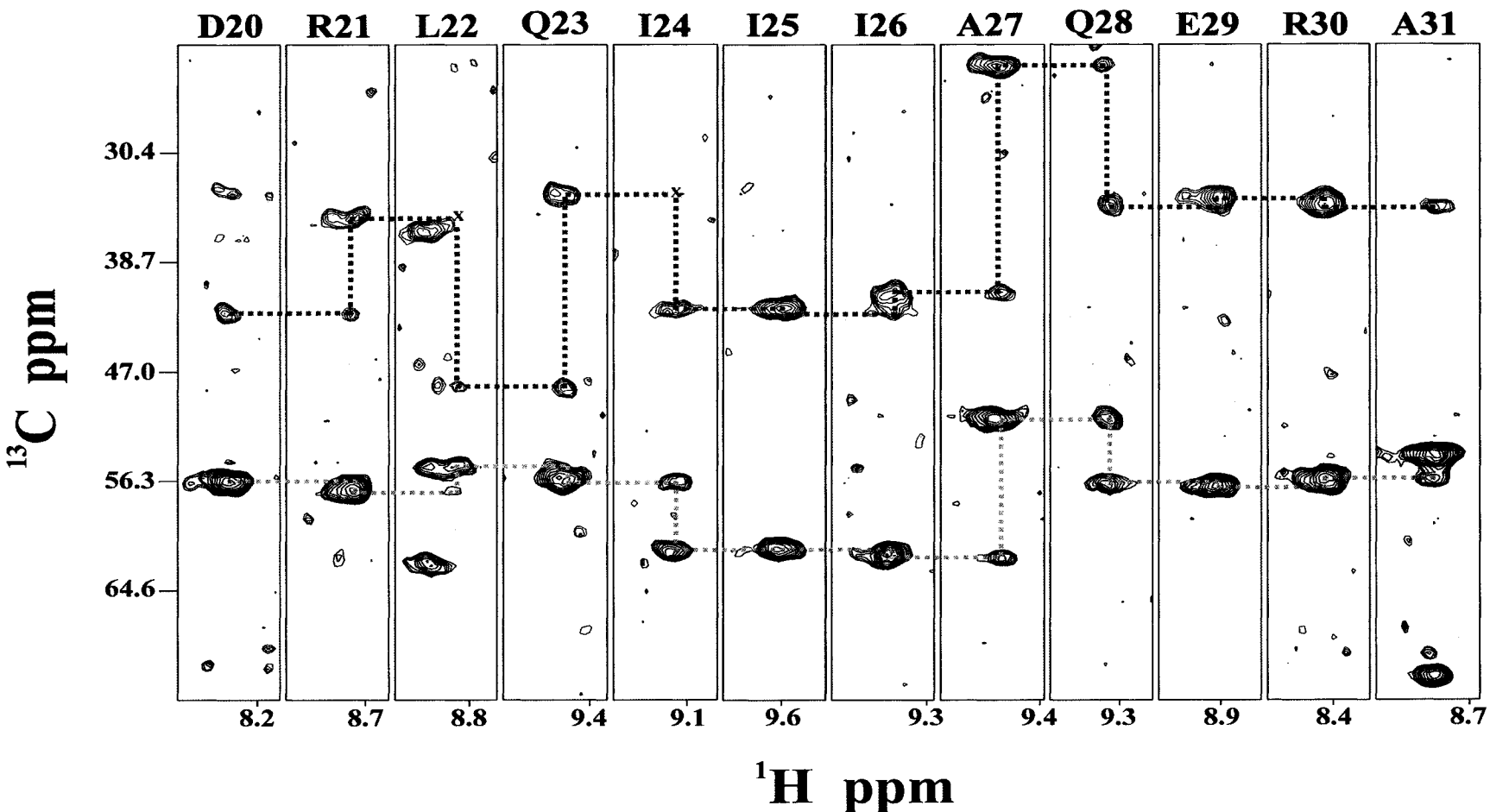

Figure 4.8: *Assigned HNCACB Strip Plot for the Anti-MinCD Domain of $MinE_{Ng}$ – The HNCACB ^{1}H – ^{13}C strips are shown for each amide proton in the Anti-MinCD segment over residues 20 – 31. Positive intensities are indicated by black contours and negative intensities by red contours. The blue dotted line outlines the sequential connectivities between the intra- and inter-residue $^{13}C_{\beta}$ correlations and the green dotted line shows $^{13}C_{\alpha}$ correlations. Peak positions of inter-residue correlations that were absent in the HNCACB, but observed in the CBCA(CO)NH spectrum (not shown) are marked in the strips with an X.*

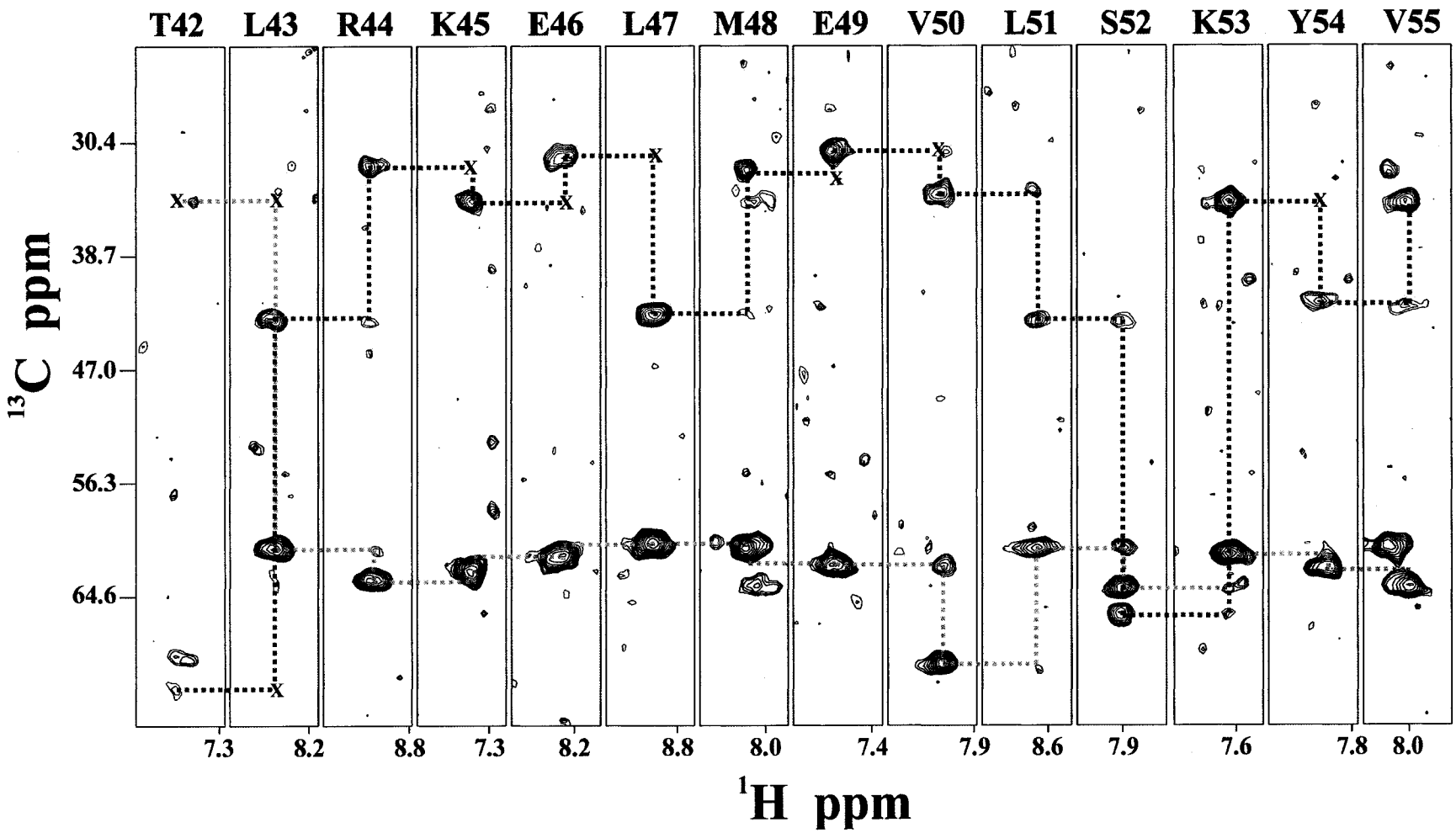

Figure 4.9: *HNCACB Strip Plots for Backbone Assignment of α-Helix B of* $MinE_{Ng}$.

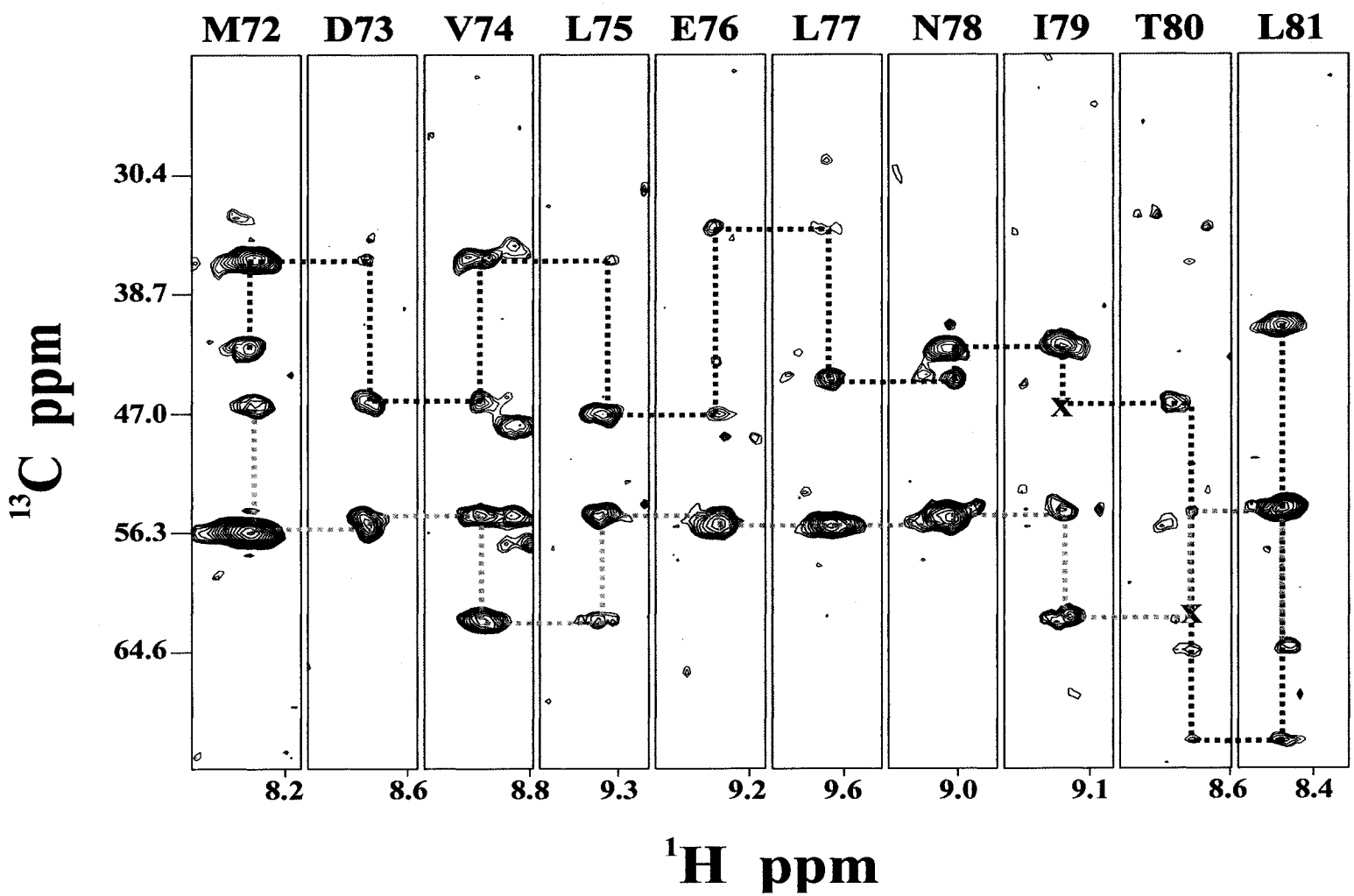

Figure 4.10: *HNCACB Strip Plots for Backbone Assignment of β-Sheet 2 of $MinE_{Ng}$.*

Since the sensitivity of these experiments is lower than the HNCA/HN(CO)CA (*62, 64*), it was necessary to record them on an NMR spectrometer equipped with a cryoprobe at the regional facility at McGill University in Montreal. This made it possible to observe a large number of the expected correlations in these experiments such that a more complete and reliable set of backbone assignments could be made. Some examples of resonance assignment from HNCACB data are shown in Figure 8 – 10, which show the HNCACB strips that were assigned to residues D20 to A31, T42 to V55 and M72 to L81. The high pH of the NMR sample used for these studies led to poor sensitivity for these experiments even with use of a cryoprobe-equipped spectrometer. Consequently, some inter-residue correlations were missing from the HNCACB experiment. Fortunately, in some cases, the missing peaks in the HNCACB spectrum were present in the CBCA(CO)NH making it possible to assign most of the backbone atoms for residues that appear in the HSQC.

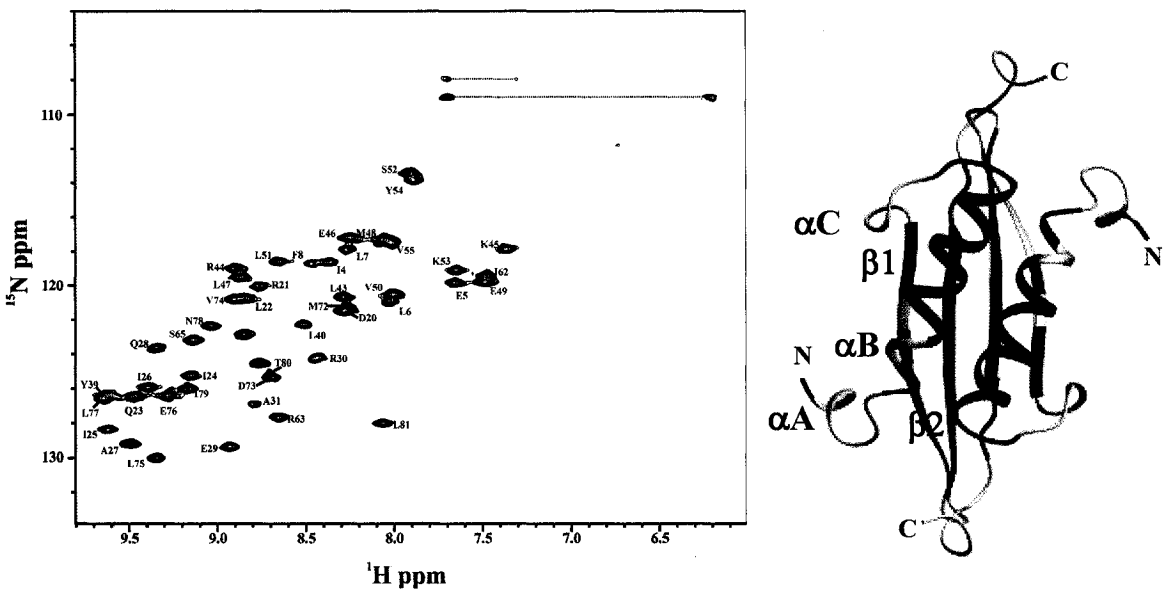

Figure 4.11: *Assigned ^{1}H – ^{15}N HSQC spectrum of WT MinE at pH 9.5. Residues assigned to the anti-MinCD domain are labeled in red. TSD residues are labeled in blue and have been mapped in green onto the ribbon diagram of the TSD structure previously determined for $MinE_{Ec}$ (45).*

As shown in Figure 4.11, it was possible to assign 46 of the 48 peaks from the HNCA, HN(CO)CA, HNCACB and CBCA(CO)NH spectra. Approximately 30 of the assigned residues could be mapped onto homologous regions in the NMR structure of the TSD from $MinE_{Ec}$. This analysis showed that the regions of $MinE_{Ng}$ that are protected from solvent exchange occur in the central α-helix (αB) and beta sheet (β2) that form the extensive dimeric interface between monomers. The high affinity for dimer formation reported for $MinE_{Ec}$ (~0.3 μM) is consistent with the persistent backbone hydrogen bonding characteristic of a stably folded dimer. The C-terminal half of the outer-most β-sheet (β1) was also protected from exchange, suggesting that hydrogen bonds between β-sheets in these regions are also relatively strong.

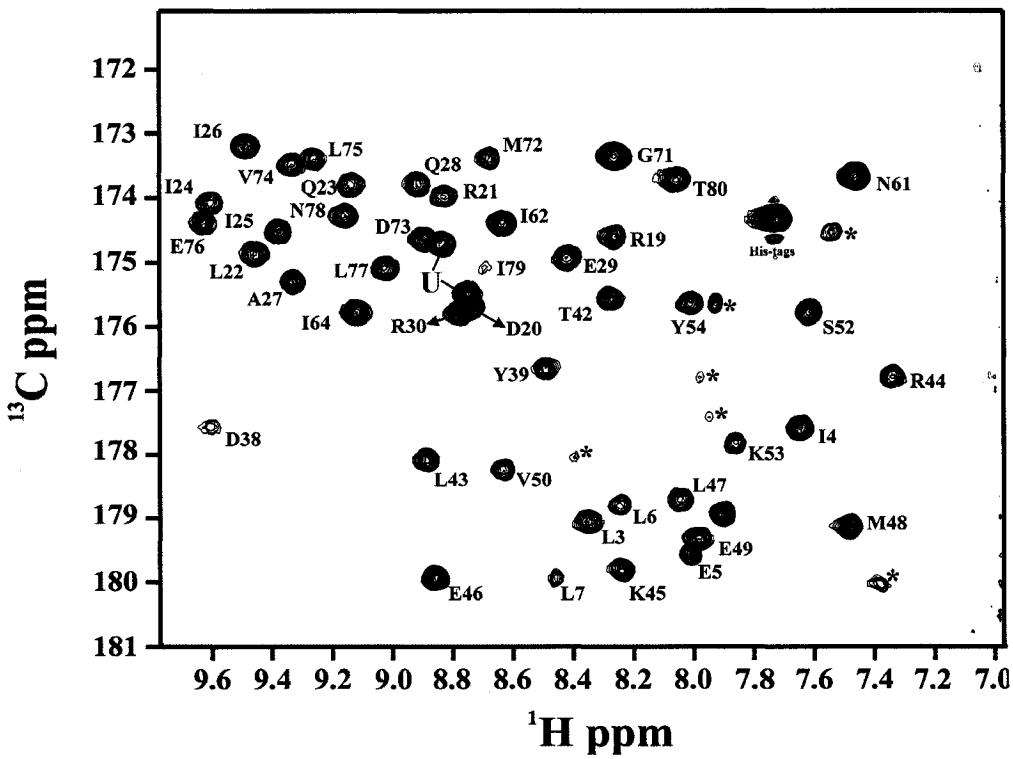

Figure 4.12: *Assigned HNCO spectrum of WT MinE at pH 9.5. Amide proton chemical shifts are correlated with the carbonyl chemical shifts from the preceding residue. The green asterisks denote peaks found from the HNCO spectrum that are not present in the HSQC spectrum potentially due to sidechain correlations. The purple U represents the two peaks that were unassigned.*

Once the amide proton and nitrogen atoms were assigned, an HNCO could be used to correlate these assignments to carbonyl chemical shifts in the preceding position. As shown in Figure 4.12, the ^{13}CO chemical shifts were assigned to 47 residues. These carbonyl shifts were useful for secondary structure analyses described in *Section 4.5*.

4.5 Secondary Structure Prediction Based Secondary Shifts from Random Coil Values

From assigned backbone chemical shift resonances it is possible to obtain a reliable prediction of secondary structure by calculating secondary shifts (defined as the difference between experimental and random-coil values) (*69*). This was done for assigned $MinE_{Ng}$ residues using C_α and CO atoms since these secondary shifts largely reflect local backbone conformations. In the analysis shown in Figure 4.13, positive secondary C_α and CO shifts indicative of helical conformations were observed for residues homologous to the αB helix determined in the Ec-TSD structure. Negative secondary C_α and CO shifts characteristic of beta structure arose in regions homologous to strands β1 and β2 in the Ec-TSD structure. Therefore, these results indicate that Ng-TSD adopts a similar fold to the Ec-TSD, as would be expected for the high degree of sequence similarity observed between the two proteins. In addition, this agreement between secondary shift predictions and the Ec-TSD structure provides additional confirmation for our chemical shift assignment.

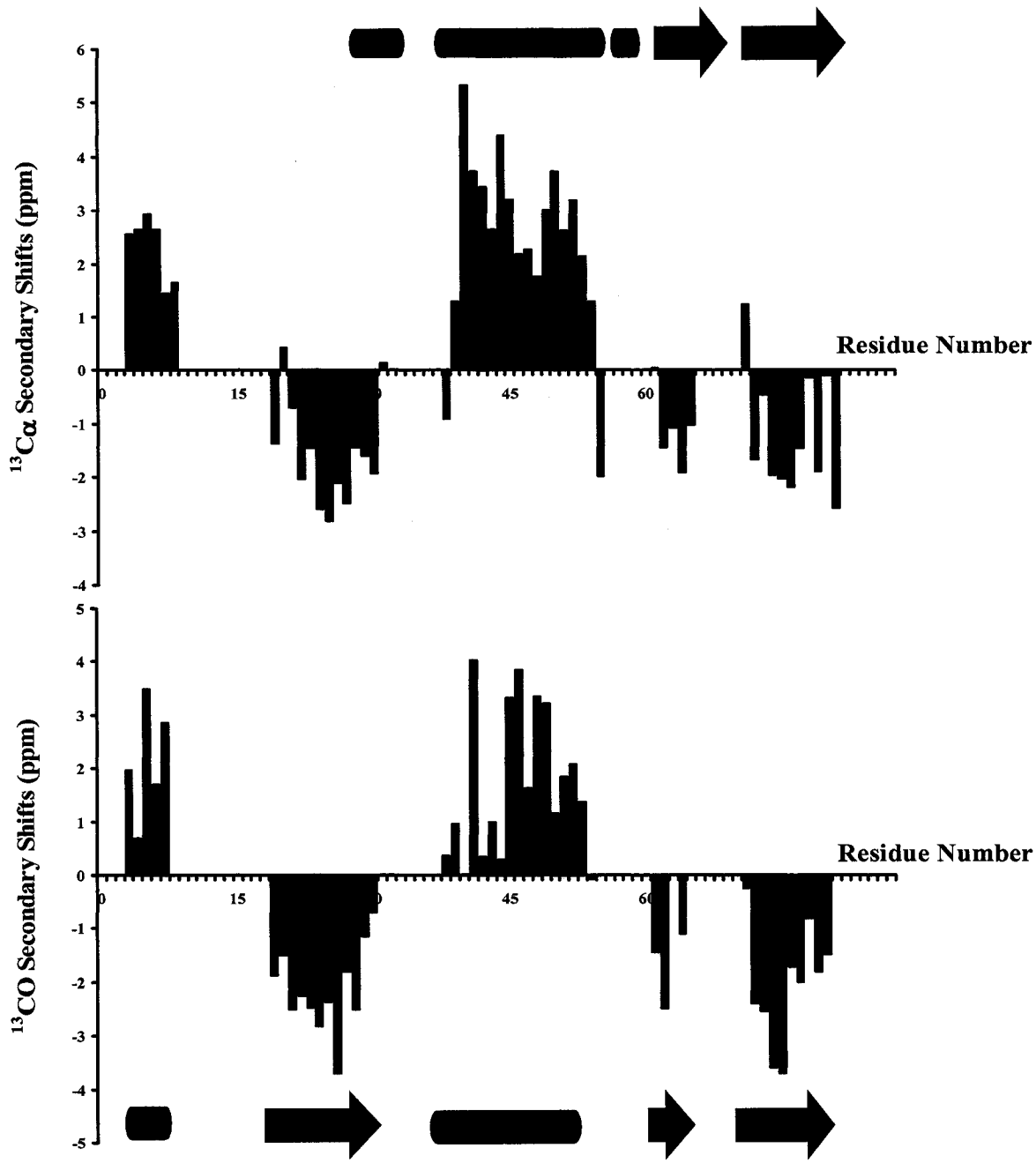

Figure 4.13: *Secondary structure of $MinE_{Ng}$ determined from C_α and CO chemical shifts. Shown are the differences between experimental C_α and CO chemical shifts and published random coil values for $MinE_{Ng}$ at pH 9.5. Regions showing positive secondary C_α and CO shifts indicate a helical conformation, while negative secondary shifts are characteristic of beta-structures. The predicted secondary structures are drawn schematically in red at the bottom and the secondary structure of the Ec-TSD in the previously determined NMR structure in green on the top. Residues not visible in the NMR spectrum at this pH were not assigned and have been given a secondary shift value of zero.*

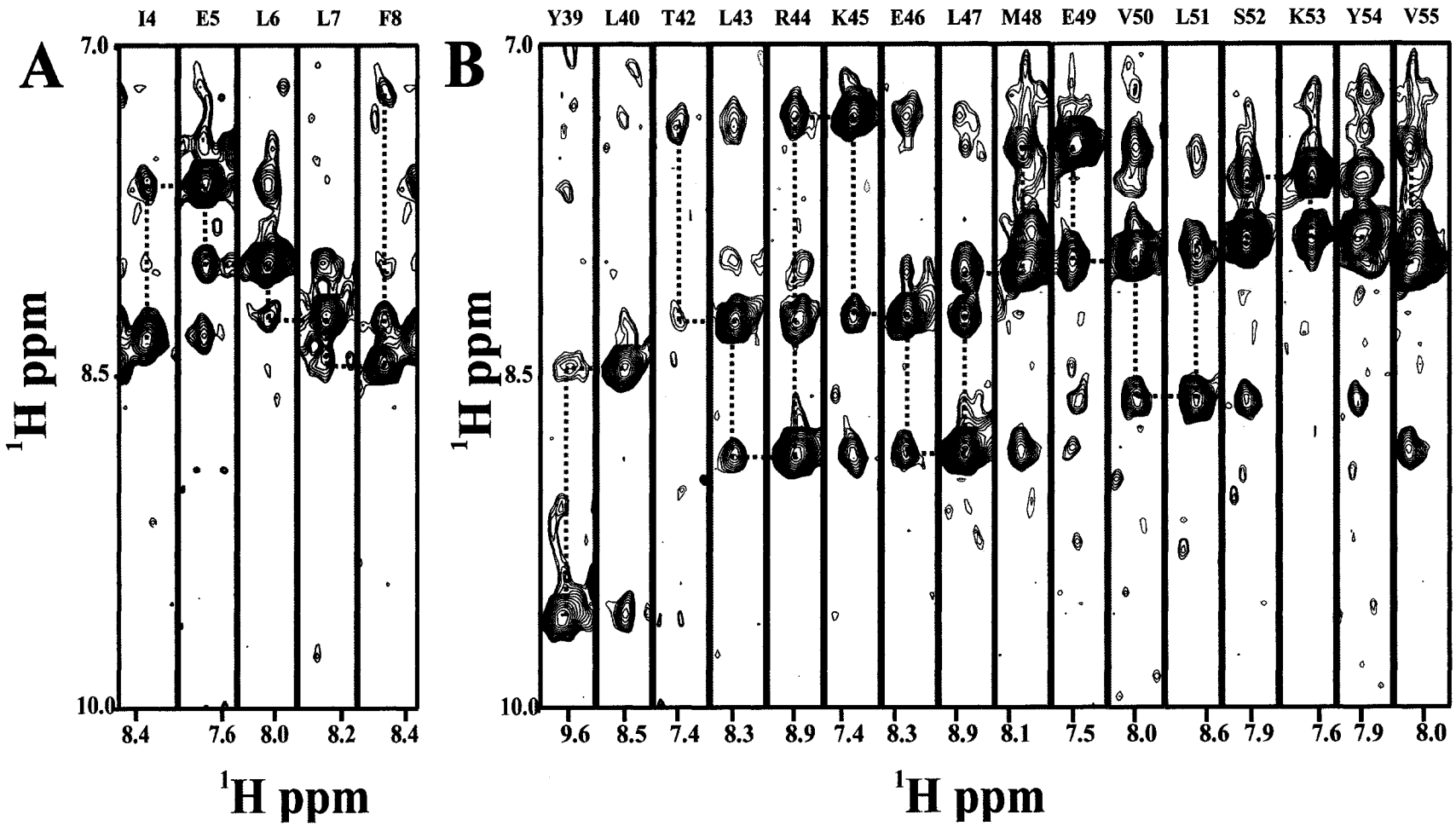

Figure 4.14: *^{1}H – ^{1}H Strips from the ^{15}N-Edited HSQC – NOESY for* ***A)*** *residues I4 – F8 and* ***B)*** *residues Y39 – V55. Note that there is no strip for residue 41 as this is a proline residue.*

The predicted secondary structure of the assigned N-terminal domain residues is of particular interest, since no structural information for the anti-MinCD domain in the full length protein was previously available. As shown in Figure 4.13, significant positive C_α and CO secondary shifts are observed for residues 3 – 8, which would suggest that this part of the N-terminal domain is helical. In addition to the N-terminal helix, anti-MinCD residues 21 – 30 show secondary shifts that predict for a β-sheet conformation. As no structural data has been previously collected from this region of MinE it is not possible to compare these results to the structure of the isolated domain. However, it is clear from the secondary structure and solvent protection results that this region of $MinE_{Ng}$, which contains a number of residues important for MinD interactions, has significant structure in the full-length protein.

4.6 Confirmation of Assignments and Structure for Helical Regions of MinE with the ^{15}N-edited NOESY

In an ^{15}N-edited NOESY, it is possible to identify atoms that are within 5 Å of a particular amide proton. For helical structures, this gives rise to a characteristic pattern of strong inter-residue NOEs between sequential residues. Therefore, to confirm the helical secondary structure assignment as well as the amide chemical shift assignments, an ^{15}N-edited NOESY was run with a short mixing time to minimize the impact of spin diffusion. As shown in Figure 4.14, the sequential connectivities between amide protons were confirmed by the presence of strong NOEs between adjacent residues for residues 4 – 8 and 39 – 55. Therefore, these regions are most likely in an α-helical structure. It should be

noted that the ^{15}N – NOESY strips from the β-regions of the protein did not show these strong inter-residue NOEs between amide protons (data not shown) which is consistent with the larger distance separating sequential amide protons in the β-structures. Although indirect, this data provides additional support for the β-sheet assignments made from the secondary chemical shift analysis.

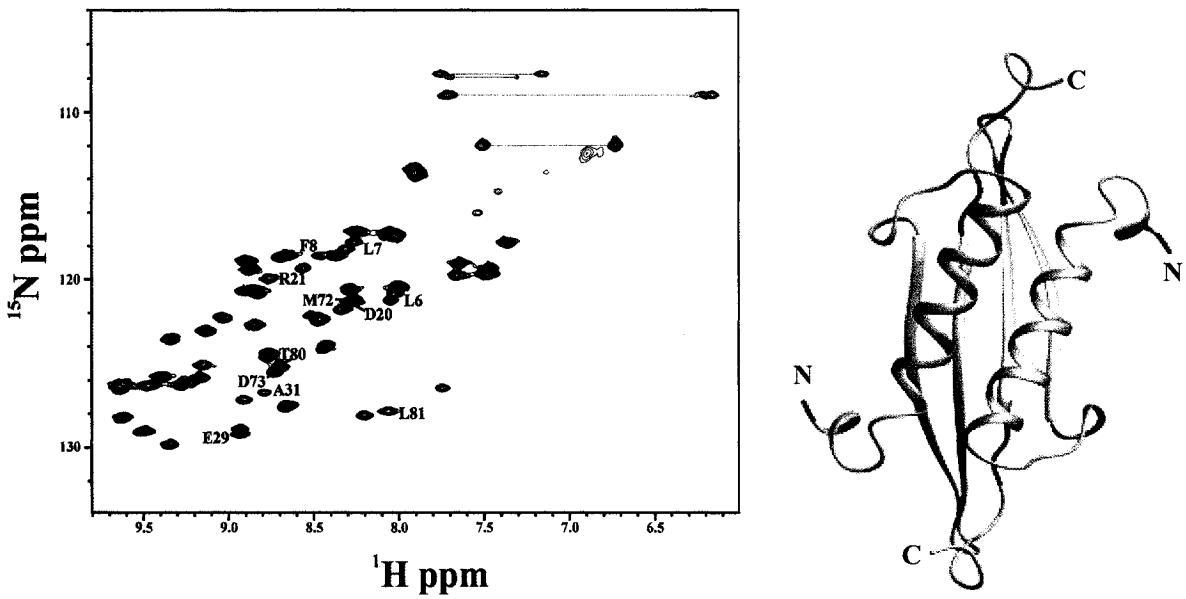

Figure 4.15: *^{1}H – ^{15}N HSQC spectrum of A18D (red) superimposed on the black spectrum of WT $MinE_{Ng}$. Both spectra were recorded at pH 9.5, 25°C. Residues that show chemical shift differences between WT and A18D spectra are labeled in the spectrum and also highlighted in neon green on the ribbon representation of the $MinE_{Ec}$ (PDB# 1EV0).*

4.7 NMR Analyses of $MinE_{Ng}$ Mutants

The presence of structure in the N-terminal domain of $MinE_{Ng}$ raises the possibility that the two functional domains of this protein may interact with each other, providing a potential mechanism for modulation of their respective functions. To explore this

possibility, ^{15}N-labeled samples were made of Ng-MinE that either contained a mutation in the N-terminal domain (A18D) or the C-terminal domain (E46A) and ^{1}H – ^{15}N HSQC recorded to look for inter-domain effects.

As shown in Figure 4.15, the HSQC spectrum of the A18D mutant (in red) shows only small differences from the spectrum recorded for wild-type $MinE_{Ng}$ (black) suggesting that no large-scale structural changes are introduced by the mutation. Circular dichroism spectroscopy of A18D $MinE_{Ng}$ (Figure 4.16) indicates that the secondary structure content has not been changed by this mutation providing additional evidence that the overall structure of the two proteins is similar. However, it appears that the local chemical environment and/or structure of some residues has been altered by the mutation since some peaks in the A18D HSQC spectrum, including those for N-terminal residues L6 - F8, D20, R21, E29 and A31, do not have the same chemical shift and/or relative intensities as the WT HSQC spectrum. In addition, TSD residues M72, D73, T80 and L81 also show differences between the two spectra. Localization of the corresponding residues in the TSD structure illustrates that they are clustered together at the dimer interface between the central two β-strands at two equivalent sites. The fact that there is a region of the TSD that is sensitive to mutations made to the anti-MinCD domain suggests that these C-terminal residues may experience a perturbation in local chemical environment, potentially due to a change in association between N- and C-terminal domains.

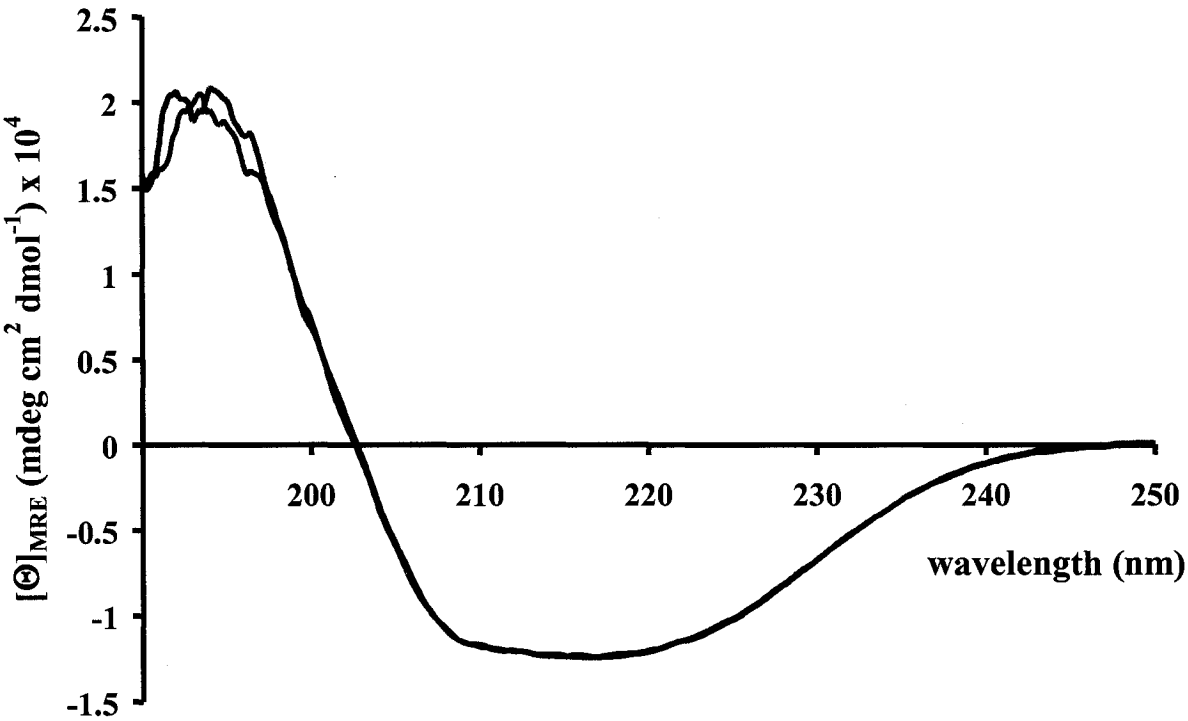

Figure 4.16: *CD Spectra of WT (red) vs. A18D (blue) $MinE_{Ng}$ in 10 mM Tris pH 9.5 at 25°C.*

The HSQC spectrum of the E46A mutant revealed more extensive, larger scale chemical shift perturbations relative to the wild-type spectrum, as would be expected from the close proximity of this TSD α-helix residue to the dimerization interface as shown in Figure 4.17. In agreement with previous studies with Ec-TSD suggesting that the analogous mutation does not perturb its global structure, we found that the CD spectrum for the mutant is superimposable with that of the wild-type protein (Figure 4.18). While the HSQC spectrum of the E46A mutant shows that many peaks are unaffected by the mutation, a number of peaks in the wild-type spectrum were not reproduced in the E46A spectrum. Specifically, residues along the length of the central helix that are involved in packing interactions either between subunits or with the β-sheet of the same subunit

appeared to show the largest perturbations. Smaller chemical shift changes were also observed for β-sheet residues that pack against this helix, potentially due to small structural changes induced by the mutation in the helix. Apart from these changes in the TSD resonances, residues in the N-terminal helix also showed changes due to the E46A mutation, with L7 and F8 showing the most notable difference since no trace of peak intensity at the wild-type position was observed for these peaks in the mutant spectrum. Again, the fact that mutations made in the C-terminal domain of $MinE_{Ng}$ are sensed in the N-terminal domain provides further evidence that the two domains could be structurally associated with each other.

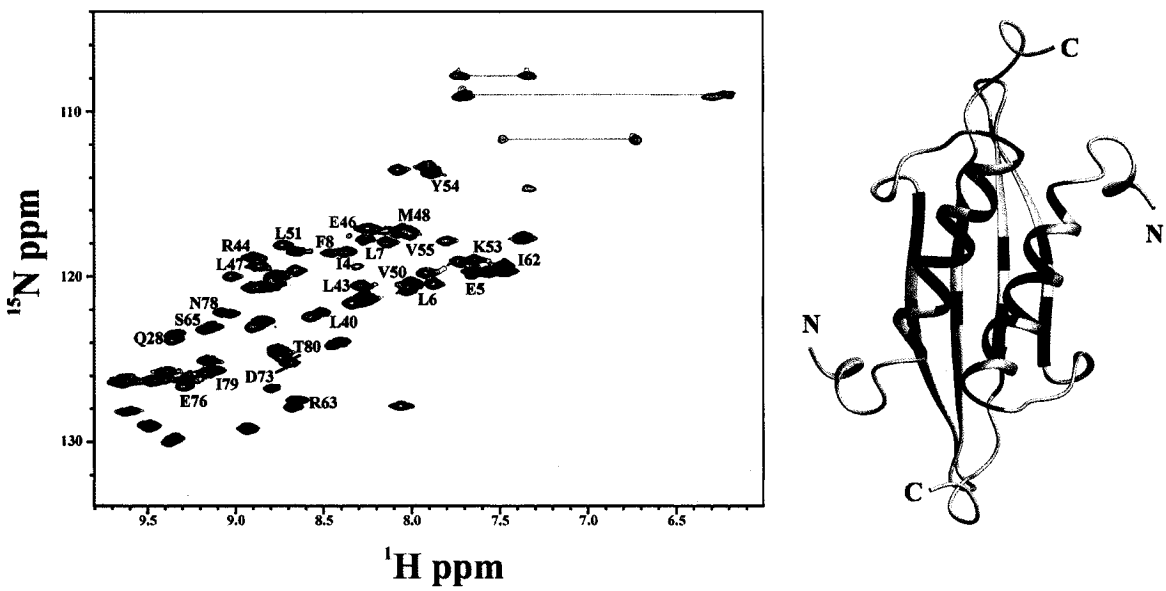

Figure 4.17: *$^{1}H - ^{15}N$ HSQC spectra of E46A (red) and WT (black) $MinE_{Ng}$. Chemical shifts that were perturbed are labeled in neon green on the spectra and mapped onto the $MinE_{Ec}$ structure. The site of the mutation (E46A) is highlighted in red on the structure on the right.*

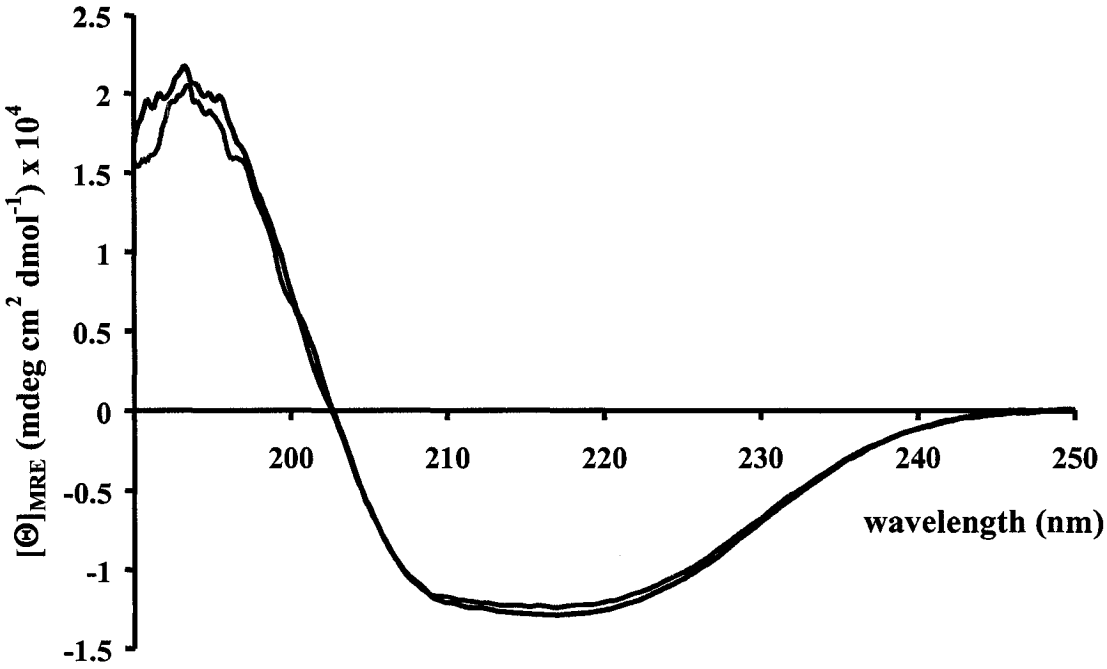

Figure 4.18: *CD Spectra of WT (red) and E46A (blue) $MinE_{Ng}$ in 10 mM Tris pH 9.5 at 25°C.*

In addition to these $MinE_{Ng}$ mutants, NMR and CD studies were done to investigate the structure of another N-domain mutant known to disrupt anti-MinCD function, namely L22D. In contrast to the previous mutants, the CD spectrum of L22D (Figure 4.19) showed a significant difference from the wild-type spectrum. This difference in structure was confirmed by NMR, which showed no amide peaks at high pH in spite of high solubility. Therefore, in contrast to the mutants studied above, L22D appears to lack a stable structure that could protect backbone amides from solvent exchange under these conditions. In addition, when the HSQC spectrum was run under neutral pH conditions (Figure 4.20), peaks of strong intensity and poor chemical shift dispersion characteristic of unfolded

protein, were observed along with broad peaks over a larger chemical shift range that may reflect regions of residual structure undergoing intermediate time-scale chemical exchange processes.

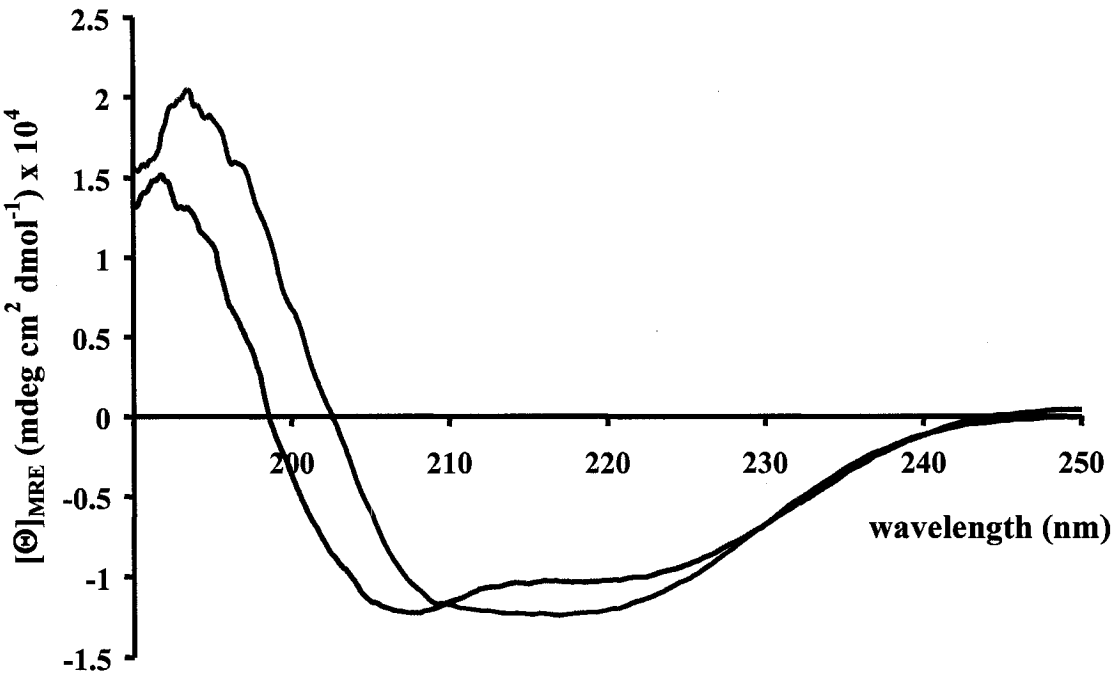

Figure 4.19: *CD Spectra of WT (red) and L22D (blue) $MinE_{Ng}$ in 10 mM Tris pH 7.4. at 25°C.*

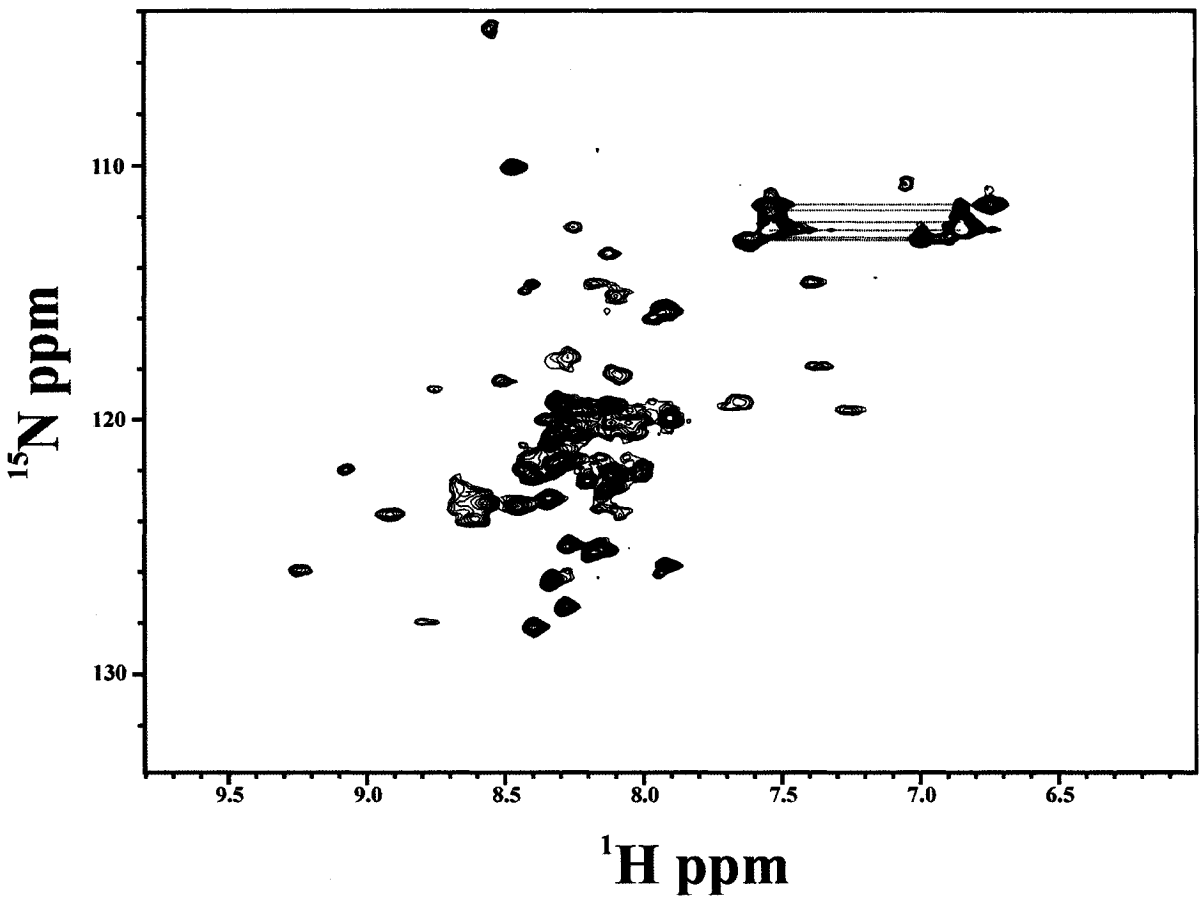

Figure 4.20: *$^{1}H - ^{15}N$ HSQC spectrum of 250 μM L22D in 50 mM Tris, 50 mM NaCl, 100 μM EDTA, 0.02% sodium azide and 0.2mM PMSF at pH 7.2, 25°C.*

To determine whether this change in NMR spectral property of L22D was due to a change in aggregation state, size exclusion chromatography was performed. As illustrated by the example shown in Figure 4.21, this mutant eluted as a single peak over a range of concentrations with an elution time similar to that of the wild-type $MinE_{Ng}$ dimer. However, it was not possible to determine whether L22D is also dimeric from this data since a monomeric unfolded protein would exhibit an altered mobility relative to that predicted by globular protein standards. Nonetheless, these results provide strong evidence

that the L22D mutation affects the structure and stability of the full-length protein even though the site of mutation in the primary sequence is far from the dimeric TSD.

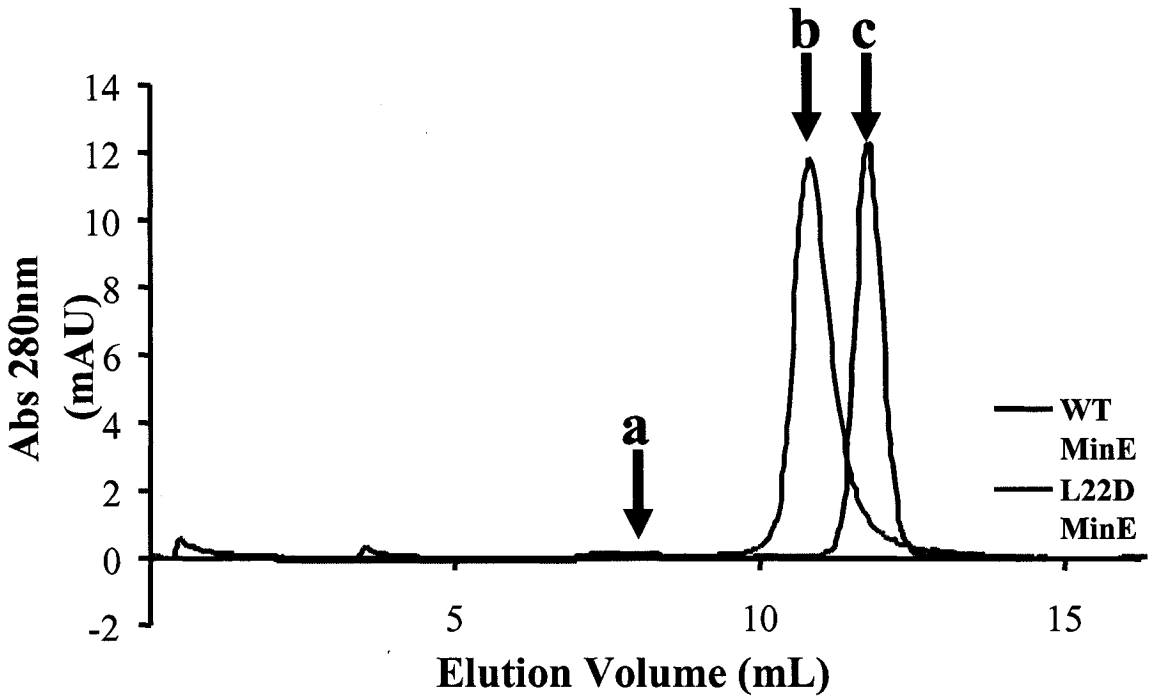

Figure 4.21: *Size-exclusion chromatogram of WT and L22D $MinE_{Ng}$ using Superdex75® 10/300 GL column in 50 mM Tris, 150 mM NaCl, 1 mM EDTA at pH 9.5 and at a flow rate of 0.5 mL/min.* ***(a)*** *represents the void volume at 8.0 mL;* ***(b)*** *L22D elution at ~10.8 mL;* ***(c)*** *WT elution at ~11.4 mL.*

4.8 Results Summary

Since one of the main objectives in this thesis is to obtain a suitable $MinE_{Ng}$ protein sample for NMR experiments and ultimately, to determine its full-length structure, solubility tests were performed in different buffer conditions. The best sample conditions

were then used to perform NMR experiments to assign backbone resonances for $MinE_{Ng}$. The following results were obtained from this study:

- optimal $MinE_{Ng}$ solubility was obtained at high pH conditions
- 48 out of the expected 89 backbone amide peaks were observed in the $^{1}H - ^{15}N$ HSQC at high pH, 46 of which could be assigned
- the secondary structure of the TSD of $MinE_{Ng}$ is in agreement with that of the structure Ec-TSD
- the anti-MinCD domain has a stable structure in the absence of MinD, which includes a β-strand region
- mutations made in one domain led to chemical shift changes in the other domain, suggesting an interaction between the two domains
- the L22D mutation destabilizes $MinE_{Ng}$ structure

CHAPTER 5

DISCUSSION

In order for bacterial cell division to exclusively occur at mid-cell MinE must counteract the inhibitory action of the MinCD complex site-specifically. For this purpose, it performs two functional roles: MinD binding to dissociate the MinCD complex and MinE ring formation to ensure topological specificity. It has been shown that these two functions can be decoupled by expressing fragments of MinE, with N-terminal fragments being associated with anti-MinCD activity and C-terminal fragments disrupting topological specificity (*12, 42*). Although the study of these functional domains in isolation has led to the identification of a number of functionally critical residues (*44, 45*), this approach can limit the examination of potential interactions between domains. Since these interactions may give rise to additional contributions that modulate MinE activity, our investigation focused on the structural properties of full length $MinE_{Ng}$.

5.1 $MinE_{Ng}$ is Stably Folded at Elevated pH Conditions

Although solubility considerations made it necessary to perform many of our studies on full length $MinE_{Ng}$ in high pH solutions, both CD and NMR spectroscopy confirmed that the structure is not significantly altered by the use of elevated pH conditions. Moreover, the ability to observe some signals in the $^{1}H - ^{15}N$ HSQC spectrum

made it possible to identify structured regions since these peaks must arise from amide protons that are protected from rapid base-catalyzed solvent exchange. Assignment of these peaks showed solvent protection of $MinE_{Ng}$ in regions that are homologous to α– and β-secondary structure elements forming the core of the Ec-TSD (*45*). In addition, N-terminal anti-MinCD domain residues were also evident in the spectrum suggesting that parts of this domain are folded in the intact protein. This was a surprising result given that a previous trypsin digest performed on full length $MinE_{Ec}$ showed that only the C-terminal domain is resistant to digestion, implying that the N-terminal domain might not be folded (*43*). However, we observe that almost all of the potential sites for trypsin cleavage in the N-terminal domain lie outside the protected regions that are visible in the high pH spectra as shown in Figure 5.1. Therefore, the NMR solvent accessibility results on $MinE_{Ng}$ correlate well with previous trypsin digestion studies on $MinE_{Ec}$ since these solvent-accessible regions are more likely to be cleaved. Cleavage at one or more of these sites would almost certainly disrupt the ability of the N-terminal region to fold, thereby facilitating complete digestion of this domain. Therefore, it is likely that the structure detected in the N-terminal domain of $MinE_{Ng}$ is a conserved feature that is also present in the Ec protein.

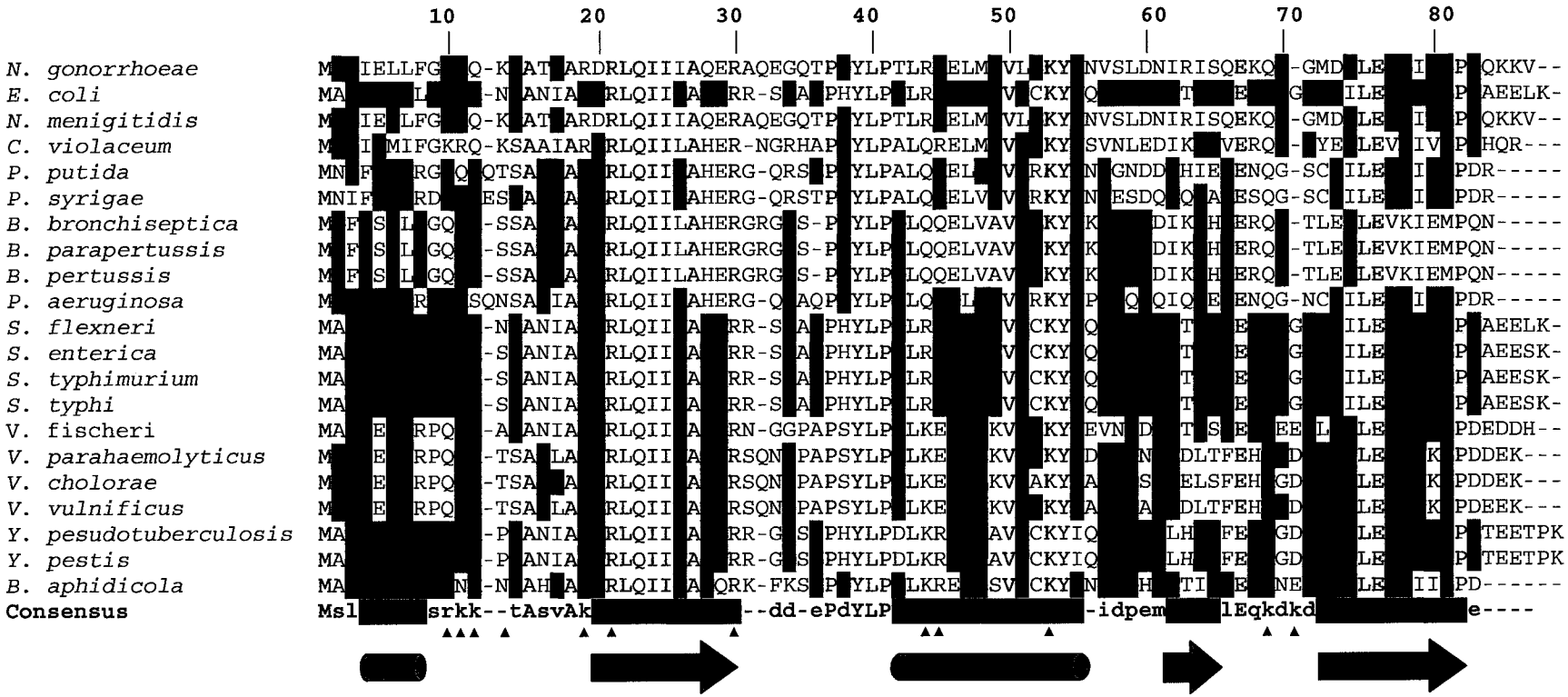

Figure 5.1: *Protein Sequence Alignment for MinE – The sequence alignement and the consensus was generated using Basic Local Alignment Search Tool (NCBI-BLAST2) from NCBI. Conserved regions are highlighted in yellow and the consensus residues conserved in nine or more of the 18 protein sequences are coloured in red. The capital letters in the consensus sequence represent the most conserved residues for all species with regions that were solvent protected from amide exchange at high pH highlighted in pink and the secondary structures are indicated under the consensus. Potential sites for trypsin cleavage of the E. coli MinE sequence are indicated under the consensus with triangles.*

5.2 *$MinE_{Ng}$ is Structurally Similar to $MinE_{Ec}$*

The results from the current study also reveal a great degree of structural similarity between the TSD of $MinE_{Ng}$ and $MinE_{Ec}$, as would be predicted from the high level of sequence homology. Specifically, the calculated backbone secondary chemical shifts for these residues show that the secondary structure is the same as that in the Ec-TSD structure. In addition, residues predicted to localize to the extensive dimeric interface formed by the αβ-motif in the Ec-TSD structure were found to be completely protected from solvent exchange in $MinE_{Ng}$. Together with the gel filtration data, this indicates that, like $MinE_{Ec}$, the Ng protein self-associates with high affinity through a highly related structural motif.

Our results supporting a high degree of structural homology between $MinE_{Ec}$ and $MinE_{Ng}$ provides some insight into previous studies that had raised questions about potential differences between MinE proteins from the two different species (*48, 49*). In particular, mutations made to the TSD in $MinE_{Ng}$ displayed reduced anti-MinCD activity as determined by yeast two-hybrid and MinD ATPase stimulation assays, suggesting a potential role for the TSD in MinD binding (*22, 44*). In contrast, studies on analogous mutants in $MinE_{Ec}$ showed wild type-like behavior in complementation studies in *E. coli minE* knockouts. This apparent difference in the role of the TSD in anti-MinCD activity raised the question as to whether functionally relevant structural differences might exist between $MinE_{Ng}$ and $MinE_{Ec}$. However, the high degree of similarity that we observe between Ng- and Ec-TSD structure and dimerization properties suggest that the proteins from the two species should be functionally similar, a finding that agrees well with functional complementation studies. For example, it has been shown that $MinE_{Ng}$ proteins oscillate when expressed in *E. coli* with $MinD_{Ng}$, and that oscillation of $MinD_{Ng}$ in *E. coli*

can be induced by co-expression with either $MinE_{Ec}$ or $MinE_{Ng}$ (*48*). Given the structural and functional similarities between Ng and Ec MinE proteins, we suggest that the previous observation of reduced MinD binding exhibited by $MinE_{Ng}$ mutants of the TSD reflects a conserved role for the TSD in MinD interactions. Yeast three-hybrid experiments with Ec Min proteins support this hypothesis since the Ec TSD alone was shown to weakly disrupt the MinCD complex (*44*). Overall these results indicate that MinE from both round and rod-shaped bacteria function via similar structures and mechanisms, with both domains playing a role in anti-MinCD function.

Although less is known about the structure of the N-terminal region of $MinE_{Ec}$, some evidence for structural similarities between $MinE_{Ec}$ and $MinE_{Ng}$ was also obtained in our study. According to the secondary chemical shift calculations for the short solvent-protected segment at the N-terminus of $MinE_{Ng}$, this region is α-helical. This compares well with previous solution NMR studies on a peptide corresponding to $MinE_{Ec}$ residues 1 – 22 since helix-specific NOEs were observed in the same region (*43*). However, the $MinE_{Ec1-22}$ (*43*) peptide structure was described as a nascent helix, while in the full-length $MinE_{Ng}$ this helix appears to be more stable since it is protected from solvent exchange and shows significant secondary shifts. While these residues are not identical between Ec and Ng proteins, there is a conserved pattern of hydrophobic and hydrophilic residues (h-h-p-h-h, where h is hydrophobic and p is polar, corresponding to $MinE_{Ng}$ residues 3 – 7). Nonetheless, the increase in helix stability may reflect differences in the intrinsic helical propensity of the Ec and Ng sequences as would be suggested by secondary structure prediction algorithms such as AGADIR (*87*). In addition, since the more stable helix is

observed in the full-length MinE protein, it is also possible that stabilizing interactions occur with other parts of the protein such as the C-terminal TSD.

5.3 Evidence for Interactions Between the Topological Specificity and Anti-MinCD Domains

Evidence that interactions may occur between the TSD and anti-MinCD domain has been provided by our investigations on mutants of $MinE_{Ng}$. Specifically, the NMR spectrum of the E46A mutant showed differences from the wild-type spectrum for peaks assigned to the N-terminal helix even though the mutation was in the TSD. Similarly, the A18D spectrum shows evidence for shifts in both the N- and C-terminal domains, including residues from this helix (L7, F8), again indicating an interaction between domains. The fact that peaks arising from the N-terminal helix are sensitive to mutations in either domain may reflect a direct role for this helix in inter-domain interactions. This provides insight into the potential role of this helix since deletion of 5 residues from the N-terminal side of $MinE_{Ec}$ *in vivo* leads to cell length heterogeneity and some minicell formation (*42*) suggesting that the truncated MinE is still active, but has lost topological specificity. Given that this helix does not appear to participate in direct interactions with MinD according to protein interaction studies in yeast on $MinE_{Ng}$ (*49*) and $MinE_{Ec,1-31}$ (*44*), deletion of the first five residues may disrupt an interaction between the N-terminal helix and the TSD that could alter the accessibility of residues important for MinD binding and/or topological specificity.

Additional evidence for an intimate association between anti-MinCD and TS domains was provided by our studies on the $MinE_{Ng}$ mutant L22D. Like $MinD_{Ng}$ mutant

A18D, the L22D mutant is not able to bind to $MinD_{Ng}$ or induce $MinD_{Ng}$ oscillation in *E. coli*. However, in contrast to A18D, the spectrum of this mutant is markedly different from that of the wild-type protein. In the L22D spectrum, approximately 25 intense peaks can be distinguished in the central region suggesting that it is at least partly unfolded. In addition, there is also a subset of broader peaks occurring over a wider range of proton chemical shifts that do not bear any resemblance to those in the wild-type spectrum. The appearance of these peaks suggests that although there is residual structure, it is not stable and may be undergoing conformational exchange. The CD spectra provide further insight into the structure of this mutant, with the secondary structure deconvolution program CDPro (*56, 60, 61*) indicating ~5% decrease in α-helix and concomitant increase in turn and unordered conformations relative to wild-type $MinE_{Ng}$. Collectively, these data show that the L22D mutation destabilizes the $MinE_{Ng}$ structure and leads to partial unfolding. The destabilizing effect on both N- and C-terminal domains from this single point mutation again provides evidence for structural association of the two functional domains.

Our discovery that the N-terminal region of MinE interacts with the TSD helps to explain why MinE does not independently localize to the membrane even though the anti-MinCD domain by itself has a strong tendency to bind the *E. coli* inner membrane. For example, GFP-tagged N-terminal $MinE_{Ec}$ peptide ($MinE_{1-31}$) has been shown to localize to the membrane even when MinD is not present. However, in the full length protein the N-terminal domain would be folded together with the TSD, making it inaccessible to membrane binding. Disruption of this interaction would also explain why mutants L22S, L22R or I25R in full length $MinE_{Ec}$ (*44*) exhibit MinD-independent membrane-localization (*15*). As we observed for the L22D mutant of $MinE_{Ng}$, the structure and stability of these

mutants may be dramatically different from wild type, with the N-terminal domain likely being available for promiscuous membrane interactions.

The pivotal structural role of Leu22 in $MinE_{Ng}$ is particularly interesting considering that this residue occurs in a β-sheet region of the anti-MinCD domain that includes a number of other residues also important for MinD interactions. Our results represent the first structural characterization for this region of MinE, although it was originally predicted that the nascent α-helix observed at the N-terminus might extend to the C-terminal end of this domain. However, neither the secondary chemical shifts nor the NOESY data provide evidence for helical structure in this region of the protein. This finding is especially surprising in light of previous experiments testing MinD binding by a 31-residue N-terminal fragment of $MinE_{Ec}$ (Ec-$MinE_{1-31}$) that showed how residues critical to this interaction would localize to one side of a hypothetical α-helix (*44*). Corresponding mutations made to the full length $MinE_{Ec}$ confirmed the functional importance of some of these residues, since they were not able to relieve MinCD inhibition of cell division. The fact that most of these critical anti-MinCD residues (*e.g.* L22, I25, I26, R30) are located in this α-region yet do not occur with a periodicity that would suggest binding in a β-sheet conformation is consistent with two possible scenarios:

1) only a subset of these residues directly participate in the MinD interaction, with the others being critical to the structural integrity of MinE, and/or

2) a structural transition is required such that the β-conformation becomes helical when bound to MinD.

In the latter case, the MinD interaction would have to be stronger than the inter-domain interaction in order to induce the structural transition. However, residues in the anti-MinCD domain have also been shown to play a role in dimerization and hence the potential effect of these mutations on the structure of MinE can also not be ignored.

Our results on full length MinE suggest that previous models based on the idea of two structurally independent MinE functional domains must be refined to account for the interaction between domains. Although the precise nature of this interaction has yet to be elucidated, it is possible that this structural feature of MinE will help to resolve the question of how topological specificity is conferred. While it has been shown that inhibition of the MinCD interaction can be obtained by expression of even just the first 22 residues of MinE, it is not well understood how the rest of the protein acts to restrict the anti-MinCD activity to the midpoint of the cell. From previous studies, it appears that normal cell division requires that MinD localize to a MinE-dependent subcellular coiled structure (*15*) and that high concentrations of MinE localize to the leading edge of the coiled array to form the E-ring. Mutations in Ec-MinE such as D45A/V49A that have lost topological specificity also do not show evidence of E-ring formation leading to longer MinD polar zones with irregular growth and decay properties (*10*). Based on these results it was suggested that E-ring formation involves interactions between the TSD and, either other parts of MinE, or with other proteins yet to be identified. Our findings that the TSD interacts with the N-domain of MinE raises the possibility that these interactions may even occur between MinE dimers. Similar to 'domain-swapping' where intra-molecular interactions are exchanged for inter-molecular interactions, a low affinity MinE oligomerization could be facilitated by interactions where intra-dimer interactions between the anti-MinCD and TS domains are replaced by inter-dimer interactions. In fact, sedimentation equilibrium experiments on

purified $MinE_{Ec}$ indicate that low affinity tetramer and octamer (*45*) formation does occur but not observed for the TSD alone (*43*). Given that the local concentration of MinE that is incorporated into the coiled array could be very high, formation of these higher order oligomers may be favored in this case. The role of the TSD in the formation of these higher order structures could explain the requirement for this domain in normal bacterial cell division. However, it is clear that understanding how MinE performs its anti-MinCD function site-specifically will require high resolution structural information on the full-length protein, a prospect which is currently being pursued. This will not only clarify how the anti-MinCD domain can bind to MinD, but should also provide insight into how the TSD contributes to the interaction and how topological specificity is conferred.

Claims to Original Research

1. Determined the optimal solubility of the wild-tupe full-length $MinE_{Ng}$ at high pH conditions and the solubility of the E46A mutant at physiological conditions
2. Based on our recent publication, we have discovered the following:
    a. The secondary structure of the TSD of $MinE_{Ng}$ is in agreement with that of the structure Ec-TSD
    b. The secondary structure of the anti-MinCD domain has been determined for the very first time, based on our NMR chemical shift data
    c. There are possible intra-molecular interactions between the anti-MinCD and TS domains based on mutational studies in both domains
    d. There might be MinE–MinE interactions in the MinE ring that might occur through inter-dimer domain swapping based on previous MinE oligomerization and MinE–MinD interaction.

Publications

Ramos, D., Ducat, T., Cheng, J., Eng, N.F., Dillon, J.A. and Goto, N.K. *Conformation of the Cell Division Regulator MinE: Evidence for Interactions between the Topological Specificity and Anti-MinCD Domains.* Biochemistry, 2006. **45**(14): p. 4593-601.

References

(1) Prescott, L. M., Harley, J. P., and Klein, D. A. (1996) *Microbiology*, Third Edition ed., Wm. C. Brown Publishers.

(2) Nanninga, N. (1998) Morphogenesis of *Escherichia coli*. *Microbiol Mol Biol Rev 62*, 110-129.

(3) Westling-Haggstrom, B., Elmros, T., Normark, S., and Winblad, B. (1977) Growth pattern and cell division in *Neisseria gonorrhoeae*. *J Bacteriol 129*, 333-342.

(4) Fitz-James, P. (1964) Thin Sections of Dividing *Neisseria gonorrhoeae*. *J Bacteriol 87*, 1477-1482.

(5) Chen, J. C., and Beckwith, J. (2001) FtsQ, FtsL and FtsI require FtsK, but not FtsN, for co-localization with FtsZ during *Escherichia coli* cell division. *Mol Microbiol 42*, 395-413.

(6) Begg, K., Nikolaichik, Y., Crossland, N., and Donachie, W. D. (1998) Roles of FtsA and FtsZ in activation of division sites. *J Bacteriol 180*, 881-884.

(7) Corbin, B. D., Geissler, B., Sadasivam, M., and Margolin, W. (2004) Z-ring-independent interaction between a subdomain of FtsA and late septation proteins as revealed by a polar recruitment assay. *J Bacteriol 186*, 7736-7744.

(8) Yu, X. C., and Margolin, W. (1999) FtsZ ring clusters in min and partition mutants: role of both the Min system and the nucleoid in regulating FtsZ ring localization. *Mol Microbiol 32*, 315-326.

(9) Justice, S. S., Garcia-Lara, J., and Rothfield, L. I. (2000) Cell division inhibitors SulA and MinC/MinD block septum formation at different steps in the assembly of the *Escherichia coli* division machinery. *Mol Microbiol 37*, 410-423.

(10) Shih, Y. L., Fu, X., King, G. F., Le, T., and Rothfield, L. (2002) Division site placement in *E.coli*: mutations that prevent formation of the MinE ring lead to loss of the normal midcell arrest of growth of polar MinD membrane domains. *EMBO J 21*, 3347-3357.

(11) Hale, C. A., Meinhardt, H., and de Boer, P. A. (2001) Dynamic localization cycle of the cell division regulator MinE in *Escherichia coli*. *EMBO J 20*, 1563-1572.

(12) Zhao, C. R., de Boer, P. A., and Rothfield, L. I. (1995) Proper placement of the *Escherichia coli* division site requires two functions that are associated with different domains of the MinE protein. *Proc Natl Acad Sci U S A 92*, 4313-4317.

(13) Janakiraman, A., and Goldberg, M. B. (2004) Evidence for polar positional information independent of cell division and nucleoid occlusion. *Proc Natl Acad Sci U S A 101*, 835-840.

(14) Rothfield, L., Justice, S., and Garcia-Lara, J. (1999) Bacterial cell division. *Annu Rev Genet 33*, 423-448.

(15) Shih, Y. L., Le, T., and Rothfield, L. (2003) Division site selection in *Escherichia coli* involves dynamic redistribution of Min proteins within coiled structures that extend between the two cell poles. *Proc Natl Acad Sci U S A 100*, 7865-7870.

(16) Ramirez-Arcos, S., Szeto, J., Beveridge, T., Victor, C., Francis, F., and Dillon, J. (2001) Deletion of the cell-division inhibitor MinC results in lysis of *Neisseria gonorrhoeae*. *Microbiology 147*, 225-237.

(17) de Boer, P. A., Crossley, R. E., and Rothfield, L. I. (1989) A division inhibitor and a topological specificity factor coded for by the minicell locus determine proper placement of the division septum in *E. coli*. *Cell 56*, 641-649.

(18) de Boer, P. A., Crossley, R. E., and Rothfield, L. I. (1988) Isolation and properties of minB, a complex genetic locus involved in correct placement of the division site in *Escherichia coli*. *J Bacteriol 170*, 2106-2112.

(19) Hu, Z., Mukherjee, A., Pichoff, S., and Lutkenhaus, J. (1999) The MinC component of the division site selection system in *Escherichia coli* interacts with FtsZ to prevent polymerization. *Proc Natl Acad Sci U S A 96*, 14819-14824.

(20) de Boer, P. A., Crossley, R. E., and Rothfield, L. I. (1992) Roles of MinC and MinD in the site-specific septation block mediated by the MinCDE system of *Escherichia coli*. *J Bacteriol 174*, 63-70.

(21) Errington, J., Daniel, R. A., and Scheffers, D. J. (2003) Cytokinesis in bacteria. *Microbiol Mol Biol Rev 67*, 52-65.

(22) Ma, L., King, G. F., and Rothfield, L. (2004) Positioning of the MinE binding site on the MinD surface suggests a plausible mechanism for activation of the *Escherichia coli* MinD ATPase during division site selection. *Mol Microbiol 54*, 99-108.

(23) de Boer, P. A., Crossley, R. E., Hand, A. R., and Rothfield, L. I. (1991) The MinD protein is a membrane ATPase required for the correct placement of the *Escherichia coli* division site. *EMBO J 10*, 4371-4380.

(24) Lackner, L. L., Raskin, D. M., and de Boer, P. A. (2003) ATP-dependent interactions between *Escherichia coli* Min proteins and the phospholipid membrane in vitro. *J Bacteriol 185*, 735-749.

(25) Raskin, D. M., and de Boer, P. A. (1999) Rapid pole-to-pole oscillation of a protein required for directing division to the middle of *Escherichia coli*. *Proc Natl Acad Sci U S A 96*, 4971-4976.

(26) Ramirez-Arcos, S., Salimnia, H., Bergevin, I., Paradis, M., and Dillon, J. A. (2001) Expression of *Neisseria gonorrhoeae* cell division genes ftsZ, ftsE and minD is influenced by environmental conditions. *Res Microbiol 152*, 781-791.

(27) Hu, Z., Saez, C., and Lutkenhaus, J. (2003) Recruitment of MinC, an inhibitor of Z-ring formation, to the membrane in *Escherichia coli*: role of MinD and MinE. *J Bacteriol 185*, 196-203.

(28) Hu, Z., and Lutkenhaus, J. (2001) Topological regulation of cell division in *E. coli* spatiotemporal oscillation of MinD requires stimulation of its ATPase by MinE and phospholipid. *Mol Cell 7*, 1337-1343.

(29) Zhou, H., Schulze, R., Cox, S., Saez, C., Hu, Z., and Lutkenhaus, J. (2005) Analysis of MinD mutations reveals residues required for MinE stimulation of the MinD ATPase and residues required for MinC interaction. *J Bacteriol 187*, 629-638.

(30) Szeto, J., Eng, N. F., Acharya, S., Rigden, M. D., and Dillon, J. A. (2005) A conserved polar region in the cell division site determinant MinD is required for responding to MinE-induced oscillation but not for localization within coiled arrays. *Res Microbiol 156*, 17-29.

(31) Lutkenhaus, J., and Sundaramoorthy, M. (2003) MinD and role of the deviant Walker A motif, dimerization and membrane binding in oscillation. *Mol Microbiol 48*, 295-303.

(32) Suefuji, K., Valluzzi, R., and RayChaudhuri, D. (2002) Dynamic assembly of MinD into filament bundles modulated by ATP, phospholipids, and MinE. *Proc Natl Acad Sci U S A 99*, 16776-16781.

(33) Hu, Z., Gogol, E. P., and Lutkenhaus, J. (2002) Dynamic assembly of MinD on phospholipid vesicles regulated by ATP and MinE. *Proc Natl Acad Sci U S A 99*, 6761-6766.

(34) Margolin, W. (2001) Bacterial cell division: a moving MinE sweeper boggles the MinD. *Curr Biol 11*, R395-398.

(35) Hu, Z., and Lutkenhaus, J. (1999) Topological regulation of cell division in *Escherichia coli* involves rapid pole to pole oscillation of the division inhibitor MinC under the control of MinD and MinE. *Mol Microbiol 34*, 82-90.

(36) Fu, X., Shih, Y. L., Zhang, Y., and Rothfield, L. I. (2001) The MinE ring required for proper placement of the division site is a mobile structure that changes its cellular location during the *Escherichia coli* division cycle. *Proc Natl Acad Sci U S A 98*, 980-985.

(37) Raskin, D. M., and de Boer, P. A. (1997) The MinE ring: an FtsZ-independent cell structure required for selection of the correct division site in *E. coli*. *Cell 91*, 685-694.

(38) Yu, X. C., Sun, Q., and Margolin, W. (2001) FtsZ rings in mukB mutants with or without the Min system. *Biochimie 83*, 125-129.

(39) Gitai, Z., and Shapiro, L. (2003) Bacterial cell division spirals into control. *Proc Natl Acad Sci U S A 100*, 7423-7424.

(40) RayChaudhuri, D., Gordon, G. S., and Wright, A. (2000) How does a bacterium find its middle? *Nat Struct Biol 7*, 997-999.

(41) Adler, H. I., Fisher, W. D., Cohen, A., and Hardigree, A. A. (1967) Miniature *Escherichia coli* cells deficient in DNA. *Proc Natl Acad Sci U S A 57*, 321-326.

(42) Pichoff, S., Vollrath, B., Touriol, C., and Bouche, J. P. (1995) Deletion analysis of gene minE which encodes the topological specificity factor of cell division in *Escherichia coli. Mol Microbiol 18*, 321-329.

(43) King, G. F., Rowland, S. L., Pan, B., Mackay, J. P., Mullen, G. P., and Rothfield, L. I. (1999) The dimerization and topological specificity functions of MinE reside in a structurally autonomous C-terminal domain. *Mol Microbiol 31*, 1161-1169.

(44) Ma, L. Y., King, G., and Rothfield, L. (2003) Mapping the MinE site involved in interaction with the MinD division site selection protein of *Escherichia coli. J Bacteriol 185*, 4948-4955.

(45) King, G. F., Shih, Y. L., Maciejewski, M. W., Bains, N. P., Pan, B., Rowland, S. L., Mullen, G. P., and Rothfield, L. I. (2000) Structural basis for the topological specificity function of MinE. *Nat Struct Biol 7*, 1013-1017.

(46) Zhang, Y., Rowland, S., King, G., Braswell, E., and Rothfield, L. (1998) The relationship between hetero-oligomer formation and function of the topological specificity domain of the *Escherichia coli* MinE protein. *Mol Microbiol 30*, 265-273.

(47) Corbin, B. D., Yu, X. C., and Margolin, W. (2002) Exploring intracellular space: function of the Min system in round-shaped *Escherichia coli. EMBO J 21*, 1998-2008.

(48) Ramirez-Arcos, S., Szeto, J., Dillon, J. A., and Margolin, W. (2002) Conservation of dynamic localization among MinD and MinE orthologues: oscillation of *Neisseria gonorrhoeae* proteins in *Escherichia coli. Mol Microbiol 46*, 493-504.

(49) Eng, N. F., Szeto, J., Acharya, S., Tessier, D., and Dillon, J. A. (2006) The C-terminus of MinE from *Neisseria gonorrhoeae* acts as a topological specificity factor by modulating MinD activity in bacterial cell division. *Res Microbiol 157*, 333-344.

(50) Greenfield, N. J. (1996) Methods to estimate the conformation of proteins and polypeptides from circular dichroism data. *Anal Biochem 235*, 1-10.

(51) Kelly, S. M., and Price, N. C. (2000) The use of circular dichroism in the investigation of protein structure and function. *Curr Protein Pept Sci 1*, 349-384.

(52) Greenfield, N. J. (2004) Analysis of circular dichroism data. *Methods Enzymol 383*, 282-317.

(53) Greenfield, N., and Fasman, G. D. (1969) Computed circular dichroism spectra for the evaluation of protein conformation. *Biochemistry 8*, 4108-4116.

(54) Nelson, D. L., and Cox, M. M. (2000) *Lehninger Principles of Biochemistry*, Third Edition ed., Worth Publishers, New York, N.Y.

(55) Koradi, R., Billeter, M., and Wuthrich, K. (1996) MOLMOL: a program for display and analysis of macromolecular structures. *J Mol Graph 14*, 51-55, 29-32.

(56) Sreerama, N., and Woody, R. W. (2004) Computation and analysis of protein circular dichroism spectra. *Methods Enzymol 383*, 318-351.

(57) Creighton, T. E. (1993) *Proteins: Structures and Molecular Properties*, Freeman, New, York, N.Y.

(58) Sreerama, N., and Woody, R. W. (1994) Poly(pro)II helices in globular proteins: identification and circular dichroic analysis. *Biochemistry 33*, 10022-10025.

(59) Sreerama, N., and Woody, R. W. (1994) Protein secondary structure from circular dichroism spectroscopy. Combining variable selection principle and cluster analysis with neural network, ridge regression and self-consistent methods. *J Mol Biol 242*, 497-507.

(60) Sreerama, N., and Woody, R. W. (1993) A self-consistent method for the analysis of protein secondary structure from circular dichroism. *Anal Biochem 209*, 32-44.

(61) Sreerama, N., and Woody, R. W. (2000) Estimation of protein secondary structure from circular dichroism spectra: comparison of CONTIN, SELCON, and CDSSTR methods with an expanded reference set. *Anal Biochem 287*, 252-260.

(62) Cavanagh, J., Fairbrother, W. J., Palmer III, A. G., and Skelton, N. J. (1996) *Protein NMR Spectroscopy: Principles and Practice*, Academic Press, San Diego.

(63) Kanelis, V., Forman-Kay, J. D., and Kay, L. E. (2001) Multidimensional NMR methods for protein structure determination. *IUBMB Life 52*, 291-302.

(64) Sattler, M., Schleucher, J., and Griesinger, C. (1999) Heteronuclear multidimensional NMR experiments for the structure determination of proteins in solution employing pulsed field gradients. *Prog Nucl Magn Res Spectrosc 34*, 93 - 158.

(65) Gronenborn, A. M., and Clore, G. M. (1996) Rapid screening for structural integrity of expressed proteins by heteronuclear NMR spectroscopy. *Protein Sci 5*, 174-177.

(66) Zheng, Z., Gryk, M. R., Finucane, M. D., and Jardetzky, O. (1995) Investigation of protein amide-proton exchange by 1H longitudinal spin relaxation. *J Magn Reson B 108*, 220-234.

(67) Seavey, B. R., Farr, E. A., Westler, W. M., and Markley, J. L. (1991) A relational database for sequence-specific protein NMR data. *J Biomol NMR 1*, 217-236.

(68) Wishart, D. S., and Sykes, B. D. (1994) The 13C chemical-shift index: a simple method for the identification of protein secondary structure using 13C chemical-shift data. *J Biomol NMR 4*, 171-180.

(69) Wishart, D. S., Sykes, B. D., and Richards, F. M. (1992) The chemical shift index: a fast and simple method for the assignment of protein secondary structure through NMR spectroscopy. *Biochemistry 31*, 1647-1651.

(70) Wishart, D. S., Sykes, B. D., and Richards, F. M. (1991) Simple techniques for the quantification of protein secondary structure by 1H NMR spectroscopy. *FEBS Lett 293*, 72-80.

(71) Wishart, D. S., and Sykes, B. D. (1994) Chemical shifts as a tool for structure determination. *Methods Enzymol 239*, 363-392.

(72) Ramos, D., Ducat, T., Cheng, J., Eng, N. F., Dillon, J. A., and Goto, N. K. (2006) Conformation of the Cell Division Regulator MinE: Evidence for Interactions

between the Topological Specificity and Anti-MinCD Domains. *Biochemistry 45*, 4593-4601.

(73) Ford, K. G., Whitmarsh, A. J., and Hornby, D. P. (1994) Overexpression and purification of eukaryotic transcription factors as glutathione-S-transferase fusions in *E. coli. Methods Mol Biol 30*, 185-197.

(74) Inoue, H., Nojima, H., and Okayama, H. (1990) High efficiency transformation of *Escherichia coli* with plasmids. *Gene 96*, 23-28.

(75) Hengen, P. N. (1996) Methods and reagents. preparing ultra-competent *Escherichia coli. Trends Biochem Sci 21*, 75-76.

(76) Sambrook, J., Fritsch, E. F., and Maniatis, T. (1989) *Molecular Cloning: A Laboratory Manual*, Second Edition ed., Cold Spring Harbor Laboratory, Cold Spring Harbor, N.Y.

(77) Studier, F. W., Rosenberg, A. H., Dunn, J. J., and Dubendorff, J. W. (1990) Use of T7 RNA polymerase to direct expression of cloned genes. *Methods Enzymol 185*, 60-89.

(78) Delaglio, F., Grzesiek, S., Vuister, G. W., Zhu, G., Pfeifer, J., and Bax, A. (1995) NMRPipe: a multidimensional spectral processing system based on UNIX pipes. *J Biomol NMR 6*, 277-293.

(79) Johnson, B. A., and Blevins, R. A. (1994) NMRView: A computer program for the visualization and analysis of NMR data. *J Biomol NMR 4*, 603 - 614.

(80) Johnson, B. A. (2004) Using NMRView to visualize and analyze the NMR spectra of macromolecules. *Methods Mol Biol 278*, 313-352.

(81) Bradford, M. M. (1976) A rapid and sensitive method for the quantitation of microgram quantities of protein utilizing the principle of protein-dye binding. *Anal Biochem 72*, 248-254.

(82) Zor, T., and Selinger, Z. (1996) Linearization of the Bradford protein assay increases its sensitivity: theoretical and experimental studies. *Anal Biochem 236*, 302-308.

(83) Wiechelman, K. J., Braun, R. D., and Fitzpatrick, J. D. (1988) Investigation of the bicinchoninic acid protein assay: identification of the groups responsible for color formation. *Anal Biochem 175*, 231-237.

(84) Smith, P. K., Krohn, R. I., Hermanson, G. T., Mallia, A. K., Gartner, F. H., Provenzano, M. D., Fujimoto, E. K., Goeke, N. M., Olson, B. J., and Klenk, D. C. (1985) Measurement of protein using bicinchoninic acid. *Anal Biochem 150*, 76-85.

(85) Bondos, S. E., and Bicknell, A. (2003) Detection and prevention of protein aggregation before, during, and after purification. *Anal Biochem 316*, 223-231.

(86) Golovanov, A. P., Hautbergue, G. M., Wilson, S. A., and Lian, L. Y. (2004) A simple method for improving protein solubility and long-term stability. *J Am Chem Soc 126*, 8933-8939.

(87) Munoz, V., and Serrano, L. (1997) Development of the multiple sequence approximation within the AGADIR model of alpha-helix formation: comparison with Zimm-Bragg and Lifson-Roig formalisms. *Biopolymers 41*, 495-509.